2013-04-29

Bounds on RF cooperative localization for video capsule endoscopy

Yunxing Ye
Worcester Polytechnic Institute

BOUNDS ON RF COOPERATIVE LOCALIZATION FOR VIDEO CAPSULE ENDOSCOPY

by

Yunxing Ye

A Dissertation

Submitted to the Faculty

of the

WORCESTER POLYTECHNIC INSTITUTE

in partial fulfillment of the requirements for the

Degree of Doctor of Philosophy

in

Electrical and Computer Engineering

by

May 2013

APPROVED:

Prof. Kaveh Pahlavan, Major Advisor	Prof. Yehia Massoud, Department Head
Prof. Allen Levesque, WPI	Prof. Xinming Huang, WPI
Prof. Sergey Makarov, WPI	Prof. Sayrafian Kamran, NIST

To my family.

ABSTRACT

Wireless video capsule endoscopy has been in use for over a decade and it uses radio frequency (RF) signals to transmit approximately fifty five thousands clear pictures of inside the GI tract to the body-mounted sensor array. However, physician has no clue on the exact location of the capsule inside the GI tract to associate it with the pictures showing abnormalities such as bleeding or tumors. It is desirable to use the same RF signal for localization of the VCE as it passes through the human GI tract.

In this thesis, we address the accuracy limits of RF localization techniques for VCE localization applications. We present an assessment of the accuracy of cooperative localization of VCE using radio frequency (RF) signals with particular emphasis on localization inside the small intestine. We derive the Cramer-Rao Lower Bound (CRLB) for cooperative location estimators using the received signal strength(RSS) or the time of arrival (TOA) of the RF signal. Our derivations are based on a three-dimension human body model, an existing model for RSS propagation from implant organs to body surface and a TOA ranging error model for the effects of non-homogenity of the human body on TOA of the RF signals. Using models for RSS and TOA errors, we first calculate the 3D CRLB bounds for cooperative localization of the VCE in three major digestive organs in the path of GI tract: the stomach, the small intestine and the large intestine. Then we analyze the performance of localization techniques on a typical path inside the small intestine. Our analysis includes the effects of number of external sensors, the external sensor array topology, number of VCE in cooperation and the random variations in transmit power from the capsule.

ACKNOWLEDGEMENTS

I am extremely grateful to Professor Kaveh Pahlavan for his guidance and support not only in my research and academics but also in my life when there are struggles and choices. My work and accomplishments were only possible because of his help and encouragement. Simply, his care and advice has been much more than an advisor to me.

"There's no real bad people, only bad situations." "If the students around me are happy, I'm happy."

-Prof. K. Pahlavan

I also would like to thank the members of my thesis committee, Prof. Allen H. Levesque for always being kind enough to give valuable comments on various parts of my thesis, my published papers. Prof. Xinmin Huang for his continual assistance on the improvement of this thesis and his quick response. Prof. Sergey Makarov for his guidance and support throughout my studies at WPI and Prof. Kamran Sarafian for his valuable suggestions and comments during my research. I would also like to extend my thanks to Prof. Yehia Massoud for his generous support as the department head.

I would also like to express my appreciation to Dr. David R. Cave from Umass medical center for introducing us to the field of VCE localization and educating us with his knowledge in this field. Our discussions contributes a lot to this dissertation.

I would like to extend my sincere thanks to former and current members of CWINS: Dr. Mohammad Heidari, Dr. Nayef Alsindi for introducing me to a new field of research as well as helping me get familiar with the lab, and Dr. Ferit Ozan Akgul for the extensive measurements we took at WPI, the times we spent in the lab, for the guidance and help, and Ruijun Fu for the measurements, projects we did together, Umair Khan, Jie He, Pranay Swar, Kaveh Ghaboosi for the help and discussion in the lab and the current members Guanqun Bao, Jin Chen, Yishuang Geng, Zhuoran Liu for their help

and support.

I would like to thank Worcester Polytechnic Institute for providing the environment and support, and Skyhook Wireless, National Institute of Science and Technology (NIST) for their funding that made most parts of this thesis possible.

Finally, words would be insufficient to express my indebtedness to my wife Min Ni for her support, encouragement and motivation; My mother Xingyue Wang and father Yuezhong Ye for their moral and physical support through the years that made this possible.

TABLE OF CONTENTS

LIST OF TABLES

LIST OF FIGURES

LIST OF ABBREVIATIONS

Abbreviation	Meaning
AOA	angle of arrival
BAN	body area network
CRLB	Cramer Rao Lower Bound
CSIR	channel state information at the receiver
CSIT	channel state information at the transmitter
DME	distance measurement error
DFE	decision-feedback equalization
DMT	diversity-multiplexing tradeoff
DP	decision point
DSTC	distributed space-time code
DSFC	distributed space-frequency code
FFF	feed forward filter
FBF	feedback filter
GI	gastro intestinal
ISI	intersymbol interference
LMS	least mean square
MPCs	multipath components
MIMO	multiple-input multiple-output
MLSE	maximum-likelihood sequential estimation
MMSE	minimum mean square error
NIST	national institute of science and technology
OFDM	orthogonal frequency-division multiplexing
PDF	probability density function
QAM	quadrature amplitude modulation
RSS	received signal strength
SIMO	single-input multiple-output
SNR	signal-to-noise ratio
STBC	space-time block code
TOA	time of arrival
VCE	video capsule endoscopy

LIST OF SYMBOLS

Symbol	Meaning
$\boldsymbol{e}_i$	Unit canonical vector
$\mathbf{0}_{m\times n}$	$m \times n$ matrix of all 0's
$\mathbf{1}_{m\times n}$	$m \times n$ matrix of all 1's
$\boldsymbol{I}_n$	$n \times n$ identity matrix
$\otimes$	Kronecker product (i.e. matrix direct product)
$\times_n$	n-mode tensor/matrix product
$(\cdot)^\top$	matrix transpose
$(\cdot)^H$	matrix conjugate transpose
$[\boldsymbol{S}]_i$	ith column of matrix $\boldsymbol{S}$
$[\boldsymbol{S}]_{i,j}$	i,jth entry of matrix $\boldsymbol{S}$
$\mathrm{sgn}(\cdot)$	signum function
$\mathrm{diag}(\boldsymbol{x})$	Square diagonal matrix with vector $\boldsymbol{x}$ along diagonal
$\mathrm{diag}(\boldsymbol{A})$	Vector resulting from extraction of diagonal elements of $\boldsymbol{A}$
$\lceil\cdot\rceil, \lfloor\cdot\rfloor$	round up, down to nearest integer
$\mathrm{tr}(\cdot)$	matrix trace
$\Re\{\cdot\}$	Extraction of real-valued component
$\nabla_{\boldsymbol{f}}$	Gradient with respect to $\boldsymbol{f}$
$\|\|\boldsymbol{x}\|\|_p$	ℓ_p norm
$E[\cdot]$	Expectation
$\delta[\cdot]$	Discrete Kronecker delta function

Chapter 1

Introduction

Many of the profound innovations in science and engineering start with metaphors presented in science fiction. The wireless information networking industry was motivated by the Captain Kirk;s communicator in the 1960s science fiction series "‘ Star Trek"‘. The idea was formed in the early 1980s; the Federal Communications Commission (FCC) released the Industrial, Scientific and Medical (ISM) bands; the IEEE 802.11 standardization committee created the WLAN standard in 1997 [63, 67]. After almost half a century, modern smart phones are what the evolution of the "‘ Star Trek"’ communicator fantasy brought to us. Recently, another 1960s science fiction, the "‘ Fantastic Voyage"’, in which a space craft with its crew were shrunken to become a micro-device capable of traveling inside human body to remove a brain clot, has stimulated a new wave of innovations science and engineering for the body area networking (BAN). That space craft lost its navigation capabilities and went through an unguided dramatic traveling experience within the human body before it exits through tears from the eye of the human subject. Today, endoscopy capsules [26] are traveling inside the digestive system in the same way as the space craft in the fantastic voyage traveled and one can envision emergence of a number of other similar applications for micro-robots inside the human body . We don't have the technology to shrink the people; however, we have enough of remote control capabilities that we can have robots do operation inside body

without an operator inside the craft.

Since the study presented in this thesis is related to in-body localization, our focus will be on the localization aspects of the body area network and we will present channel modeling challenges for time-of-arrival(TOA) and received-signal-strength (RSS) based localization techniques; the calculation of Cramer-Rao-lower-bound (CRLB) for RF localization accuracy limitation inside the human gastro-intestinal (GI) tract, and the performance of TOA and RSS based localization techniques for various topology of body mounted receiver sensors, the number of capsules inside the GI tract for cooperation, and the effect of randomness in the transmitted power on the accuracy of capsule localization.

1.1 Evolution of Video Capsule Endoscopy (VCE)

In the past decade, miniaturization and cost reduction of semiconductor devices have allowed the design of small, low cost computing and wireless communication devices used as sensors in a variety of popular wireless networking applications and this trend is expected to continue in the next few decades [64], [36]. One of the leading wonders of this wireless networking breakthrough is the emergence of wireless video capsule endoscopy (VCE) [18]. The technology was introduced by the Given Imaging Yoqneam, Israel in 2000.and the U.S. Food and Drug Administration (FDA) approved its clinical use in 2001. Examination of the Gastro-Intestinal (GI) tract using VCE is commonly used for a number of diseases such as the inflammatory bowel disease, the ulcerative colitis and the colorectal cancer [46]. VCE provides a unique visualization of bleedings and tumors in the middle parts of the small intestine, where traditional endoscopy

and colonoscopy visualization techniques can not reach [55]. Small intestine is a 5-8 meters long curled path occupying the central part of the GI tract, therefore, the path of movement of the VCE inside the small intestineis very complex. Wireless video capsule endoscopy has been in use for over a decade and it uses radio frequency (RF) signals to transmit approximately fifty five thousands clear pictures of inside the GI tract to the body-mounted sensor array.

Wireless capsule endoscopy begins with the patient swallowing the capsule. The natural peristalsis moves the capsule smoothly and painlessly throughout the GI tract while it is transmitting color images taken by the camera at a rate of two images per second [26]. The VCE images allow the physician to visualize the entire GI tract without scope trauma and air insufflations. Comparing with the traditional gastroscopy and colonoscopy techniques, the VCE procedure is ambulatory allowing the patients to continue with their daily activities throughout the endoscopic examinations. In addition, the traditional techniques can only reach the first few or last several feet of the small intestine, while VCE provides images of the entire GI tract.

However, physician has no clue on the exact location of the capsule inside the GI tract to associate it with the pictures showing abnormalities such as bleeding or tumors. It is desirable to use the same RF signal for localization of the VCE as it passes through the human GI tract.

1.2 Location information for Gastro-Intestinal(GI) tract

In recent years, the feasibility of several technologies for localization of the VCE has been explored. These technologies can be divided into those using magnetic field or

inertial systems, using image processing techniques and techniques using RF signals. In magnetic sensing based techniques, a magnet is inserted into the VCE and the VCE is located by measuring the magnetic field [42]. This technique increases the weight and size of the VCE and the magnetic field of the VCE used for localization will be interfered by the external magnetic fields used for other applications such as the Magnetic Resonance Imaging (MRI) systems. One can also insert radiation opaque material into the VCE and trace the location of the VCE using X-ray or Computed Tomography (CT) scan [72]. Continuous imaging using X-ray or CT scan is very expensive and it bears the health risks for the patient. Using the RF signal used for image transmissions for the VCE to also locate the capsule offers itself as a natural and low cost solution that does not add to the capsule complexity and payload. Therefore, it has been chosen for use with the smartpill capsule [86] in USA and the M2A capsule [37] in Israel. These companies use the RSS of the waveform for the purpose of localization of the VCE. A more accurate metric for localization is the TOA or the time of flight of the signal.

For RF based localization, a widely known benefit of TOA based techniques is their high accuracy compared to RSS based techniques. The TOA based technique relies on measurements of travel time of signals between the known reference nodes and unknown terminal nodes. Ranging information is calculated by multiplying the propagation velocity of RF signal and the measured TOA value. The testbed developed in [40] can be used to examine the performance of TOA localization in indoor areas under the influence of multipath scenario. On the other hand, the human body is formed of various organs with complex structures. Each organ has a unique characteristics of conductivity and relative permittivity. Since propagation velocity inside human body is expressed as a function of the relative permittivity, medical implanted devices placed in different positions cause different propagation velocities due to the RF signal traveling through

various tissues or organs. These variations in the speed is dominant source of error for TOA-based RF localization inside the human body. Some preliminary two dimensional (2D) RSS and TOA localization techniques for inside the human body have been reported in [49], [37]. However, there is nothing available in the literature to compare the performances of the performances of the two approaches in particular in a realistic 3D scenario.

1.3 Motivation

Our aim is to use the CRLB to analyze the RF localization accuracy that is achievable in the various organs in the GI tract and determine if these accuracies are enough for clinical capsule endoscopy applications. The CRLB has been used traditionally for the analysis of the accuracy of outdoor localization using GPS and for a variety of indoor geolocation applications for the human and robotics applications [10]. The CRLB uses the ranging error models for the behavior of the localization metrics such as RSS and TOA to estimate the bounds. Currently, most of the researchers have focused on developing the algorithms and mathematical models for solving the triangulation problem [13, 27]. In this paper, we take a different approach. We focus on the accuracy possible for VCE in the GI tract using RSS or TOA based triangulation technique. We have developed the RSS localization bound calculation for single VCE situation in our previous work [97].

Understanding the nature of signal propagation is the key to the design of efficient and low-power, low-cost communication systems and precise localization for the BANs. Therefore, the first step in research is to start a measurement and modeling program to understand the nature of signal transmission inside the human body. Today, the existing

literature in measurement and modeling for understanding the propagation in and around human body is fragmented and it does not pay attention to localization inside body for emerging applications such as localization of endoscopy capsules [91]. There is a need for research in understanding the behavior of RF signal propagation inside human body for localization applications.

1.4 Contributions

In this thesis, we address the accuracy limits of RF localization techniques for VCE localization with particular attention to localization inside the small intestine. Fundamentally, RF localization is either based on the traditional RSS or the more accurate TOA [65]. The limited existing literature is focused on developing algorithms and mathematical models for solving the triangulation problems [30], [49]. The Cramer Rao Lower Bound (CRLB) has been used traditionally for the analysis of accuracy of outdoor localization using GPS and for a variety of indoor geolocation applications for the human and robotics applications. In this thesis, we apply this analytical framework for calculation of the CRLB for comparative performance evaluation of the RSS- and TOA- based cooperative localization using multiple capsules in the three major organs of the GI tract as well as to assess the accuracy of these techniques as the VCE moves along the complex path of movements inside the small intestine. Analytical results presented in this thesis includes the effects of number of external sensors; the external sensor array topology, number of VCEs in cooperation and the random variations in transmit power from the capsule.

The primary contribution of this thesis is the calculation of CRLB for capsule en-

doscopy applications using an existing path loss model and a novel TOA ranging error model developed in this thesis.

The thesis draws substantially from results presented previously in:

1. Yunxing Ye, Umair Khan, Nayef Alsindi, Ruijun Fu, Kaveh Pahlavan, ”On the accuracy of RF positioning in multi-capsule endoscopy” in IEEE Personal indoor and Mobile Radio Communications (PIMRC),2011 IEEE 22nd International Symposium on 2011/9/11.

2. Kaveh Pahlavan, Yunxing Ye, Umair Khan, Ruijun Fu, ”RF localization inside human body: Enabling micro-robotic navigation for medical applications” in Localization and GNSS(ICL-GNSS), 2011 International Conference on 2011/6/29

3. Yunxing Ye, Pranay Swar, Kaveh Pahlavan, Kaveh Ghaboosi, ”Accuracy of RSS-Based RF Localization in Multi-capsule Endoscopy” in International Journal of Wireless information Networks (IJWIN), volumn 19, issue 3, page 229-238

4. Ruijun Fu, Yunxing Ye, Ning Yang, Kaveh Pahlavan, ”Doppler spread analysis of human motions for body area network applications”, in Personal Indoor and Mobile Radio Communications (PIMRC), 2011 IEEE 22nd International Symposium on, 2011/9/11.

5. Kaveh Pahlavan, Yunxing Ye, Ruijun Fu, Umair Khan, ”Challenges in Channel Measurement and Modeling for RF Localization Inside the Human Body”. in International Journal of Embedded and Real-Time Communication Systems (IJERTCS) volumn 3, issue 3, page 18-37.

6. Ruijun Fu, Yunxing Ye, Kaveh Pahlavan, ”Characteristic and Modeling of Hu-

man Body Motions for Body Area Network Applications", in International Journal of Wireless Information Networks, volume 19, issue 3, page 2190-228.

7. Pranay Swar, Yunxing Ye, Kaveh Ghaboosi, Kaveh Pahlavan, "On effect of transmit power variance on localization accuracy in wireless capsule endoscopy". in IEEE Wireless Communications and Networking Conference (WCNC), 2012/4/1.

8. Guanqun Bao, Yunxing Ye, Umair Khan, Xin Zheng, Kaveh Pahlavan, "Modeling of the Movement of the Endoscopy Capsule inside GI Tract based on the Captured Endoscopic Images" in International Conference on Modeling, Simulation and Visualization Methods, MSV'12. July 16-19, 2012, Las Vegas, USA.

9. Kaveh Pahlavan, Guanqun Bao, Yunxing Ye, Sergy Makarov, Umair Khan, Pranay Swar, David cave, A Karellas, Prishant Krishnamurthy, Kamran Sayrafian, "RF Localization for Wireless Video Capsule Endoscopy" in International Journal of Wireless Information Networks.

10. Jin Chen, Yunxing Ye, Kaveh Pahlavan, "UWB characteristics of creeping wave for RF localization around the human body" in IEEE 23rd Personal Indoor and Mobile Radio Communications (PIMRC), 2012, 2012/9/9.

1.5 Outline of the Dissertation

This dissertation focuses on the comparative performance evaluation of TOA- and RSS-based RF localization for VCE localization. In chapter 2, we first give an overview of the cooperative VCE localization which includes the system aspect of RF VCE localization system, the RF positioning metrics, the existing VCE localization techniques, the

challenges in VCE localization and the measurement campaign we conducted for channel characterization. In chapter 3, we introduce the performance evaluation scenario and the implant to body surface path loss model for RSS based VCE localization. In chapter 4, we present our novel TOA ranging error model caused by human tissue inhomogeneity and show the modeling results. In chapter 5, we first derive the 3D Cramer Rau Lower Bound (CRLB) for single capsule localization in 3D space and then extends the the derivations to multiple capsule cooperative localization, we derived the CRLB when there's randomness in the transmitted power in the end of this chapter. In chapter 6, we present the results and discussion which includes the effect of organ shape and location, the effect of number of receiver sensors, the effect of number of capsules in cooperation, the effect of randomness in transmitted power and the accuracy limit along the small intestine. In chapter 7,we introduce the VCE movement model and the application of tracking techniques in the VCE localization. Finally, we conclude the dissertation in chapter 8 and give the suggested direction of future work.

Chapter 2

Overview of Cooperative VCE Localization

In this chapter, we discuss the system engineering and channel aspects of capsule endoscopy localization systems. We also present the major challenges for RF localization [98]in VCE in this chapter.

Given the free intraperitoneal location of the small intestine and its constant peristalsis, accurate localization of pathology is very difficult [57]. Because wireless endoscopy is usually used for diagnostic puorse, surgical intervention may be necessary for follow up procedures. Accurate location information is vital for the follow up interventions.

2.1 Overview of capsule endoscopy localization system

The triangulation [100]method of localization of the wireless capsule endoscope was initially introduced in 2001 [30]. The system used by GIVEN Imaging [99] is shown in Fig. 2.1

The transmitted signal of the capsule is received by eight sensors attached to the patient's abdomen. Its location is estimated by three sensors at any given time: The sensor in closest proximity to the capsule receives the strongest signal, and two adjacent sensors, which the capsule is located in between, will receive signals of nearly equivalent

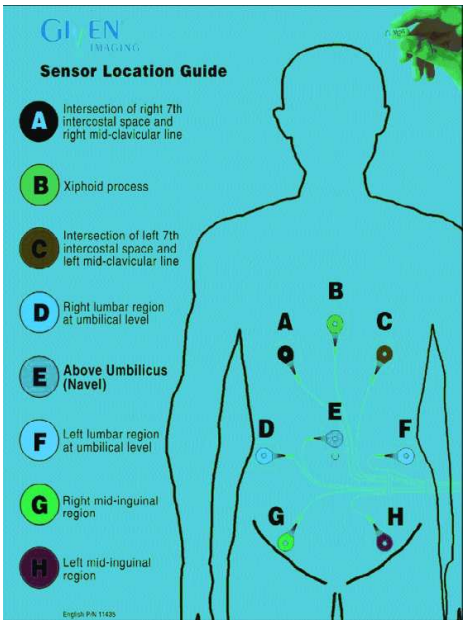

Figure 2.1: The sensor array location guide, from GIVEN Imaging

strength. Using the strength of the signals and location of the sensors, an approximate location can be calculated. It is reported in [54] that this system detected the capsule within 6 cm of its location in the abdomen 87% of the time in healthy volunteers who also received fluoroscopy. However, this method does not indicate the actual distance down the small intestine. Therefore, patients with small intestine lesions still require surgical intervention to precisely localize the lesion.

2.2 RF Positioning Metrices

Wireless localization sensors operating in different environment measure RSS, AOA, POA, TOA, and the signature of the delay power profile as location metrics [66], [34].

2.2.1 AOA based techniques

In AOA-based indoor geolocation, directional antenna or antenna arrays are used to triangulate the MT [52] [82]. Two or more reference points (RP) are needed to determine the axis value of the MT as shown in Fig 2.2 Commonly, measurements of POA [17]and AOA in large indoor and urban areas provide very unreliable results due to severe multipath propagation and heavy shadow-fading conditions. The accuracy of the

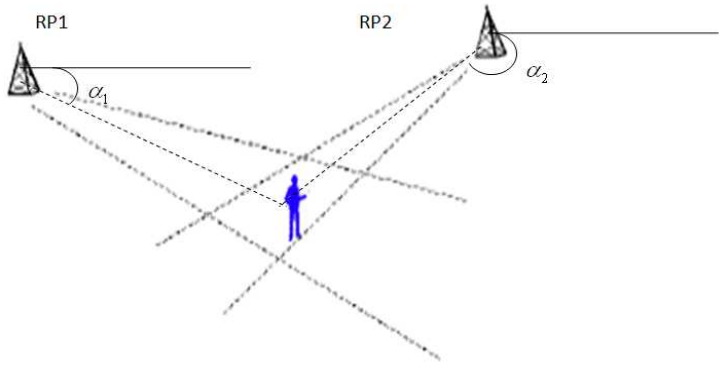

Figure 2.2: AOA technique for geolocation

AOA measurement system is determined by the resolution of the directional antenna or antenna array and the algorithms used to estimate the AOA simultaneously. Given the accuracy of AOA measurement system, the number of reference points is determined by the MT position with respect to the reference points. When the MT lies between the two reference points. AOA measurements will not be able to provide the exact location of MT on the line between the two reference points. Hence, more than two reference points are normally needed to improve the location accuracy.

2.2.2 RSS based techniques

The first RSS-based indoor geolocation system is the RADAR [14]. In RSS-based indoor geolocation, the distance between the RP and MT can be calculated using the measured power and a distance-power relationship. In wideband measurements, the effects of multipath fading are averaged over the spectrum of the signal. For narrowband systems, where we have only one arriving pulse with fluctuating amplitude according to the multipath fading characteristics, we need to average the signal over a longer period to make sure that the multipath fading is averaged out [68]. There are plenty of statistical models for relating RSS to the distance, which are developed mainly for telecommunication applications. The common principle behind all statistical models for calculating the RSS in a distance d is given by [68]:

$$RSS_d = 10log_{10}P_r = 10log_{10}P_t - 10\alpha log_{10}d + X \tag{2.1}$$

where P_t is the transmitted power, d is the distance between the transmitter and the receiver, and α is the distance-power gradient of the environment. The random variable X. The path loss model in indoor environment is highly site-specific. For example, the value of power-distance gradient, which is a parameter of path loss model, varies in a wide range between 15-20dB/decade and a value as high as 70dB/decade. Moreover, the shadow fading [35] will decrease the stability of RSS value further. As a result, the distance calculated from RSS is not very reliable. An alternative solution is the ray-tracing algorithms which can provide much more reliable RSS by using the layout of the building [68]. However, the drawback of ray-tracing algorithms is the computational complexity and the labor cost of getting the fine grained building floor plan as well as information of construction material.

2.2.3 TOA based techniques

The TOA-based system measure distance based on an estimate of signal propagation delay between a transmitter and a receiver since in free space or air, radio signals travel at the constant speed of light [44]. The TOA can be measured by either measuring the phase of received narrowband carrier signal or directly measuring the arrival time of a wideband narrow pulse [66]. The important parameters for TOA-based localization system are the TOA of the direct line of sight (DLOS) path [93] since it is the direct representation of the physical distance between the transmitter and receiver [48], [47]. An example of the indoor multipath and the geolocation specific parameters is shown in Fig 2.3. In narrowband ranging technique [81], the phase of a received carrier signal, ϕ,

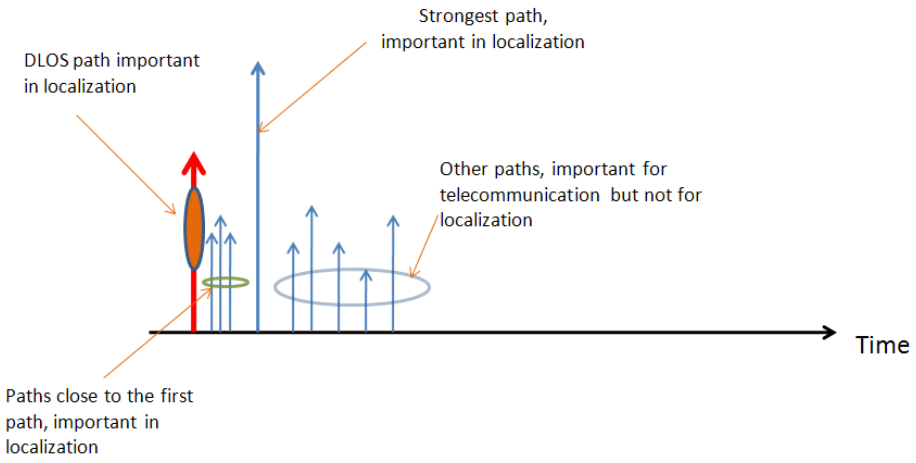

Figure 2.3: Multipath profile and important paths for geolocation

and the TOA of the signal, τ, are related by $\tau = \phi/\omega_c$, where ω_c is the carrier frequency in radian. In outdoor scenario applications such as GPS, the DLOS path always exists, accurate measurement of the carrier phase is possible. But in indoor environments,

the severe multipath environment causes huge measurement errors even larger than the actual distance between the transmitter and receiver. Therefore, the conclusion is that the phase-based distance measurement using narrowband carrier signal is not a suitable solution for indoor geolocation.

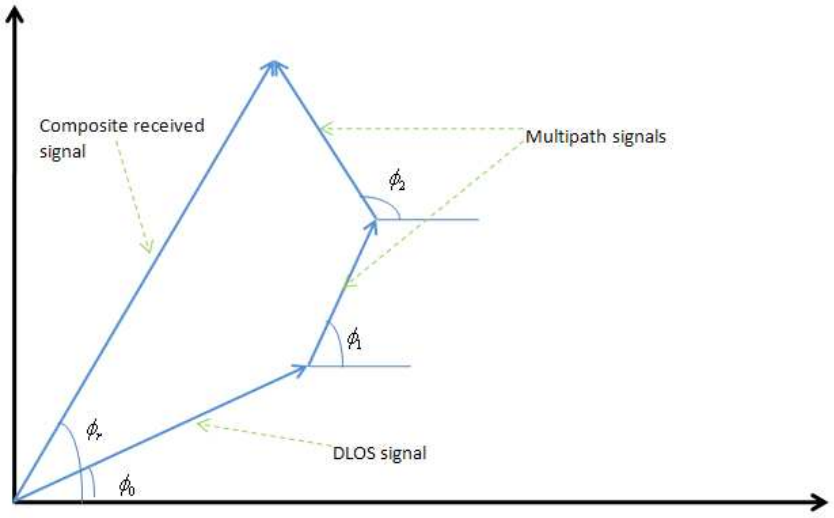

Figure 2.4: Phasor diagram for narrowband signaling on a multipath channel

Another widely used technique is the wideband signal approach where the direct sequence spread spectrum (DSSS) [89] method is the most commonly used form, as this technique performs better than competing systems at suppressing interference [58] [83]. In such a system a known pseudo-noise (PN) signal, which is modulated using a modulation technique (such as BPSK, QPSK, etc), is multiplied by the carrier signal, which is thus replaced by a wide bandwidth signal with a spectrum equivalent to that of the noise signal.

Usually, in order to measure the time of arrival of the signal, a sliding correlator or

a matched filter is used at the receiver which cross-correlates the received signal with a stored reference PN sequence. The arrival time of the first correlation peak is used as the time measurement.

Due to the scarcity of the available bandwidth in practice, DSSS ranging systems may not be able to provide adequate accuracy. On the other hand, it is always desirable to achieve higher ranging accuracy using the same bandwidth. Inspired by high resolution spectrum estimation techniques, a number of researchers have studied super-resolution techniques for time-domain analysis such as [96].

Finally, the most recent accurate and promising technique is the UWB approach [53]. As the bandwidth of UWB systems is usually several GHz, the ranging accuracy is of the order of centimeter. This fact can be justified from equation:

$$d = \frac{c}{BW} \tag{2.2}$$

where d denotes the absolute resolution, and BW is the bandwidth of the signal. The large bandwidth of UWB systems means that they are able to resolve multiple paths and combat multipath fading and interference. However, such systems have a limited range and building penetration, due to the high attenuation associated with the high-frequency content of the signal. From our measurement experience, the coverage range of UWB signal for obstructed line of sight (0LOS) scenario is only about 16 meter. The actual deployment of the UWB systems in the US is subject to the FCC approval. The main concern of the FCC authorities is the interference of the UWB devices to, among other licensed services such as GPS systems operating at 1.5GHz frequency band. A significant amount of research work is under way to assess the effect of the UWB interference on the GPS receivers.

2.3 Cooperative Localization in Wireless Sensor Networks

The network localization generally consists of two phases, namely the measurement phase and the location estimation phase [94] [11]. In the previous section, we have introduced the techniques used in the measurement phase. It is important to mention here the location accuracy also heavily depends on the relative geometry of the unknown node (capsule here) to the reference nodes. The major difference between traditional localization and wireless sensor network localization is the cooperative localization.

In a noncooperative localization approach, there is no communication between the unknown nodes (capsules), only between the unknown node and the reference nodes. Every unknown node need to communicate with multiple reference nodes, requiring either a high number of reference nodes or long -range reference nodes transmissions as shown in Figure 2.5.

In cooperative localization, we still allow the unknown nodes to make measurements with the reference nodes, but in cooperative localization, we additionally allow unknown nodes to make measurements with each other unknown nodes as shown in Figure 2.6. Inter-node communication removes the need for all unknown nodes to be within communication range of multiple reference nodes. Thus, high reference nodes density or long-range reference node transmissions are no longer required. The extra information gained from these measurements between the pairs of unknown nodes can offer an increased accuracy and coverage for the overall system.

The formulation of the ”cooperative localization problem” is give in [70]. Consider a sensor network S consisting of a set of $m > 0$ nodes labeled 1 through m that represent the reference nodes together with $n - m > 0$ additional nodes labeled $m + 1$

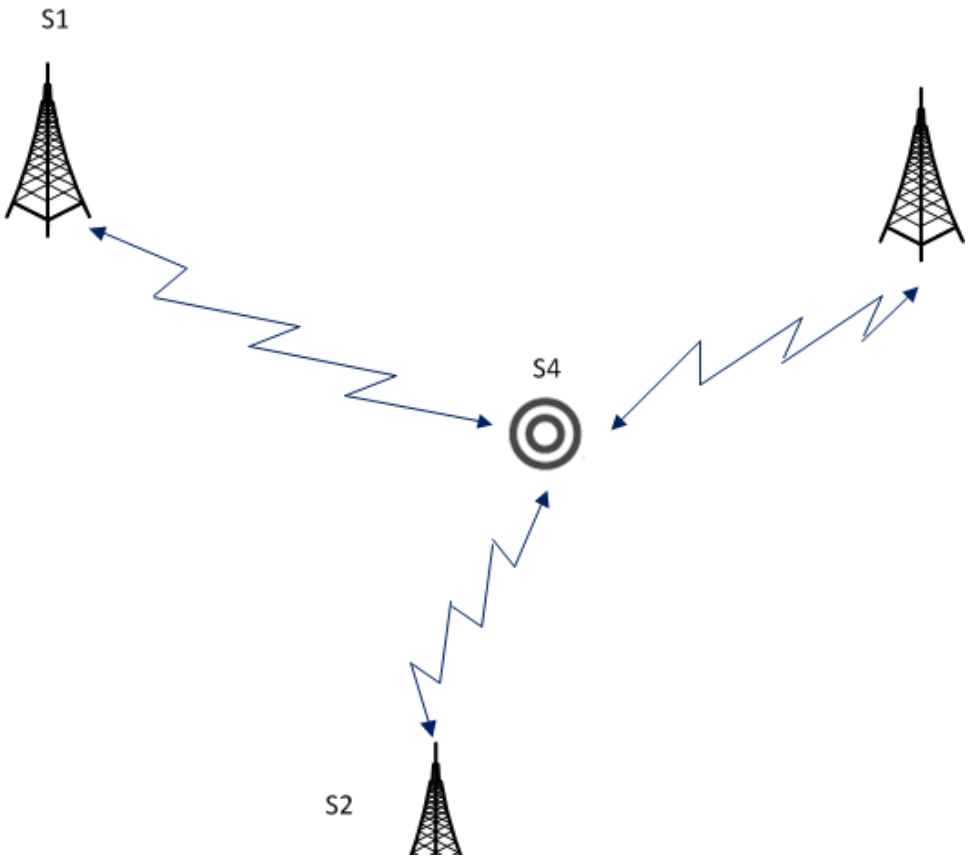

Figure 2.5: Noncooperative localization

through n that represent the unknown nodes. Let $\mu_{i,j}$ between certain pairs of nodes s_i, s_j be given, and suppose that the coordinates p_i of the reference nodes s_i are known. The cooperative localization problem is finding the coordinates of the unknown nodes such that the assignment of the coordinates of unknown nodes is consistent with the measurements $\mu_{i,j}$ and is consistent with the reference coordinates.

In general, there are two main approaches to achieve the cooperative localization. The first is centralized and the second is distributed.

In centralized cooperative localization [50], the central processor collects measurements before calculation. The positions of all nodes are determined by a central proces-

sor. This processor collects measurements from the reference points as well as unknown nodes and computes the positions of all unknown nodes.Centralized systems are usually not scalable and thus impractical for large networks. Then main advantage of centralized system is that they tend to provide more accurate location estimates than those provided by distributed systems. In the literature, there exist three main approaches for designing centralized distance-based localization systems: multidimensional scaling (MDS), linear programming, and stochastic optimization approaches. It is relevant to note for MDS that it is a centralized system in its raw form, though recent study has attempted to break away from this restriction [79].

In distributed cooperative localization system, there is no central controller, and every node infers its own position based only on locally collected information. Distributed systems are scalable and thus attractive for large localization networks. Distributed algorithms for cooperative localization generally fall into one of two categories, namely, ”network multilateration” and ”successive refinement” [70].

2.4 Summary of existing localization techniques for VCE

Various technologies for localization of the capsule have been explored in feasibility studies. The original idea is to use a spatially scanning system to locate the points with the strongest RSS. The system is non-commercial and cumbersome. Frisch et al [30] developed a RF triangulation system using an external sensor array that measures signal strength of capsule transmissions at multiple points and uses this information to estimate the distance. The average experimental error is reported to be 37.7mm [27]. Kuth et al. [72]proposed a method for determinning the position of and orientation of the

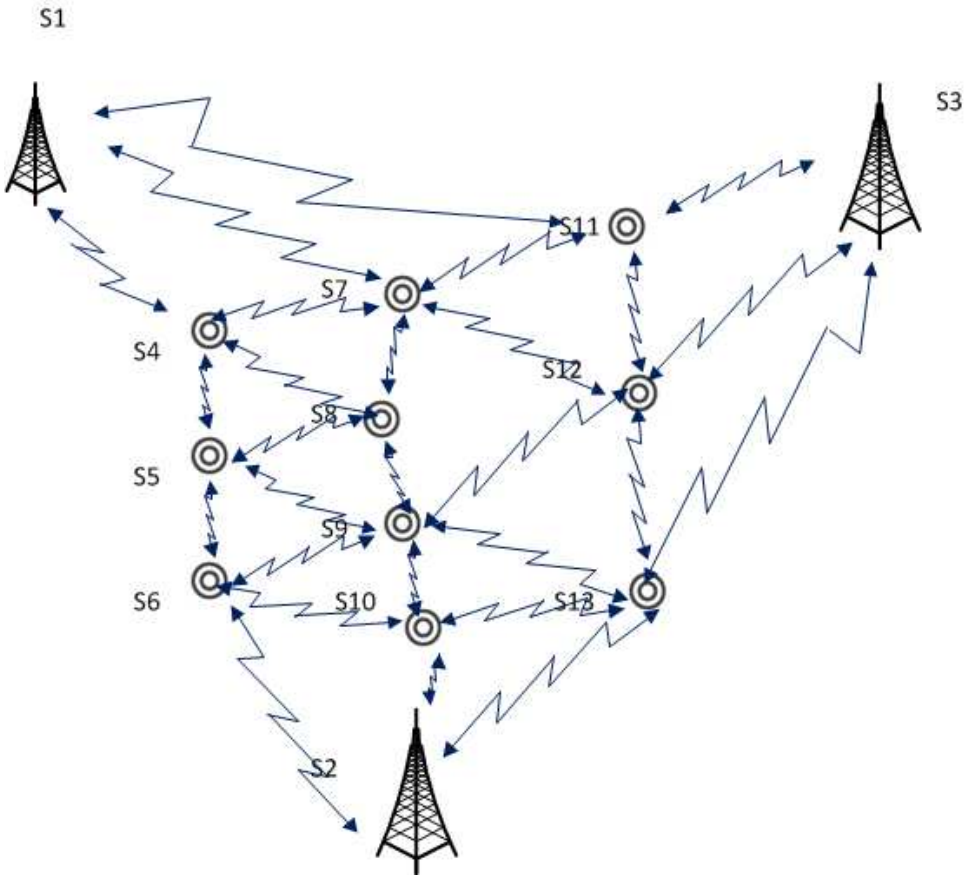

Figure 2.6: Cooperative localization

capsule by means of X-ray radiation image processing. In this case, the capsule can be seen unambiguously since it has a multiplicity of radiation-opaque elements which are usually metallic or plastic and show a very clear image. Thus, it is possible to operate with an extremely low radiation dose in order to reduce the health risks on the patients. Makoto et al. [49]disclosed a method for finding the location of medical implant devices by using the time of arrival (TOA) based pattern recognition method. First, the propagation speed of signal inside human body is estimate by processing the images from CT or MRI system. Then, an adaptive template synthesis method is applied to calculate the prapagation time based on the output of the correlator between the transmitter and the receiver. Other techniques developed for capsule localization include magnetic field

sensing [42], [43]. A small permanet magnet is enclosed into the capsule. With the sensing data of magnetic sensor array outside the patient's body, the 3D location and 2D orientation of the capsule are estimed. Inertial system has also been used for capsule localization [32]. In this work, a $3 \times 3mm$ digital triaxial accelerometer, which operates at 20Hz, was integrated within the capsule and data was transmitted over Zigbee technology to an external computer. Since the acceleration is directly measured, velocity can be obtained more accurately than position because it requires only a single integration. Since identifying the physical location of each capture of capsule photo is important in both diagnostic and therapeutic applications of WCEs.

Among these technologies, RF signal based localization systems have the advantage of application-non-specific and relatively low cost for implementation. Therefore, it has been chosen for use with the Smartpill capsule [86] [38] in USA and the M2A capsule [37] in Israel. Generally, the RF localization technique is based on TOA, angle of arrival (AOA) or received signal strength (RSS) measurements. A widely known benefit of TOA based techniques is their high accuracy compared to RSS and AOA based techniques. However, the strong absorption of human tissue causes large errors in TOA estimation and the limited bandwidth (402-405MHz) of the Medical Implant Communication Services (MICS) band prevent us from high resolution TOA estimation. The problem is made even worse by the GI movement, and the filling and emptying cycle, resulting in unpredictable ranging error [90]. Thus, the ranging information from TOA estimation is not promising with the current technology.

The RSS based techniques are less sensitive to bandwidth limitation and harsh propagation environment.There are basically two ways to use the the RSS information for localization, triangulation and pattern recognition. In this paper, we only address the

issues related to RSS triangulation techniques. RSS Triangulation technique is based on the path loss model from implant tissues to body surface. The model is used to calculate the distance between each external sensor and the capsule, then at least 4 link distances are used to calculate the location of the capsule in 3D space.

2.5 Challenges for RF localization in VCE

The most challenge problem in capsule localization comes from the complexity of the environment where the capsule travels through. Since the GI tract is a long tubular structure that folds upon itself many times and is free to move within the abdominal cavity [45], it is very difficult to accurately localize the capsule. Meanwile, due to the activities of patient and body passive motions such as repiration, the absolute location of sensors on the surface of the body and their relative positions to the capsule inside body keep varing, making the definition of localization different from traditional scenarios [3] [60]. Currently, most of the researchers have focused on developing the algorithms and mathematical models for solving the triangulation problem [27], [13]. In this paper, we take a different approach. Based on the statistical implant path loss model developed in [76], we focus on the accuracy possible for capsules in the GI tract using RSS based triangulation technique, Yi etc have developed the localization bound calculation for single pill situation in [91]. The CRB presented in this paper quantify the limits of localization accuracy with certain reference-points topology, implant path loss model and number of pills in cooperation. Our aim is to analyze the accuracy achievable at various organs and determine if the accuracies are enough for endoscopy applications. Similar works have been done for indoor geolocation applications [10] and robot localization applications [16].

2.6 Measurement Campaign for Channel Characterization

In this section, the ultra-wide-band (UWB) measurement [74]campaign around the human body and a phantom as well as the measurements inside a phantom will be presented. By analyzing certain channel parameters such as, TOA, DME, RSS and total path-loss, we discuss the influencing factors when the signal traveling around the human body. We also analyze the influence of the human body on TOA ranging accuracy.

2.6.1 Measurement Campaign for Time of arrival (TOA) based Localization on Body Surface

Measurement setup: On body surface measurement campaign is performed at 3 8GHz for investigating the possibility of using time of arrival (TOA) based ranging technique for localization purpose in and around body. The core of the measurement system is the 40 GHz Agilent technologies E8363B network analyzer purchased in 2004 by NSF founding [23]. The antennas we used for measurements are small patch antennas bought from Skycross Corporation (1) (SMT-3TO10M) [39], shown as below:

The parameters we used for measurements are listed below: Transmit power: 0dBm (1mW)
Number of frequency points: 1601
IF bandwidth: 3 kHz

For the analysis of human body on TOA estimation, we evaluated 8 different antenna distances in a typical office environment. First, we measured the TOA when theres

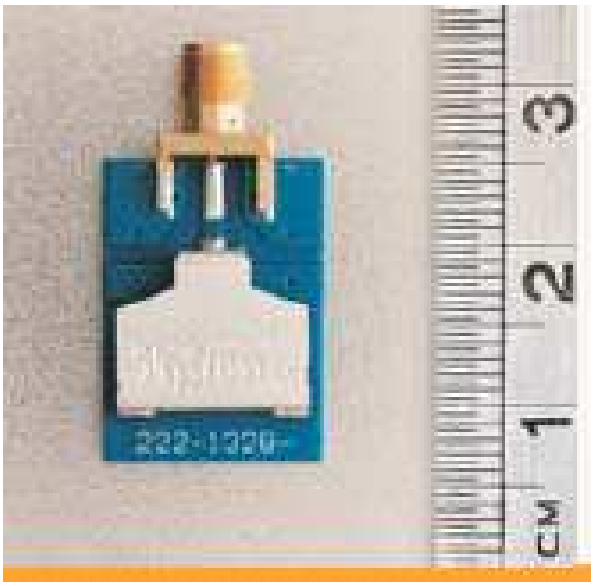

Figure 2.7: SMT-3TO10M antenna element

nothing in between the antenna pair to study the bias and noise level in our measurement system. Then we did measurements with body tissue in between the antenna pair. When processing the measured data, we first removed the bias of the system from the first step. Then we used line fitting to find out the average relative permittivity of human body in order to calculate the propagation speed of signal traveling through human body. The theory behind this method is that: the propagation velocity of a homogeneous tissue is given by :

$$v(\omega) = \frac{c}{\epsilon_r(\omega)} \tag{2.3}$$

where $c$is the velocity of light in the free space and $\epsilon_r(\omega)$is the relative permittivity of a human tissue, ω is the frequency of signal, so propagation speed is frequency dependent. After that, we use this signal speed value and measured TOA to calculate the estimated distance and compare the results with the true distance value to get the distance measurement error (DME) for TOA technique. The measurement scenarios and parameters are illustrated in figure 2.8 and table 2.9.

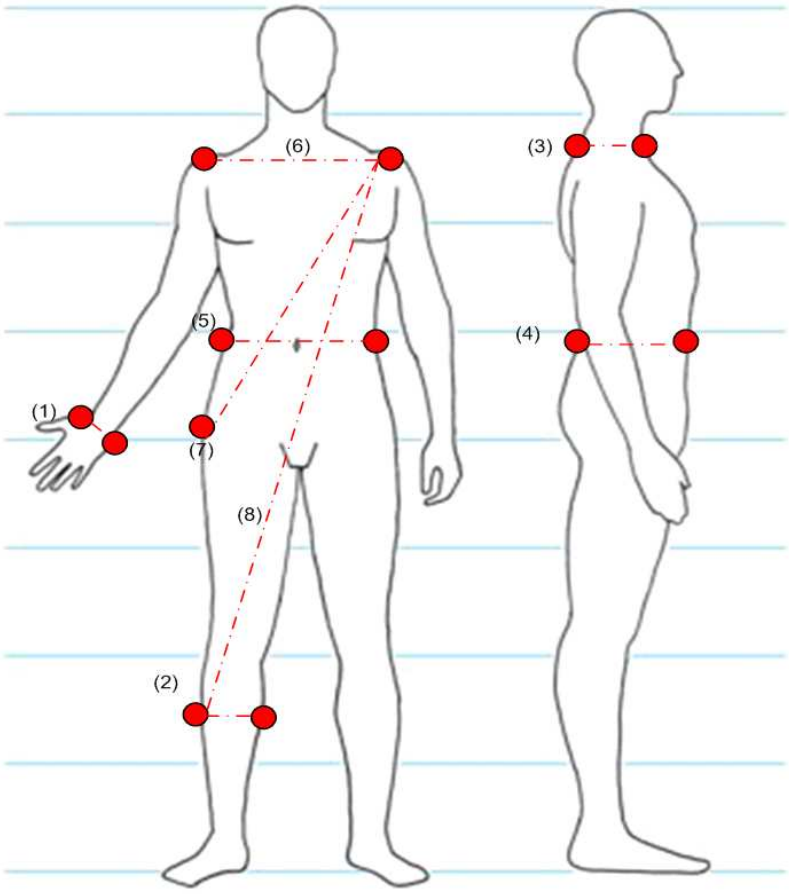

Figure 2.8: On body surface measurement scenarios

Scenario Number	Distance (cm)
(1)	**6**
(2)	**12**
(3)	**23**
(4)	**29**
(5)	**43**
(6)	**58**
(7)	**94**
(8)	**124**

Figure 2.9: measurement parameters

the results from the measurement campaign are shown in

the calculated average permittivity of human body tissue is very close to water, The

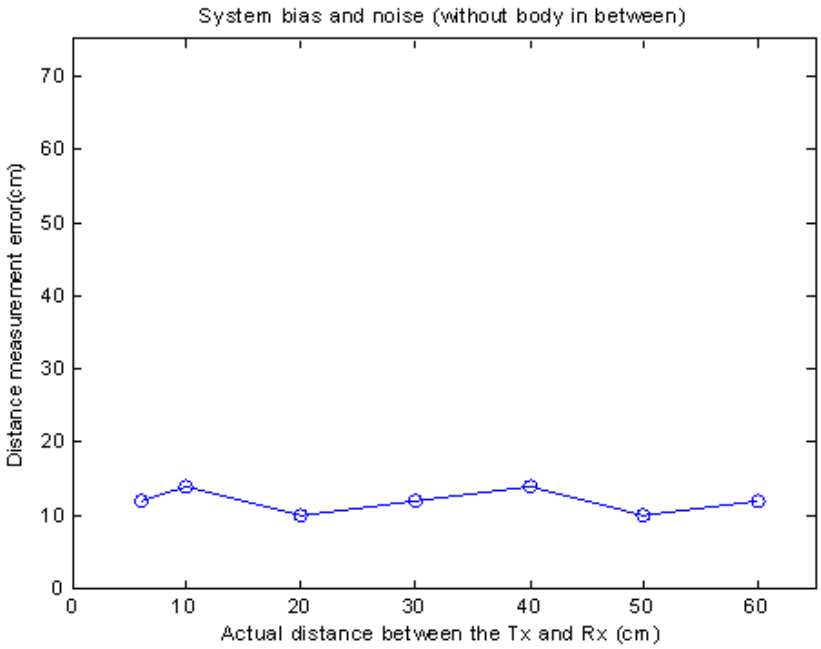

Figure 2.10: System bias and noise(without body in between)

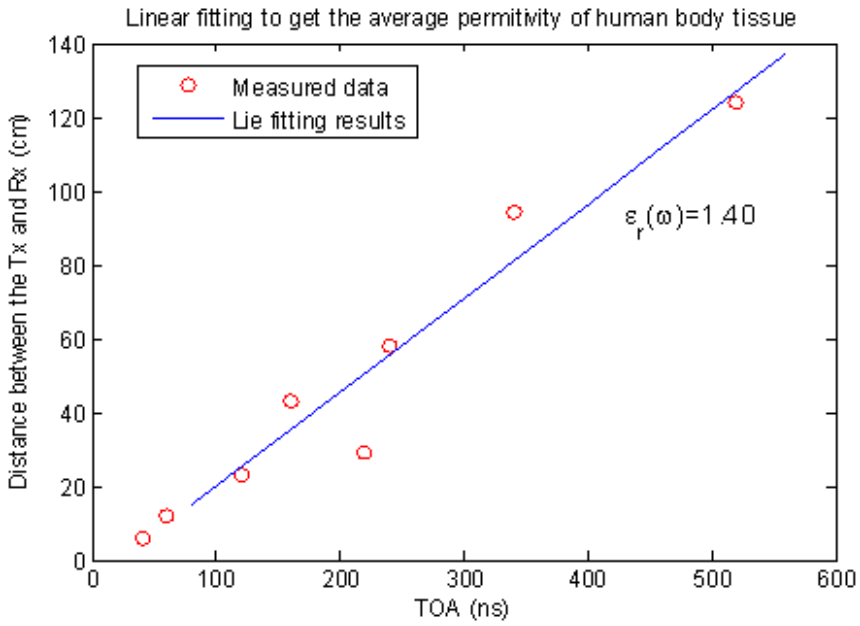

Figure 2.11: Linear fitting to get the average permitivity of human body tissue

average absolute value of DME is 7.81cm by TOA ranging, and the standard deviation of DME is 10.11cm.

Actual Distance(cm)	6	12	23	29	43	58	94	124
DME (cm)	4.14	3.21	7.43	26.78	-2.43	2.85	-7.79	7.84

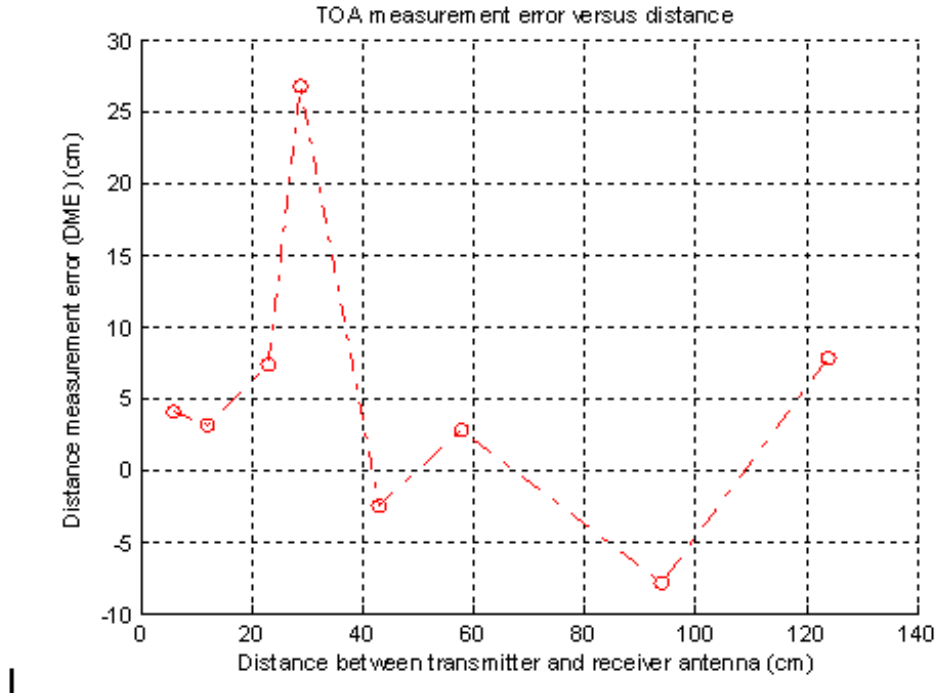

Figure 2.12: TOA measurement error versus distance

2.6.2 Implant Phantom Measurement Campaign for Time of Arrival based Localization

implant measurement campaign is performed at 2 2.4GHz for investigating the influence of body tissue and antenna polarization on the accuracy of time of arrival (TOA) based ranging technique for localization purpose inside body. The core of the measurement system is the 40GHz Agilent technologies E8363B vector network analyzer (VNA) purchased in 2004 by NSF founding. The antenna we used for measurements are small mono-pole antennas designed by center for wireless information network study

(CWINS). The parameters we used for measurements are listed below: Transmit power: 0dBm (1mW)

Frequency range: 2 2.4GHz

Number of frequency points: 801

IF bandwidth: 3 kHz

Since the dielectric property of human body tissue is close to water, we used a human body phantom filled with purified water as the measurement object in the first phase of the measurement campaign. We conducted measurements in two controlled environments. An anechoic chamber which prevents ray reflections and a typical office environment. We studied the effects of human body tissue and antenna polarization on the accuracy of TOA estimation. The measurement setup is illustrated in 2.13 Since the interaction between antenna and liquid might cause short-circuit and error to the measured results, we used shiled around the antenna when it was dropped into the liquid. Results are presented in figure 2.14, **??**, **??**, **??**, **??**. From the measured results, we can see that human tissueliquidwill casue large amount of delay in the TOA estimation, reduction in the first path power and total received power. Antenna polarization will also influence the accuracy of TOA estimation. Same polarization of transmitter antenna and receiver antenna can provide better TOA estimation accuracy.

2.6.3 Measurement Campaign for the Creeping Wave

The measurement setup is configured for conducting the measurements around the human body and a phantom [88], [12]to develop UWB channel model for various multipath components (MPCs) such as the TOA, RSS and total path-loss.

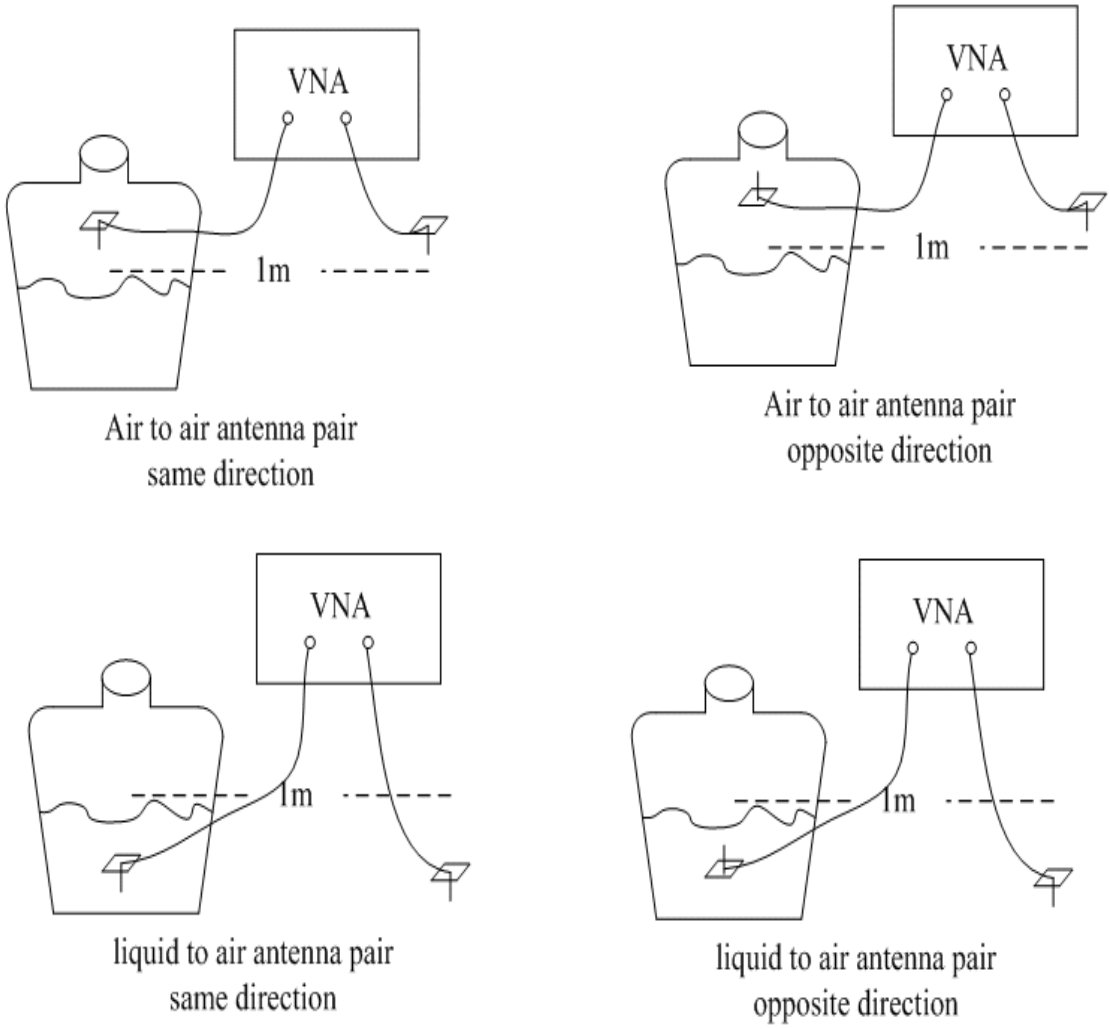

Figure 2.13: Measurement setup

All the measurements were conducted in an RF anechoic chamber, a shielded room having dimension $2.32m \times 2.41m \times 2.29m$. The interior structure of the chamber greatly attenuates any MPCs reflected from the walls, and also isolates the experimental setup from RF signals existing outside the chamber.

An E8363B Vector Network Analyzer (VNA) is employed to sweep the frequency

Scenario	$TOA \cdot C$ (Estimated Distance (m))	First path gain(dB)	Total power（dB）
Air to air, Same direction free space	0.97	-67.9	-34.0
Liquid to air, Same direction free space	2.36	-166.2	-81.8
Air to air, opposite direction free space	1.36	-73.2	-36.4
Liquid to air, opposite direction free space	2.52	-172.3	-84.3
Air to air, Same direction, chamber	0.86	63.8	-31.7
Liquid to air, Same direction, chamber	1.23	-140.3	-69.9
air to air, opposite direction, chamber	1.45	-69.2	-33.0
Liquid to air, opposite direction, chamber	2.63	-173.7	-74.8

Figure 2.14: TOA,first path gain and total power results

from 3-10GHz. The measurement parameters are listed in Table 2.1

We measured the transfer function S21 and the measurement results are stored in a PC which is wirelessly communicated with the VNA. After obtaining the frequency domain data, we first apply a hamming window on the frequency domain data to reduce the infect of side lobes and then use the inverse-chirp Z transform to convert the frequency data to the time domain impulse response. After that, we apply a peak detection algorithm to extract the MPC from the time domain impulse response and analyze the parameters in time domain.

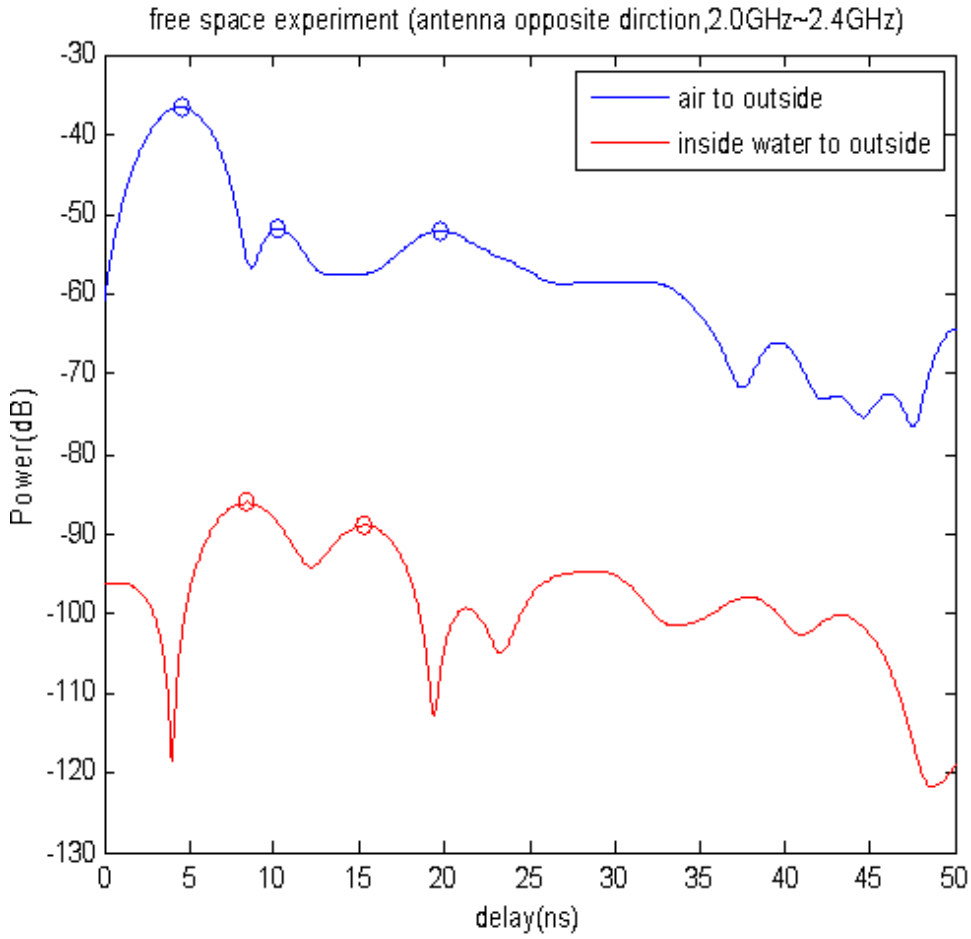

Figure 2.15: free space experiment (antenna opposite direction, 2.0GHz 2.4GHz)

Two antenna pairs are used during the measurement campaign. The transmitter antenna is fixed on the front surface of the human subject or a phantom, as point shown in figure. The distance between the human body and the antenna is about 10mm, which is caused by the clothes in between. For comparison purpose, we also insert cloths between the phantom and the antenna to make the distance in between 10mm. The antennas used here are model SMT-3TO10M-A UWB patch antennas from SkyCross corporation. The operating frequency range of these antennas is between 3.1 and 10.0GHz. The antennas and the VNA are connected by shielded coaxial cables. To eliminate the power loss from the connection part of the coaxial cables, we use the tin foil as a better shielding to

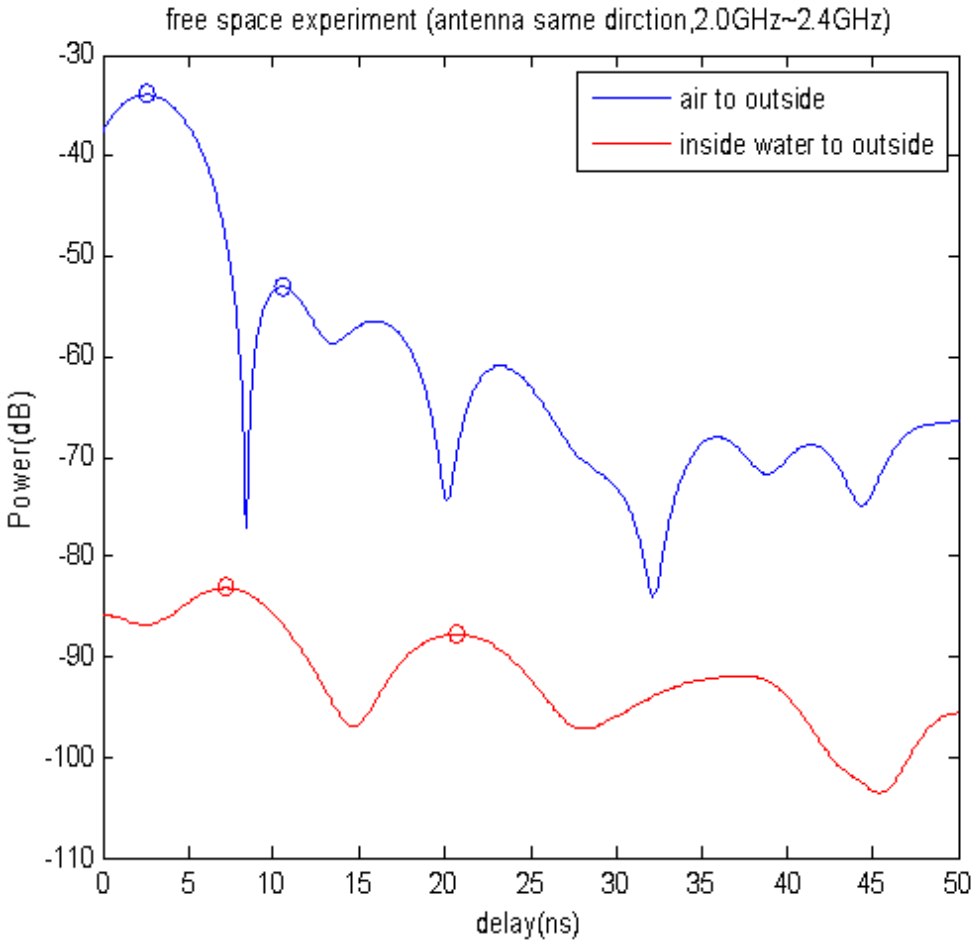

Figure 2.16: free space experiment (antenna same direction 2.0GHz 2.4GHz)

cover the cables and the connection part between the antenna and the VNA.

Figure shows the measurement setup around the phantom. The phantom we used in the measurement is from the Phantom Laboratories. The surface of the phantom is made of cellulose acetate butyrate. During the measurement, the phantom is filled with water in order to simulate the simplified environment of human body because the main component of human tissue is water and the electrical characteristics of human tissue is close to water. We conducted 20 measurements at each receiver location at each height to study the statistics of MPC parameters. The total length from the shoulder to the waist

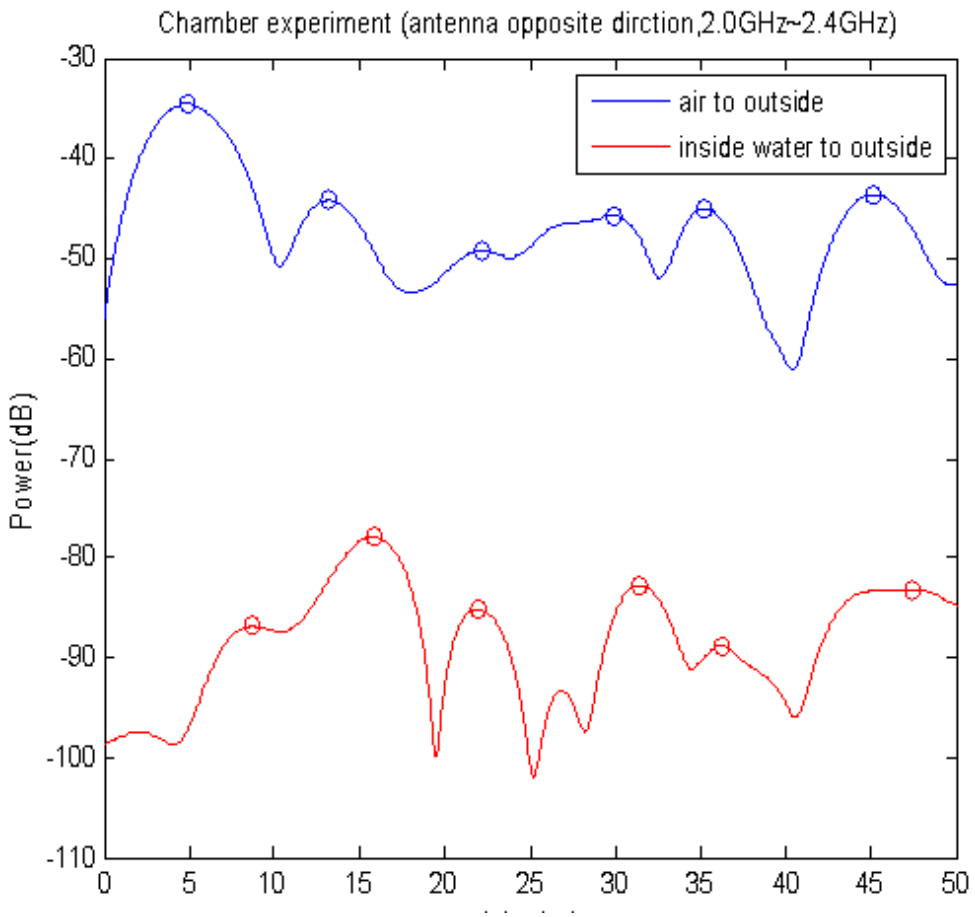

Figure 2.17: chamber experiment(antenna opposite direction, 2.0GHz 2.4GHz)

of this phantom is 45cm, hence we did the measurements every 15cm which are shown in the Figure as Height A, Height B and Height C. The distance between every two adjacent points is the same. We also did the similar measurements around the human body, shown in Figure. During these human body measurements, the person is in a standing position in the chamber and tries to keep stationary during the process of data collection.

For the RF localization applications around the human body, we develop angle based channel models for TOA and the gain of the first path for TOA ranging, and total path-

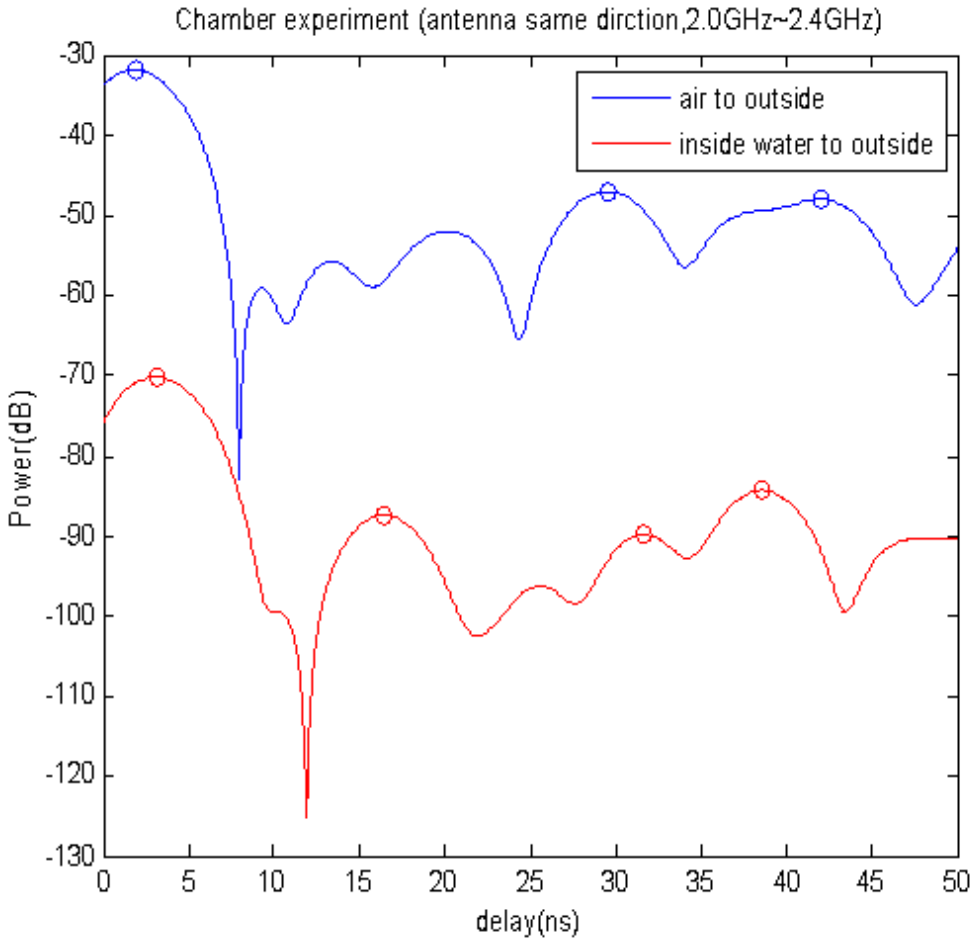

Figure 2.18: Chamber experiment(antenna same direction, 2.0GHz 2.4GHz)

loss for RSS based localization.

Generally speaking, there are three kinds of paths for RF signals traveling from the transmitter antenna to the receiver antenna in the BAN scenario. The direct path (DP), through which the signal traveling through the water in the phantom or the human tissue in real body to reach the receiver antenna. This kind of path is not the dominant path in BAN scenario because of the huge amount of gain reduction through water or the body tissue. These paths tend to be neglected in practice because they are too weak to be differentiated from the background noise [28]. The frequency range in this measurement

(a) (b)

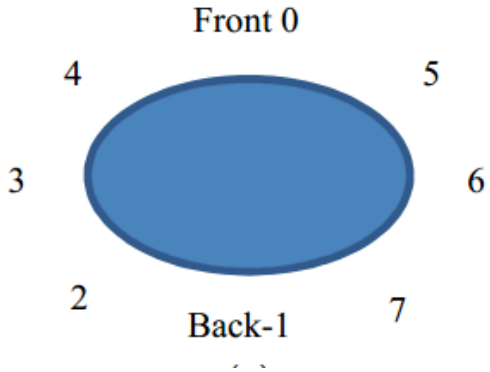

(c)

Figure 2.19: Measurement environment (a) Measurement around the phantom (b) Measurement around the human body (c) Location of measurement points at every height

campaign is 3-10GHz in which the diffracted paths are much stronger. SO we are interested in the second kind of path diffracted around the human body or a phantom which is also called the 'creeping wave'. We will focus our discussion on these paths due to their rich existences in the BAN scenario. The third kind of paths are the reflected paths from the environment which can also be neglected because we did all the measurements in the anechoic chamber and the reflected paths are absorbed by the UWB absorbers

VNA setup parameters	Value
Frequency band	3-10GHz
Number of points	1601
Transmission power	0dBm

Table 2.1: Measurement parameters

installed in the chamber.

TOA is an import ranging metric for BAN localization [6] because its high resolution provided by the high bandwidth of UWB. In the case the human body is blocked in between of the transmitter and the receiver, the TOA of the first peak of the creeping wave can be directly converted to the distance information as the input to the localization estimation algorithms.

Firstly, we measure the TOA in free space as a reference distance between the two antennas to find out the system bias. Measurement in the chamber if close to the results in free space. In this case, the only peak which can be found is the peak of the direct path. In our case, the actual distance between the transmitter and the receiver is 23.5cm. By analyzing the result, we can find the measured distance by the VNA is 31cm. In this way, the system bias Δt is 0.25ns.

During this part of the measurements, the phantom is filled with water, which can be treated as homogeneous tissue. Because of the differences in the distance from point 0 to the same point in different height, we decide to use angle instead of distance as the reference. Table shows the angle from the transmitter antenna to receiver antenna. We have three groups of data obtained in different heights at the same angle, so we calculate

P_0 to	P_1	P_2	P_3	P_4	P_5	P_6	P_7
Angle(degree)	180	132	90	48	312	270	228

Table 2.2: Angle from P_0 to P_n

the arithmetic square root of the times of arrival of the first peak of the creeping waves. In this way, we can compare the measured TOA with the expected TOA using the angle based model.

The expected TOA of the first peak can be treated as transmissions time around the surface of human body or a phantom which can be calculated using the distance-based model. In, D_{on} means the distance from transmitter antenna to the receiver antenna, c means the transmission speed of signal via air and Δt means the system bias, which has been measured in free space. In our measurement, we calculate the expected TOA of the first peak using the angle based model, as shown in 2.4.

$$Expected(TOA) = \frac{D_{on}}{c} + \Delta t = \begin{cases} \frac{1}{2} \times \frac{\theta \times \pi}{180} + \Delta t; 0 < \theta < 180 \\ -\frac{1}{2} \times \frac{(\theta - 360) \times \pi}{180} + \Delta t; 0 < \theta < 180 \end{cases} \tag{2.4}$$

In Figure 2.20 , the measured TOA and the expected TOA are shown from which we notice that the measured TOA and the expected TOA are very close. The first peak of the creeping waves in different points in various height is always the strongest peak in our measurements.

Figure **?? ??**shows the TOA of the first peak around human body. The main path we are interested in is the creeping waves, which may be influenced by the environment of the surface. The expected TOA of each angle is also used the angle based model.

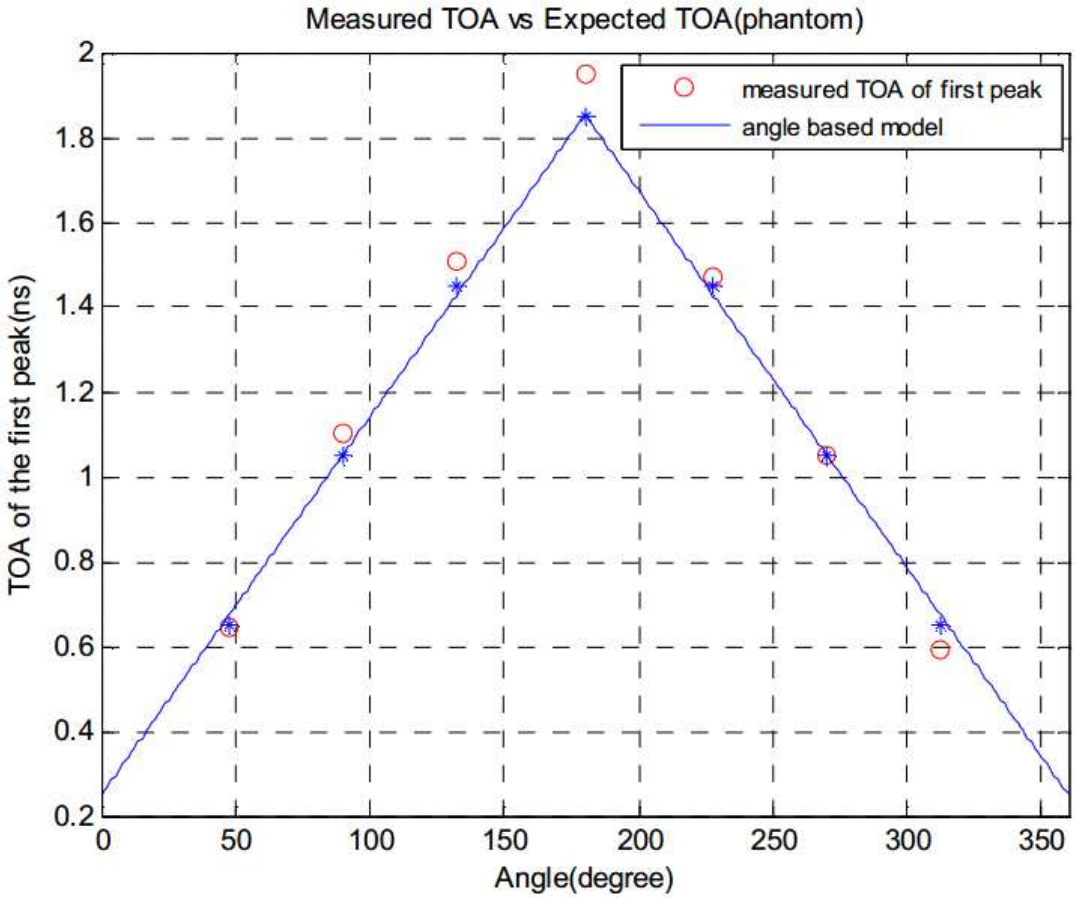

Figure 2.20: Measured TOA and expected TOA around a phantom

From the measurement results, we find that the TOA error of the human body is larger than that of the phantom which is also in accordance with our experience.

Since the DME is a very important parameter in the TOA based localization techniques, we calculate and plot the DME to figure out its distribution around the human body and the phantom. The definition of DME is in [67]

$$\varepsilon = \hat{d} - d \tag{2.5}$$

in 2.5, $\hat{d}$ means the measured distance between the transmitter antenna and the

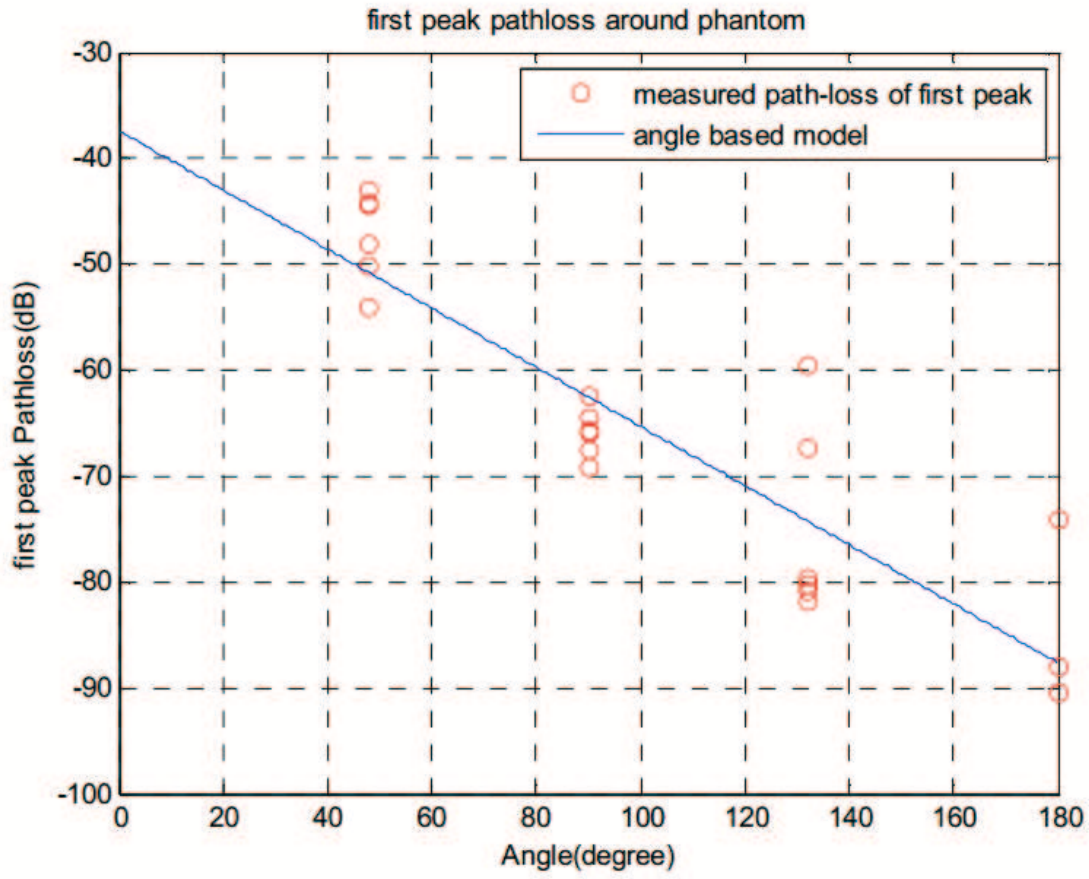

Figure 2.21: Path-loss of the first peak around the phantom

receiver antenna, and d means the expected distance between the transmitter antenna and the receiver antenna. The best achievable accuracy of a distance estimate $\hat{d}$ from TOA satisfies the following inequality

$$\sqrt{Var(\hat{d})} \geq \frac{c}{2\sqrt{2}\pi\sqrt{SNR}\beta} \qquad \beta = [\int_{-\infty}^{\infty} f^2|s(f)|^2df / \int_{-\infty}^{\infty} |s(f)|^2df]^{1/2} \tag{2.6}$$

in 2.6,c is the speed of light, SNR is the signal to noise ratio for the used signal and β is the effective signal bandwidth. Since the receiver power of the first peak of the creeping wave is between -45dBm and -90dBm and the noise floor is around -120dBm,

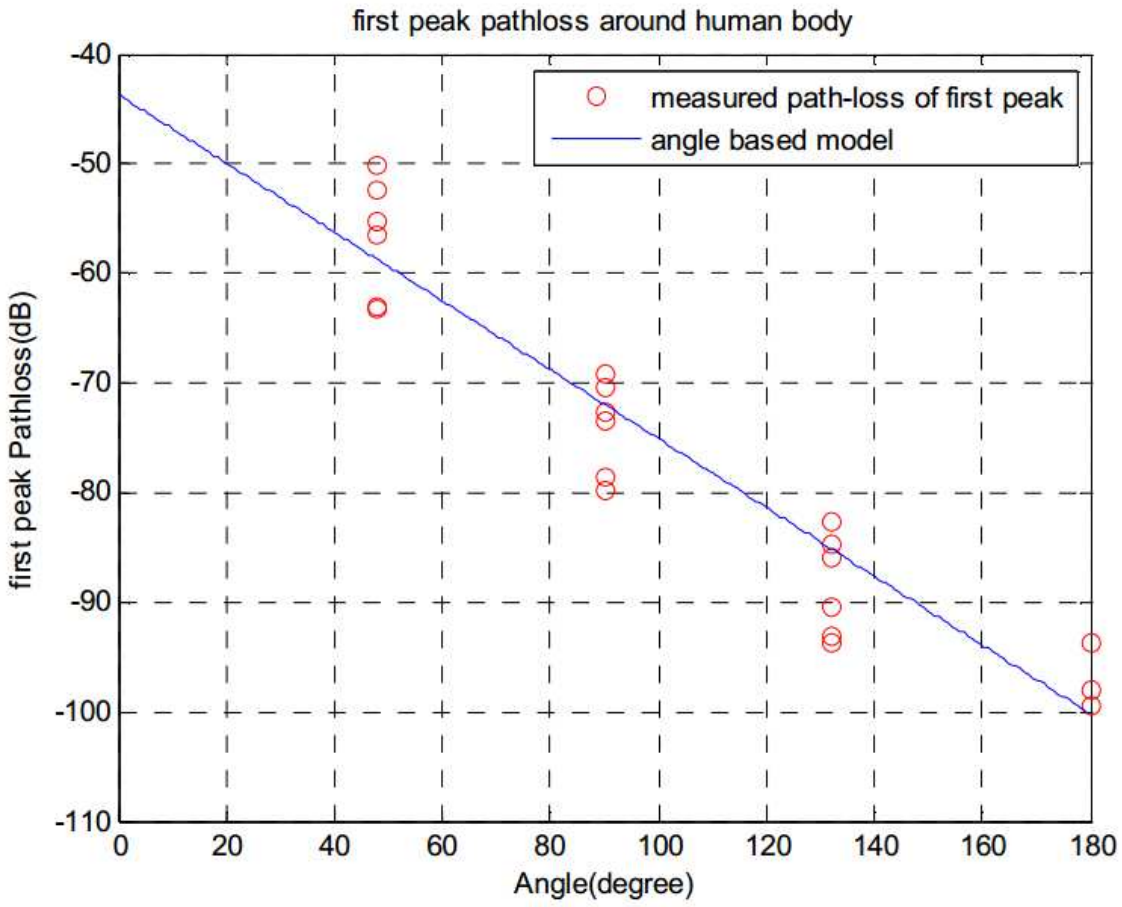

Figure 2.22: Path-loss of the first peak around the human body

therefore the SNR value here between 75dB to 30dB and the effective bandwidth β equals to 7GHz. Based on 2.6, the standard deviation of the distance estimation is less than 0.11cm, which is much smaller than the minimum measured standard deviation, 2.32cm.

From Table 2.3, we see that the mean of DME around the phantom is close to 0 and the distribution of the DME around the phantom follows the Gaussian distribution which is shown in Figure 2.25. The mean of DME around the human body is 12.06cm which can be treated as the bias. After eliminating this bias, the CDF of DME around the

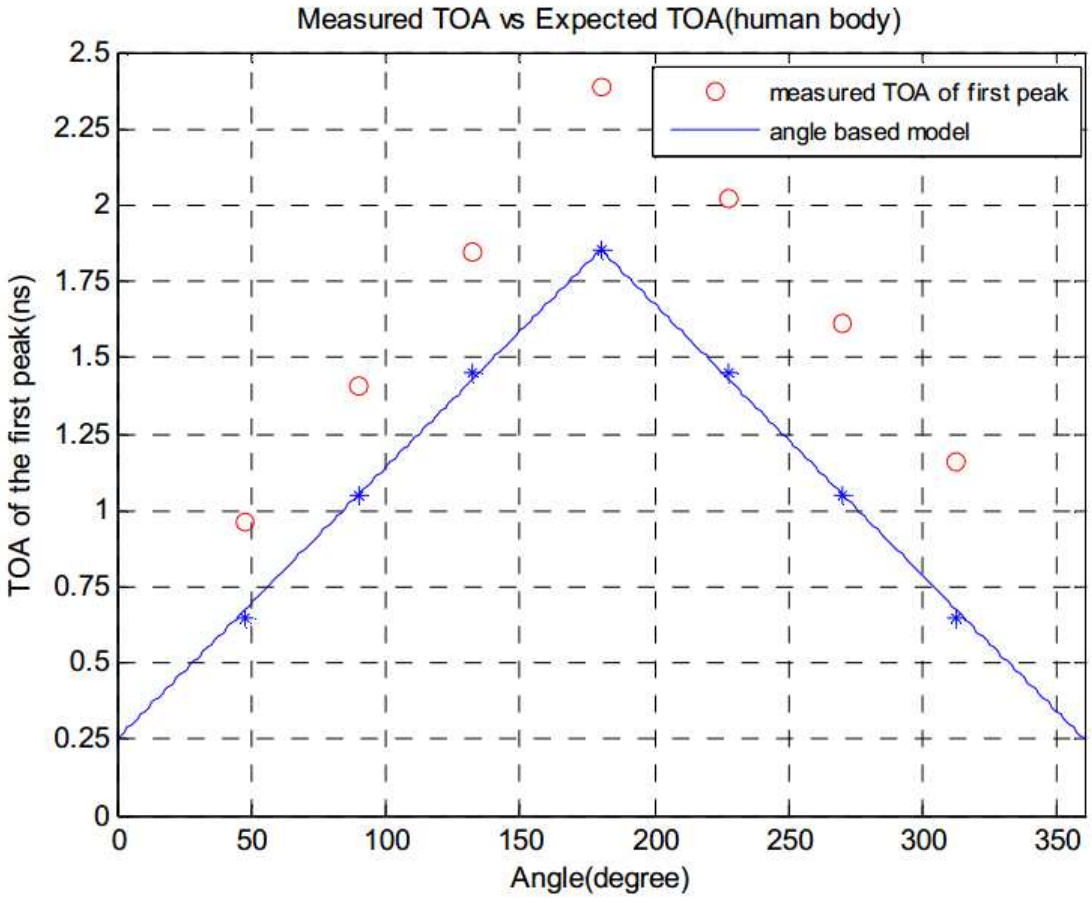

Figure 2.23: Measured TOA and expected TOA around the human body

human body also follows the Gaussian distribution. The measurement results suggest that the creeping wave is a very useful metric for RF localization in BAN.

RSS of the first peak is an important metric in RF localization. However, only using RSS of the first peak to estimate the location might cause significant error in the estimation results.However, if the first peak can be captured accurately, we can estimate the location of the transmitter antenna with the help of TOA.

In our measurement, the selected points around the human body and a phantom are symmetrical. In this way, we only use one side of the data when analyzing the RSS.

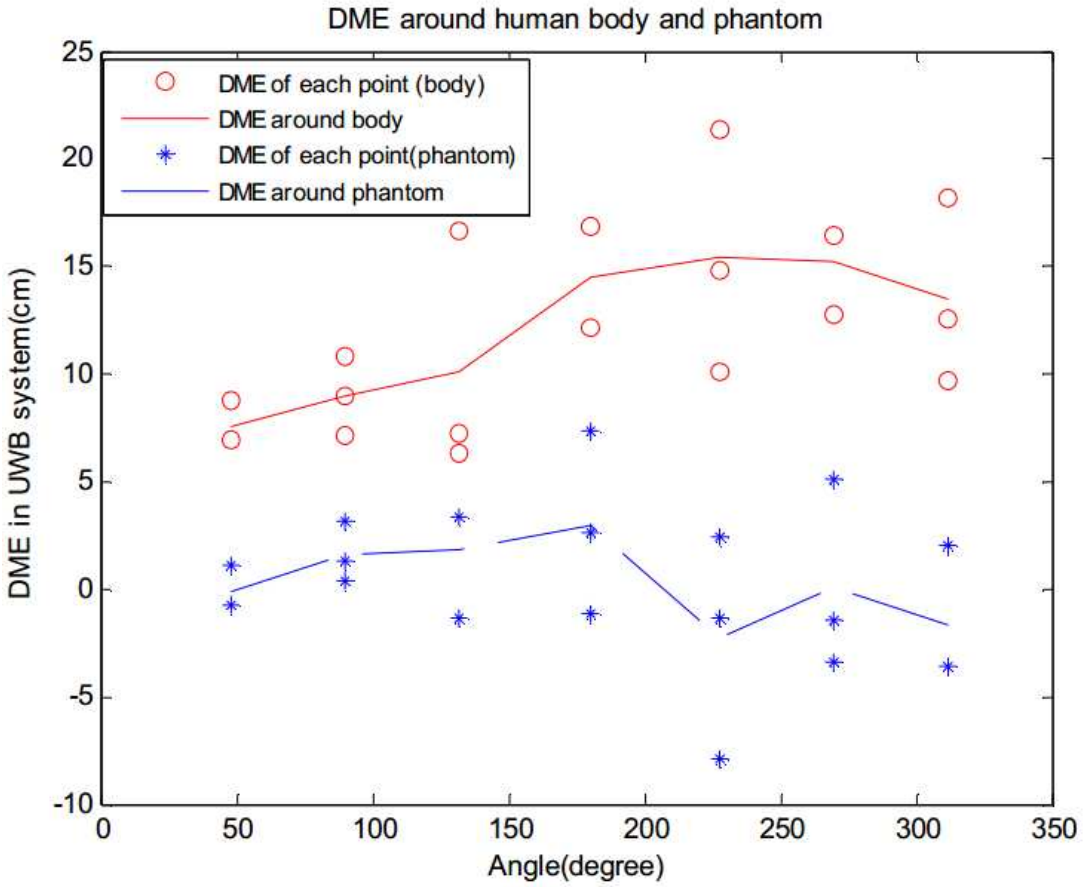

Figure 2.24: DME around human body and a phantom

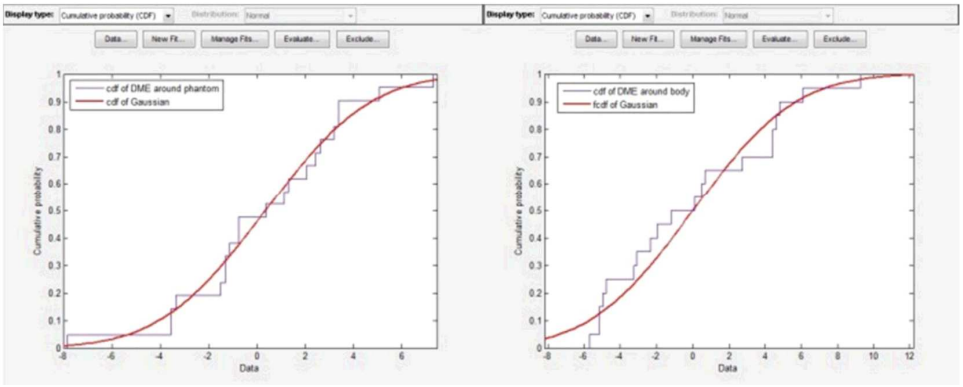

Figure 2.25: (a) CDF of Gaussian and CDF of DME around a phantom; (b)CDF of Gaussian and CDF of DME around the human body

	DME	
	Mean	Std.
Phantom	0.34	3.44
Human body	12.06	4.46

Table 2.3: Mean and standard deviation of DME around a phantom and human body

	Phantom	Human
$P_{dB}(\theta_0)$	$41.25dB$	$48dB$
γ_1	$16dB/rad$	$18dB/rad$
θ_0	$0.2415rad$	$0.2415rad$

Table 2.4: Parameters of angle based channel model for the first peak path-loss

Based on the measurement results, we build an angle based channel model for the path-loss of the first peak as follows:

$$P_{f-dB}(\theta) = P_{dB}(\theta_0) - \gamma_1(\theta - \theta_0) \tag{2.7}$$

Figure and Figure show the measured path-loss and angle based channel model we built of the first peak path loss around a phantom and the human body.

$$P_{dB} = P_0 + 10nlog(d) \tag{2.8}$$

Based on our measured results, we calculate the path loss gradient n based on 2.8. After fitting the measurement results, we get the path-loss gradient n of the first-peak around a phantom and human body equal to 5.8 and 7.27. The path-loss gradient n of total path-loss around a phantom and human body equal to 4.47 and 6. The first path-

	Path loss gradient n	
	Phantom	Human body
First-peak	5.8	7.27
Total path-loss	4.47	6

Table 2.5: Path-loss gradient n in different situations

	Phantom	Human
$P_{dB}(\theta_0)$	$36.25dB$	$44.25dB$
γ_1	$13dB/rad$	$16dB/rad$
θ_0	$0.3115rad$	$0.3115rad$

Table 2.6: Parameters of angle based channel model for the total path-loss

loss gradient is larger than that of the total path-loss. The result is reasonable. All these results about the path-loss gradient are listed in Table 2.5

Channel models for wireless communications around the human body at the radio frequency of 400MHz, 900MHz and 2.4GHz have been built in [73], [61], [20], however, there is no angle based channel model for UWB band. According to our measurement results, we build an angle based channel model for RF localization around human body in UWB as in 2.9. The parameters for this model are shown in Table 2.6

Figure shows the measured total path-loss, the distance based total path-loss around a phantom and the human body.

$$P_{dB}(\theta) = P_{dB}(\theta) - \gamma_1(\theta - \theta_0) \tag{2.9}$$

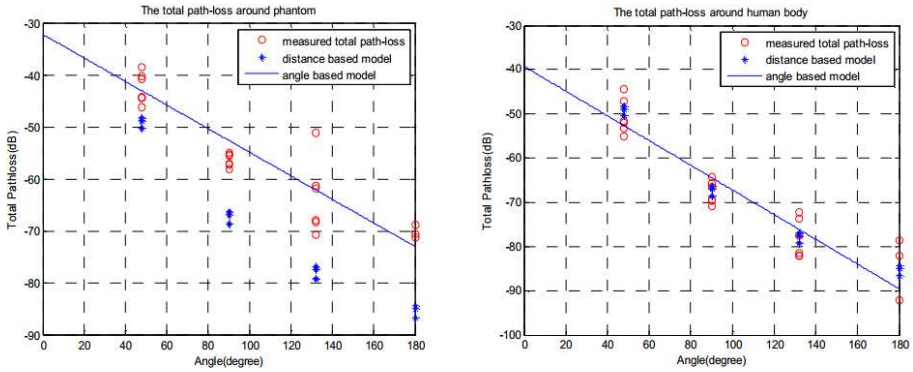

Figure 2.26: Measured total path-loss, distance based and angle based total path-loss around a phantom and human body

Chapter 3

RSS Path Loss Model for Received Signal Strength(RSS) based VCE Localization

To calculate the CRLB, we define a performance evaluation scenario and models for the behavior of the localization metrics [7], the RSS and TOA, for RF signaling in between the GI tract and the body-mounted sensors used for localization. In this section we introduce a general scenario for comparative performance evaluation of RSS- and TOA-based localization for capsule endoscopy application. The scenario is designed to reflect the performance in different organs, the path of movement of the VCE inside the small intestine, and the number and pattern of installation of body mounted sensors on the torso. Since the received signal on the body-mounted sensors is distorted with the multipath receptions caused by the refraction at the boundary of organs and tissues inside the human body [92], models for behavior of the RSS and TOA are fairly complicated. These models are then introduced in the rest of the section.

3.1 Performance evaluation scenario

The major organs in the GI tract are the esophagus, stomach, small intestine, and large intestine shown in Figure 3.2(a).

Figure 3.2(a) shows the relative location and shape of the three major organs in the GI tract, stomach, small intestine, and colon or large intestine. In order to emulate a scenario for comparative performance evaluation of RSS- and TOA-based localization

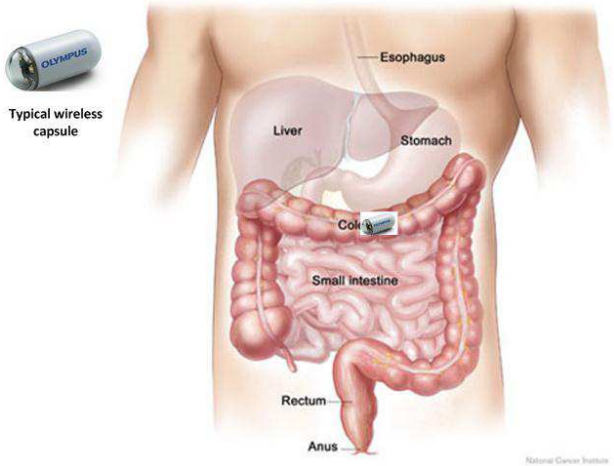

(a)

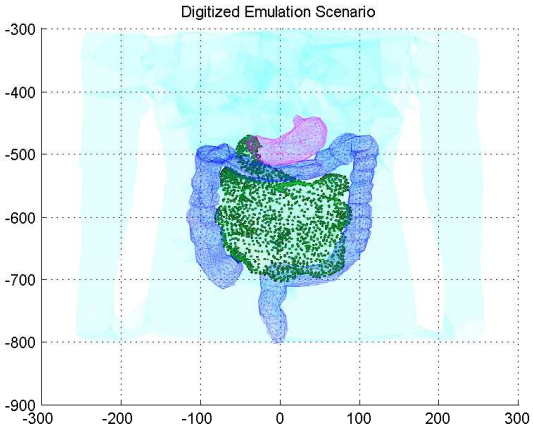

(b)

Figure 3.1: Anatomy of GI tract (a) A schematic of the GI tract. (b) The digitized major organs in the GI tract

systems we first analyses the effects of the shape of the organs by comparing the localization performance in the three major organs. Then, we focus on the analysis of the performance as the VCE moves along the small intestine. To create the environment, we use a three-dimensional (3D) human model from the full-wave electromagnetic field simulation system (Ansoft [2]). This 3D human body model has a spatial resolution of 2 millimeters and includes frequency dependent dielectric properties of more than 300 parts in a male human body. Figure 3.2(b). shows the digitized picture of the three major organs in this human body model. For comparative performance evaluation in different organs, we calculate the CRLB for each grid point of an organ and we compare the CDF or these errors for different topologies of the body mounted sensors. Since small intestine is a long curled organ, the VCE takes a path to go through this organ. Given the 3D CAD model of the small intestine, we found the path of the movement of the capsule and imported this path into the software simulation tool for RF propagation modeling. Given a 3D model of the intestinal tract, shown in Fig.3.2(b) ,

we applied 3D image processing [77] techniques to trace the path of movements inside the intestine. In the case of the large intestine, since it already has a very clear pattern, which looks like a big hook, applied 3D skeletonization technique [**?**] to extract the path. Since the shape of the small intestine is much more complicated, the same technique does not work well. In this case, we developed an element sliding technique [**?**] to trace the path. The basic idea behind this technique is to define an element shape with its radius automatically adjustable to the radius of the small intestine. As the element shape goes along the small intestine, the center of the element shape is recorded to define a clear path movement inside the small intestine. The result of the path extracted for large and small intestines from the 3D model is shown in Figure.**??**. For comparative performance evaluation, we determine the CRLB along the path of capsule in the small

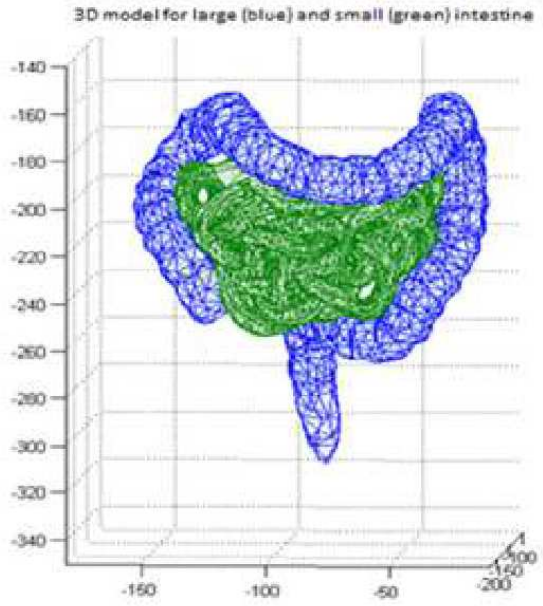

(a)

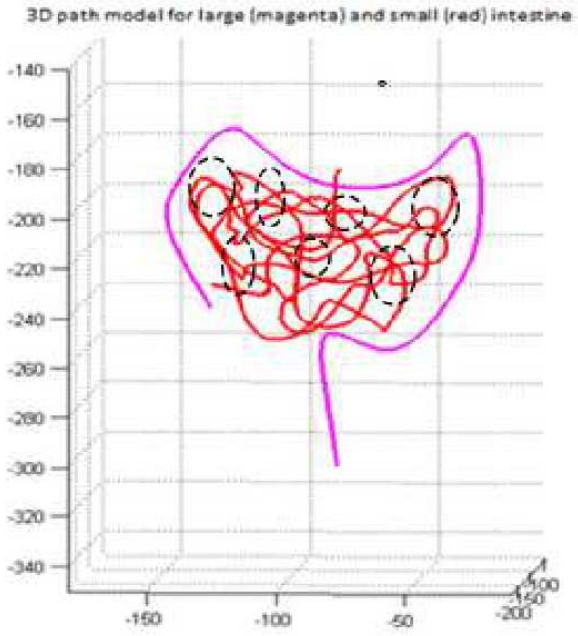

(b)

Figure 3.2: (a)3D model for large and small intestine (b)3D path model for large and small intestine

intestine for different topologies of body-mounted sensors.

To define the topologies of the body-mounted receiver sensors, similar to [30], we assume the receiver arrays are placed on a jacket worn by the patient during the examination. We calculated the CRLB for 8, 16, 32 and 64 body-mounted receiver sensors spread over a rectangular area with a three dimensional range of $268 \times 323 \times 312$ millimeters. Sensor receivers are mounted in grids in equal number in front and on the back of the jacket. An example of a typical network topology for 32 receiver sensors is illustrated in Figure 3.3. Using the path loss models as well as the path of movement inside the small intestine for the RSS and the ranging error model for TOA estimations, we determine the CRLB for each of the three major organs as well as path of movement inside the small intestine for different body mounted sensor topologies.

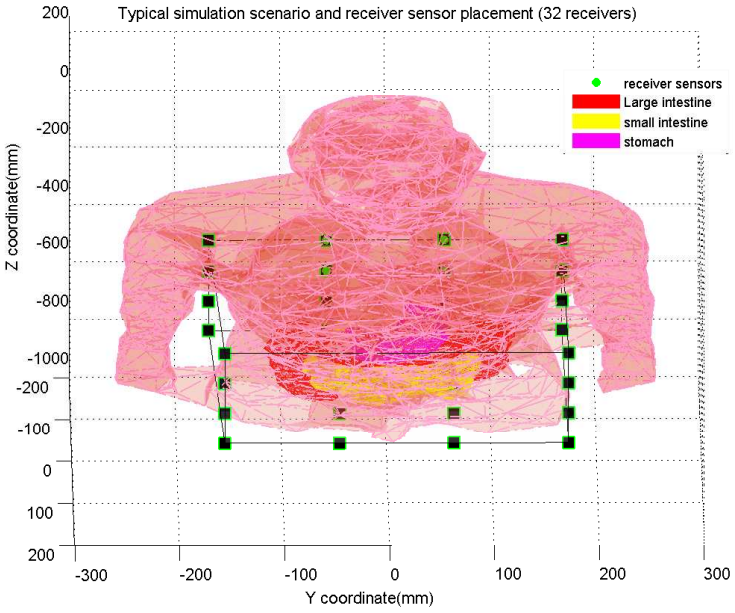

Figure 3.3: A typical 3D pattern of body mounted sensors used as reference points of the performance evaluation scenario for localization of the VCE .

3.2 Path loss model for the channels between the VCE and the body mounted sensors

Calculation of the CRLB for performance evaluation of the RSS-based localization need a path-loss model for the RF propagation from the inside of the GI tract, where the VCE travels, to the body mounted sensors used as reference points for localization. The path-loss model we used for the performance evaluation of RSS-based VCE localization inside the human body is the one reported in [76]. The model was developed by National Institute of Standards and Technology (NIST) at $402 - 405MHz$ MICS band using a fully digitized human body with detailed organs and tissues and a 3D full-wave electromagnetic field simulator [76].

This model relates the $L_p(d)$, the path loss in dB between the VCE and the body-mounted sensors at distance d by the following equation:

$$L_p(d) = L_p(d_0) + 10\alpha \log_{10}(d/d_0) + S \tag{3.1}$$

where d_0 is the reference distance set at 50mm, $L_p(d_0)$is the path loss at the reference distance, α is the path loss gradient and S is a zero mean log-normally distributed random variable representing the shadow fading effect caused by different human tissues.

The model is developed for the near-surface implants applications with distances less than 10 cm inside the human body from the surface skin as well as deep-tissue implants applications with distances more than 10 cm.

The parameters associated with the two scenarios for the implant to body surface path loss model are summarized in table 3.1. In this table, σ_{dB} is the standard deviation of shadow fading S. In our simulations, 10 cm distance between the VCE and body

mounted receiver sensors is used as the threshold for choosing between the two models.

Table 3.1: Parameters for the statistical implant to body surface path loss model.

Implant to Body Surface	$L_p(d_0)$(dB)	α	σ_{dB}
Deep Tissue	47.14	4.26	7.85
Near Surface	49.81	4.22	6.81

Chapter 4

Time of Arrival (TOA) Ranging Error Model for TOA based VCE Localization

Traditional localization systems such as GPS [15]use the more accurate TOA localization approach. To determine the distance between a terminal and a reference point, the TOA of signal is measured to determine the flight time of the radio wave [5] [9]. The distance is calculated by multiplying the time of flight of the signal with the speed of radio propagation in the medium, which is the same as the speed of light for those applications [51].

In traditional indoor scenario TOA based localization, the biggest challenge is the appearance of the so called "undetected direct path problem" [41] [1], for TOA based localization of the VCE, the most challenging problem comes from the complexity of the environment where the capsule travels through. Various organs and tissues with different permittivity make it difficult to predict the propagation speed of RF signal traveling through the human body. Since we do not know the speed of the propagation inside the human body, to calculate the distance, we may use the average speed of propagation in different organs [49]. This approach causes ranging error caused by deviations of the actual speed of propagation in different organs from the average speed. This error is much higher than the traditional TOA-based ranging error caused by the bandwidth and power limitations [8],and it dominates the TOA-based localization error [80], [59]. Therefore, we need a TOA ranging error model to account for this error source in TOA ranging process.

4.1 TOA ranging error models for channels between the VCE and the body mounted sensors

n this part, we will summarize our work in modeling of the TOA ranging error caused by lack of information of the real propagation velocity inside the human body. The current TOA ranging method calculates the distance by multiplying the TOA with the velocity derived from the average permittivity of the human body [49]. This approach results a ranging error caused by inhomogeneity of body as a medium for radio propagation. We propose a 3D simulation platform to address this issue in details. In RF localization literature [4, 65], the ranging error is defined as:

$$DME = d - \hat{d} \tag{4.1}$$

where d is the actual distance and $\hat{d}$ is the estimated distance. Considering the total distance traveled through the body is added by the distance in each organ or tissue, the total distance can be expressed as

$$d_{total} = d_1 + d_2 + \cdots + d_n \tag{4.2}$$

where d_1 to d_n are the distances traveled in each organ or tissue. In reality, we use the average permittivity of human body to estimate the average propagation velocity inside human body, which is

$$\bar{v} = \frac{c}{\sqrt{\bar{\epsilon_r}}}. \tag{4.3}$$

Therefore, the estimated distance is expressed as

$$\begin{aligned} \hat{d} &= \hat{\tau}\bar{v} = (\hat{\tau_1} + \hat{\tau_2} + \cdots + \hat{\tau_n})\tfrac{c}{\sqrt{\bar{\epsilon_r}}} \\ &= \textstyle\sum_{i=1}^{n} \frac{d_i}{v_i}\frac{c}{\bar{\epsilon}} = (\frac{d_1}{c/\sqrt{\epsilon_1}} + \frac{d_2}{c/\sqrt{\epsilon_2}} + ... + \frac{d_n}{c/\sqrt{\epsilon_n}})\frac{c}{\bar{\epsilon}}. \end{aligned} \tag{4.4}$$

The difference between d_{total} and $\hat{d}$ is the ranging error caused by human tissue inhomogeneity that we refer to as DME in equation (3.1) [22]. This error between the actual

distance and the distance measured by TOA and average velocity of the propagation is caused by using a single velocity rather than multiple velocities. To determine the statistics of this error, we simulated the effect of inhomogeneous tissues on TOA ranging in a 3D torso environment, shown in Figure 4.1. We have selected approximately five hundred pairs of random locations on the human body torso and for each pair, we have calculated the DME using equation (4.1). The human organs' relative permittivitys are a function of the operating frequency, we studied the TOA ranging error at MICs band for the center frequency of 405MHz, which is the reserved band for implant and in body applications.

4.2 Human tissue/organ non-homogeneity

The average permittivity is calculated by weighting the permittivity of each organ according to their volume, the average permittivity is 46.35 in the torso environment. The permittivity and volume of different organs used for this simulation is shown in table 4.1 [62].

Table 4.1: Organ Parameters used for Simulation$[\epsilon_r, v(cm^3)]$.

Intestine (50.7,3936.3)	Stomach (67.8,357)	Gallbladder (52.3,12.4)
Lung(23.77,4320)	Heart(65.97,625.4)	Kidney(68,325.1)
Spleen(63.1,160.2)	Liver(51.15,1357)	Muscle(47.8,32403.4)

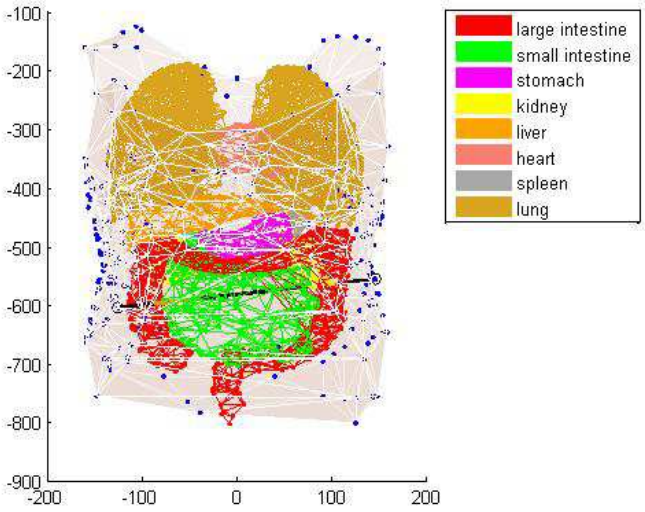

(a) Stomach

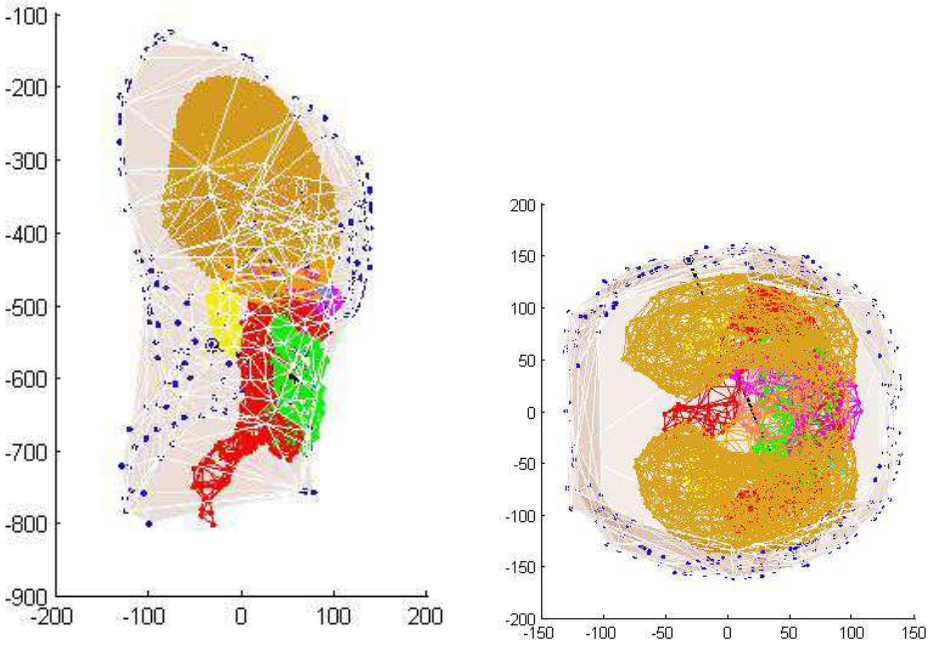

(b) Small Intestine (c) Large Intestine

Figure 4.1: Simulation scenario for the DME in TOA ranging. The transmitter and receiver pairs are randomly distributed on the surface of body torso. The path length through each organ are marked as different colors in order to calculate the DME caused by tissue inhomogeity.

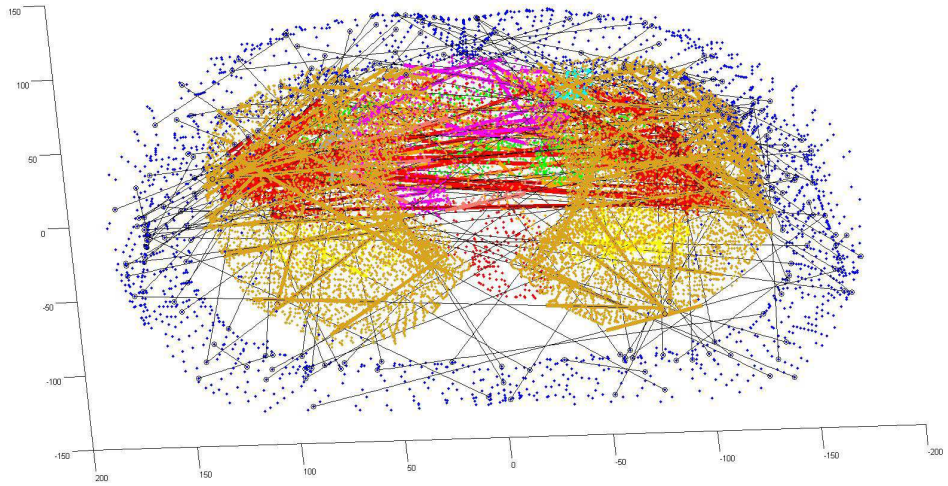

Figure 4.2: Simulation scenario for the DME in TOA ranging.

4.3 Conclusions

Figure 4.3 presents the results of simulation and the best fit Gaussian distribution to the results. The mean value of DME is -3.92 mm, while the standard deviation of DME $\sigma_T$is 24.3 mm. The mean value of DME is a negative value because the largest organ in the torso cavity is the lungs, which have a much smaller permittivity value than the average permittivity of human tissues. Hence, the signal propagates faster in the lungs than the average speed of signal propagation inside human body. When we use the average propagation to calculate the estimated distance, the value is smaller than the real distance, because we underestimated the distance signal went through the lungs.

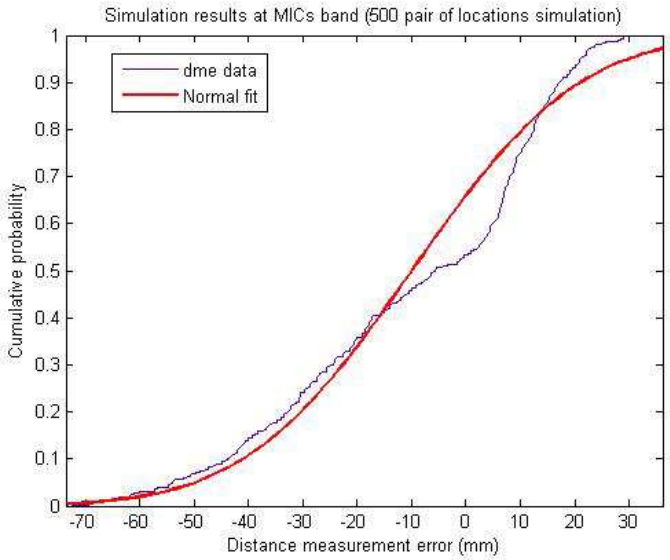

Figure 4.3: CDF of DME caused by human tissue inhomogeneity.

Chapter 5

Cramer-Rau Lower Bound (CRLB) for VCE Cooperative Localization

In this chapter, based on the performance evaluation scenario, path loss and TOA ranging error models in section 3,4. We derive a universal 3D CRLB for cooperative localization of the VCE inside the GI tract. We begin by developing performance bounds for RSS-and TOA-based localization for one capsule traveling inside the GI tract the for different patterns of body-mounted array of sensors. We then extend our analysis to cooperative localization using multiple capsules. In the cooperative localization [95], a patient takes more than one capsule in different times and localization is based on the measured RSS and TOA among the capsules as well as the pattern of body-mounted sensors. We determine the CRLB accuracy of localization for different scenarios involving different numbers of capsules and body-mounted sensor arrays in the major organs in the human GI tract.The performance of RSS-based localization depends on variations of the transmitted power [33]and that power is affected by the variations in the behavior of the batteries. In the latter part of this section, we provide a performance evaluation methodology for analysis of the effects of these variation on the performance of the RSS-based localization techniques.

5.1 CRLB for single VCE localization

Consider the VCE whose location is being estimated is indexed 1, and m body mounted receiver sensors denoted with indexes $2...m+1$. Each receiver sensor i is capable of measuring the TOA t_i or RSS r_i from the VCE. The observation vector is $X = [t_2, ...t_{m+1}]$ for the TOA case or $X = [r_2, ...r_{m+1}]$ for the RSS case. Assume he location coordinate of the VCE is $\theta_1 = [x_1, y_1, z_1]$, then our objective here is to estimate the location of the VCE $\hat{\theta_1}$. The t_i observations are modeled as normal random variables $f_{t_i/\theta_1,\theta_i} \sim N(d_{i,1}/\bar{v}, \sigma_T^2)$, where $d_{i,1}$ is the distance between the VCE and receiver sensor i. $\bar{v}$ is the average propagation speed of RF signal inside the human GI tract, and σ_T is the parameter describing the TOA ranging error caused by human tissue non-homogeneity. The r_i measurements are log-normally distributed $f_{r_i}dB/_{\theta_1,\theta_i} \sim N(P_r(dB), \sigma_{sh}^2)$, with $P_r(dB) = P_0(dB) - 10\alpha \log 10(d_{1,i})$. $P_0(dB)$ is the RSS at the reference distance (i.e. 50mm) from the VCE. α is the path loss gradient and σ_{sh} is the variance of the log normal shadowing.

The CRLB of $\hat{\theta}_1$ is $cov(\hat{\theta}_1) \geq I(\theta_1)^{-1}$ where $I(\theta_1)$ is the Fisher information matrix (FIM)

$$\begin{aligned} I_{\theta_1} &= -E\nabla_{\theta_1}(\nabla_{\theta_1} \ln l(X|\theta_1, \theta)) \\ &= \begin{bmatrix} I_{xx} & I_{xy} & I_{xz} \\ I_{xy} & I_{yy} & I_{yz} \\ I_{xz} & I_{yz} & I_{zz} \end{bmatrix} (3D \quad situation) \end{aligned} \tag{5.1}$$

where $l(X|\theta_1, \theta)$ is the logarithm of the joint conditional probability density func-

tion:

$$\begin{aligned} l(X|\theta_1,\theta) &= \textstyle\sum_{i=2}^{m+1} \log f_{t_i|\theta_1,\theta_i}(for \quad TOA) \\ l(X|\theta_1,\theta) &= \textstyle\sum_{i=2}^{m+1} \log f_{r_i|\theta_1,\theta_i}(for \quad RSS) \end{aligned} \tag{5.2}$$

and

$$\begin{aligned} I_{xx} &= -\textstyle\sum_{i=2}^{m+1} E[\frac{\partial^2 \log f_{t_i|\theta_1,\theta_i}}{\partial^2 x_1^2}](for \quad TOA) \\ I_{xx} &= -\textstyle\sum_{i=2}^{m+1} E[\frac{\partial^2 \log f_{r_i|\theta_1,\theta_i}}{\partial^2 x_1^2}](for \quad RSS) \end{aligned} \tag{5.3}$$

Similar definitions can be extend to $I_{yy}, I_{zz}, I_{xy}, I_{xz}$ and I_{yz}. The CRLB on the variance of the TOA/RSS location estimation is

$$\begin{aligned} &\sigma_1^2 = tr\left\{cov_\theta(\hat{x}_1, \hat{y}_1, \hat{z}_1)\right\} \\ &= Var_\theta(\hat{x}_1) + Var_\theta(\hat{y}_1) + Var_\theta(\hat{z}_1) \\ &= \min tr(cov(\hat{\theta_1})) = tr(I(\theta_1)^{-1}) \\ &= (-I_{xx}(I_{yy} + Izz) + I_{xy}I_{xy} + I_{xz}I_{xz} - I_{yy}I_{zz} + \cdots \\ &I_{yz}I_{yz})/(-I_{xx}I_{yy}I_{zz} + I_{xx}I_{yz}I_{yz} + \cdots \\ &I_{xy}I_{xy}I_{zz} - I_{xy}I_{yz}I_{xz} - I_{xz}I_{xy}I_{xx}I_{yz} + I_{xz}I_{yy}I_{xz}) \end{aligned} \tag{5.4}$$

The derivations of the likelihood function for the TOA and RSS case was originally derived in [70] [71] for 2D case. Here, we extended the work to 3D scenario for VCE applications. The details are given in the appendix.

5.2 CRLB for multiple VCEs cooperative localization

The localization problem is formulated as follows, N wireless endoscopic capsules are distributed in the GI tract with locations given by $\theta_c = [p_1, \cdots, p_N]$. These pills are

blindfolded devices but they can measure the RSS from each other and transmit the information out to the receiver array for further processing. M receiver sensors are placed on the surface of the human body with location given by $\theta_r = [p_{N+1}, \cdots, p_{N+M}]$. The vector of device parameters is $\theta = [\, \theta_c \;\; \theta_r \,]$. For this three dimensional system, $p_i = [x_i, y_i, z_i]^T$, where $i \in [1, N+M]$ and T is the transpose operation. The unknown parameters to be estimated can be represented by a $3 \times N$ coordinates matrix. t_i or RSS r_i from the VCE. The observation vector is $X = [t_2, ...t_{m+1}]$ for the TOA case or $X = [r_2, ...r_{m+1}]$ for the RSS case. Assume he location coordinate of the VCE is $\theta_1 = [x_1, y_1, z_1]$, then our objective here is to estimate the location of the VCE $\hat{\theta_1}$. The t_i observations are modeled as normal random variables $f_{t_i/\theta_1,\theta_i} \sim N(d_{i,1}/\bar{v}, \sigma_T^2)$, where $d_{i,1}$ is the distance between the VCE and receiver sensor i. $\bar{v}$ is the average propagation speed of RF signal inside the human GI tract, and σ_T is the parameter describing the TOA ranging error caused by human tissue non-homogeneity. The r_i measurements are log-normally distributed $f_{r_i}dB/_{\theta_1,\theta_i} \sim N(P_r(dB), \sigma_{sh}^2)$, with $P_r(dB) = P_0(dB) - 10\alpha \log 10(d_{1,i})$. $P_0(dB)$ is the RSS at the reference distance (i.e. 50mm) from the VCE. α is the path loss gradient and σ_{sh} is the variance of the log normal shadowing.

The CRLB of $\hat{\theta_1}$ is $cov(\hat{\theta_1}) \geq I(\theta_1)^{-1}$ where $I(\theta_1)$ is the Fisher information matrix (FIM)

$$
\begin{aligned}
I_{\theta_1} &= -E\nabla_{\theta_1}(\nabla_{\theta_1} \ln l(X|\theta_1, \theta)) \\
&= \begin{bmatrix} I_{xx} & I_{xy} & I_{xz} \\ I_{xy} & I_{yy} & I_{yz} \\ I_{xz} & I_{yz} & I_{zz} \end{bmatrix} (3D \quad situation)
\end{aligned}
\tag{5.5}
$$

where $l(X|\theta_1, \theta)$ is the logarithm of the joint conditional probability density function:

$$\begin{aligned} l(X|\theta_1,\theta) &= \textstyle\sum_{i=2}^{m+1} \log f_{t_i|\theta_1,\theta_i}(for \quad TOA) \\ l(X|\theta_1,\theta) &= \textstyle\sum_{i=2}^{m+1} \log f_{r_i|\theta_1,\theta_i}(for \quad RSS) \end{aligned} \tag{5.6}$$

and

$$\begin{aligned} I_{xx} &= -\textstyle\sum_{i=2}^{m+1} E[\frac{\partial^2 \log f_{t_i|\theta_1,\theta_i}}{\partial^2 x_1^2}](for \quad TOA) \\ I_{xx} &= -\textstyle\sum_{i=2}^{m+1} E[\frac{\partial^2 \log f_{r_i|\theta_1,\theta_i}}{\partial^2 x_1^2}](for \quad RSS) \end{aligned} \tag{5.7}$$

Similar definitions can be extend to $I_{yy}, I_{zz}, I_{xy}, I_{xz}$ and I_{yz}. The CRLB on the variance of the TOA/RSS location estimation is

$$\begin{aligned} &\sigma_1^2 = tr\left\{cov_\theta(\hat{x}_1, \hat{y}_1, \hat{z}_1)\right\} \\ &= Var_\theta(\hat{x}_1) + Var_\theta(\hat{y}_1) + Var_\theta(\hat{z}_1) \\ &= \min tr(cov(\hat{\theta_1})) = tr(I(\theta_1)^{-1}) \\ &= (-I_{xx}(I_{yy} + Izz) + I_{xy}I_{xy} + I_{xz}I_{xz} - I_{yy}I_{zz} + \cdots \\ &I_{yz}I_{yz})/(-I_{xx}I_{yy}I_{zz} + I_{xx}I_{yz}I_{yz} + \cdots \\ &I_{xy}I_{xy}I_{zz} - I_{xy}I_{yz}I_{xz} - I_{xz}I_{xy}I_{xx}I_{yz} + I_{xz}I_{yy}I_{xz}) \end{aligned} \tag{5.8}$$

The derivations of the likelihood function for the TOA and RSS case was originally derived in [70] for 2D case. Here, we extended the work to 3D scenario for VCE applications. The details are given in the appendix.

$$\theta_c = [p_1, p_2, ..., p_N] = \begin{bmatrix} x_1 & x_2 & ... & x_N \\ y_1 & y_2 & ... & y_N \\ z_1 & z_2 & ... & z_N \end{bmatrix} \tag{5.9}$$

Consider devices (devices include capsules and receivers)i and j make pair-wise observations $X_{i,j}$. We assume each receiver sensor can measure the RSS from all the capsules inside the body, but the path loss parameters for different links varies as the distance between the receiver sensor and capsule inside the body changes. Therefore, Let $H(i) = \{j$:device j makes pair-wise observations with device $i\}$. $H\{i\} = \{1, \cdots, i-1, i+1, \cdots, N+M\}$ for $i \in [1, N]$ and $H\{i\} = \{1, \cdots, N\}$ for $i \in [N+1, N+M]$ because a device cannot make pairwise observation with itself and the receivers do not make observations with receivers either. Therefore the length of the observation vector X is $N \times (N + M - 1) + M \times N$.

By reciprocity,we assume $X_{i,j} = X_{j,i}$; Thus, it is sufficient to consider only the lower triangle of the observation matrix X when formulating the joint likelihood function [70]. The CRLB on the covariance matrix of any unbiased estimator $\hat{\theta}$ is given by [87]:

$$cov(\hat{\theta}) = E\left[(\hat{\theta} - \theta)(\hat{\theta} - \theta)^T\right] \geq F_\theta^{-1} \tag{5.10}$$

where $E[\cdot]$ is the expectation operation and F is the Fisher information matrix (FIM) defined as:

$$\begin{aligned} F_\theta &= -E\nabla_\theta(\nabla_\theta \ln f(X|\theta))^T \\ &= E_\theta[\tfrac{\partial}{\partial\theta} \ln f(X|\theta)(\tfrac{\partial}{\partial\theta} \ln f(X|\theta))^T] \\ &= \begin{bmatrix} F_{Rxx} & F_{Rxy} & F_{Rxz} \\ F_{Rxy}^T & F_{Ryy} & F_{Ryz} \\ F_{Rxz}^T & F_{Ryz}^T & F_{Rzz} \end{bmatrix} (3D \quad situation) \end{aligned} \tag{5.11}$$

where $f(X|\theta)$ is the joint PDF of the observation vector X conditioned on θ. Then the

logarithm of the joint condition pdf is:

$$l(X|\theta) = \sum_{i=1}^{M+N} \sum_{j \in H_i j<i} \log f_{X|\theta}(X_{i,j}|p_i, p_j) \tag{5.12}$$

It is shown in [70] The elements of F_θ are:

$$[F_{R_{xx}}]_{k,l} = \begin{cases} \gamma \sum_{i \in H(k)} \frac{(x_k - x_i)^2}{d_{ki}^s} & k = l \\ -\gamma I_{H(k)}(l) \frac{(x_k - x_l)^2}{d_{kl}^s} & k \neq l \end{cases} \tag{5.13}$$

$$[F_{R_{xy}}]_{k,l} = \begin{cases} \gamma \sum_{i \in H(k)} \frac{(x_k - x_i)(y_k - y_i)}{d_{ki}^s} & k = l \\ -\gamma I_{H(k)}(l) \frac{(x_k - x_l)(y_k - y_l)}{d_{kl}^s} & k \neq l \end{cases}$$

$$[F_{R_{xz}}]_{k,l} = \begin{cases} \gamma \sum_{i \in H(k)} \frac{(x_k - x_i)(z_k - z_i)}{d_{ki}^s} & k = l \\ -\gamma I_{H(k)}(l) \frac{(x_k - x_l)(z_k - z_l)}{d_{kl}^s} & k \neq l \end{cases}$$

$$[F_{R_{yy}}]_{k,l} = \begin{cases} \gamma \sum_{i \in H(k)} \frac{(y_k - y_i)^2}{d_{ki}^s} & k = l \\ -\gamma I_{H(k)}(l) \frac{(y_k - y_l)^2}{d_{kl}^s} & k \neq l \end{cases}$$

$$[F_{R_{yz}}]_{k,l} = \begin{cases} \gamma \sum_{i \in H(k)} \frac{(y_k - y_i)(z_k - z_i)}{d_{ki}^s} & k = l \\ -\gamma I_{H(k)}(l) \frac{(y_k - y_l)(z_k - z_l)}{d_{kl}^s} & k \neq l \end{cases}$$

$$[F_{R_{zz}}]_{k,l} = \begin{cases} \gamma \sum_{i \in H(k)} \frac{(z_k - z_i)^2}{d_{ki}^s} & k = l \\ -\gamma I_{H(k)}(l) \frac{(z_k - z_l)^2}{d_{kl}^s} & k \neq l \end{cases}$$

Here, γ is a channel constant and s is an exponent, both of which are functions of the measurement type and are given in tabel 5.1

Table 5.1: differences in parameters for TOA and RSS

	channel constant γ	exponent s
TOA	$\gamma = \frac{1}{(v_p \sigma_T)^2}$	2
RSS	$(\frac{10\alpha}{\sigma_{dB} log 10})^2$	4

Where for TOA based localization technique, v_p is the propagation speed of the signal and σ_T is the standard deviation of the ranging error. for RSS based localization technique, α is the path loss gradient and σ_{dB} is the standard deviation of the shadow fading.

Let $\hat{x}_i, \hat{y}_i, \hat{z}_i$ be the unbiased estimation of x_i, y_i, z_i, the trace of the covariance of the ith location estimate is given by:

$$\begin{aligned}
&\sigma_i^2 = tr\left\{cov_\theta(\hat{x}_i, \hat{y}_i, \hat{z}_i)\right\} \\
&= Var_\theta(\hat{x}_i) + Var_\theta(\hat{y}_i) + Var_\theta(\hat{z}_i) \\
&\geq \left[F_{R_{xx}} - (F_{R_{xy}} F_{R_{xz}}) \begin{pmatrix} F_{R_{yy}} & F_{R_{yz}} \\ F_{R_{yz}} & F_{R_{zz}} \end{pmatrix}^{-1} \begin{pmatrix} F_{R_{xy}} \\ F_{R_{xz}} \end{pmatrix}\right]^{-1}_{i,i} \\
&+ \left[F_{R_{yy}} - (F_{R_{xy}} F_{R_{yz}}) \begin{pmatrix} F_{R_{xx}} & F_{R_{xz}} \\ F_{R_{xz}} & F_{R_{zz}} \end{pmatrix}^{-1} \begin{pmatrix} F_{R_{xy}} \\ F_{R_{yz}} \end{pmatrix}\right]^{-1}_{i,i} \\
&+ \left[F_{R_{zz}} - (F_{R_{xz}} F_{R_{yz}}) \begin{pmatrix} F_{R_{xx}} & F_{R_{xy}} \\ F_{R_{xy}} & F_{R_{yy}} \end{pmatrix}^{-1} \begin{pmatrix} F_{R_{xz}} \\ F_{R_{yz}} \end{pmatrix}\right]^{-1}_{i,i}
\end{aligned} \tag{5.14}$$

5.3 CRLB with randomness in the transmitted power

Until now, we assume the sensors have perfect knowledge of their transmit power,if none of the N sensors have perfect knowledge of their transmit power [31]. The Bayesian CRLB [87] also called as Vantrees inequality states that any estimator $\hat{\theta}$ must have error correlation matrix $R_\in$ satisfying

$$R_\in > F^{-1} = [F_\theta + F_p] \tag{5.15}$$

where $R_{\in} = E[(\hat{\theta} - \theta)(\hat{\theta} - \theta)^T]$, with F_θ and F_p are the fisher information matrix and prior information matrix respectively and are give by equns (5.16)

$$\begin{aligned} F_\theta &= -E[\bigtriangledown_\theta(\bigtriangledown_\theta ln f(p_{i,j}|\theta))^T] \\ F_p &= -E[\bigtriangledown_\theta(\bigtriangledown_\theta ln f(\theta))^T] \end{aligned} \tag{5.16}$$

where $p_{i,j}$ is the bi-directional measurement vector. The prior information matrix F_p is given in eqation (5.17)

$$F_p = diag[0_n^T, 0_n^T, 0_n^T, 1_N^T/\sigma_\pi^2] \tag{5.17}$$

where 0_n is a length-n vector of zeros and 1_N is an N length vector of ones and σ_π^2 is the variance of the random variable π_{0i} (the power at 1 cm distance from transmitter i) which is assumed to have an i.i.d Gaussian prior for every sensor i.

We model the bi-directional measurements $P_{i,j}$ and $P_{j,i}$ using vector $p_{i,j} = [P_{i,j}P_{j,i}]$ as a bi-variate gaussian with mean $u_{i,j}$ and variance $C_{i,j}$, where

$$u_{i,j} = \begin{bmatrix} \pi_{0j} - 10\alpha log_{10}\frac{|ri-rj|^2}{\triangle_0^2} \\ \pi_{0i} - 10\alpha log_{10}\frac{|ri-rj|^2}{\triangle_0^2} \end{bmatrix} \tag{5.18}$$

$$C_{i,j} = \sigma_{dB}^2 \begin{bmatrix} 1 & \rho \\ \rho & 1 \end{bmatrix} \tag{5.19}$$

Where α is the path loss exponent, and ρ is the correlation coefficient between the bidirectional measurements, $0 \leq \rho \leq 1$. For the purpose of discussion we transform the bidirectional measurement vector $p_{i,j}$ by an orthogonal matrix A as:

$$\tilde{p_{i,j}} = Ap_{i,j}, A = \begin{bmatrix} 1 & 1 \\ 1 & -1 \end{bmatrix} \tag{5.20}$$

such a full rank transformation of measurement does not change the Fisher information. For simplicity of notation, we denote $\tilde{p}_{i,j} = [\bar{p}_{i,j} p_{ij}^{\triangle}]^T$, where $\bar{p}_{ij}$ corresponds to the average of the two measurements and $p_{ij}^{\triangle}$ corresponds to the difference between the two measurements. After some mathematical analysis, it is seen that $\bar{p}_{ij}$ has a mean $\bar{u}_{ij}$ and covariance $\bar{C}$ and $p_{ij}^{\triangle}$ has a mean $u_{ij}^{\triangle}$ and covariance $C^{\triangle}$ as given below:

$$\begin{aligned} \bar{u}_{ij} &= \pi_{0j} + \pi_{0i} - 10\alpha log_{10} \tfrac{|ri-rj|^2}{\triangle_0^2}; \bar{C} = \tfrac{(1+\rho)\sigma_{dB}^2}{2} I_{3n+N} \\ u_{ij}^{\triangle} &= \tfrac{\pi_{0j}-\pi_{0i}}{2}; C^{\triangle} = \tfrac{(1-\rho)\sigma_{dB}^2}{2} I_{3n+N} \end{aligned} \tag{5.21}$$

where I_{3n+N} is $3n + N \times 3n + N$ identity matrix and $\bar{u}$ and $u^{\triangle}$ are the mean values of the sum and difference of measurements respectively for all measurement pairs,

$$\bar{u} = [\bar{u}_{i_1,j_1}, ..., \bar{u}_{i_s,j_s}]^T; u^{\triangle} = [u_{i_1,j_1}^{\triangle}, ..., u_{i_s,j_s}^{\triangle}] \tag{5.22}$$

where $i_1, j_1, \cdots, i_s, j_s$ corresponds to each unique pair. A pair makes measurement if they are in the measurement range of each other. Here we assume that the measurement range is infinite (i.e., every sensor can do measurements with every other sensor.) The Fisher information matrix F_θ given in equation 5.16 can be split into two sub matrices $\bar{F}_\theta$ and $F_\theta^{\triangle}$ corresponding to sum and difference measurements due to their independence.

$$F_\theta = \bar{F}_\theta + F_\theta^{\triangle} \tag{5.23}$$

The Fisher information matrix of a vector of multivariate Gaussian measurements with mean $\mu(\theta)$ and covariance C is given by [69] and shown in the appendix. The derivation of the individual elements of the matrix are given in [84].

Chapter 6

Results and Discussions

In this chapter, we present the results of our analysis of the accuracy for localization of the VCE as it travels inside the human GI tract. We compare the performance of RSS and TOA based localization techniques in the major digestive organs in the GI tract as well as the path of movements of the VCE inside the small intestine. We study the effects of the number of receiver sensors on body surface and their topology on the localization accuracy. We also analyze the influence of number of transmitter sensors in cooperation and the randomness in their transmitted power on the localization accuracy. As shown in Fig.3.3, M receiver sensors are distributed evenly on the surface of the body torso and N capsule pills are distributed inside the GI tract environment. Connectivity is assumed between the VCEs and the body mounted sensors and among the VCEs. The path loss parameters are determined by the length of each connection as mentioned in section **??**. As shown in Fig.3.3, M receiver sensors are distributed evenly on the surface of the body torso and N capsule pills are distributed inside the GI tract environment. Connectivity is assumed between the VCEs and the body mounted sensors and among the VCEs. The path loss parameters are determined by the length of each connection as mentioned in section **??**.

For the analysis of the experiments, we compute the average Root Mean Square Error (RMSE) of the location error of each situation. For the case of N different capsule locations, the average RMSE is computed by:

$$RMSE_{avg} = \sqrt{\frac{\sum_{i=1}^{N} \sigma_{x_i}^2 + \sigma_{y_i}^2 + \sigma_{z_i}^2}{N}} \tag{6.1}$$

where $\sigma_{x_i}^2, \sigma_{y_i}^2$ and $\sigma_{z_i}^2$ are the variance of each coordinate value of the ith pill location, given by equation 5.14.

6.1 In-body localization setup

To evaluate the impact of the organ shape and location on localization accuracy. We fixed the number of receiver sensors to 32 and assumed only one single capsule in each organ. We calculated the 3D-CRLB for all the possible location points inside each organ (634 points for stomach, 1926 points for small intestine and 3334 points for large intestine). Figure **??** shows the CDF comparison of location error bound in different organs for RSS and TOA based localization.

6.1.1 Effect of organ shape and location

To evaluate the impact of the organ shape and location on localization accuracy. We fixed the number of receiver sensors to 32 and assumed only one single capsule in each organ. We calculated the 3D-CRLB for all the possible location points inside each organ (634 points for stomach, 1926 points for small intestine and 3334 points for large intestine). Figure **??** shows the CDF comparison of location error bound in different

organs for RSS and TOA based localization.

The localization error for capsule in small intestine and stomach is apparently smaller than that in large intestine for both RSS and TOA based localization techniques.The average value of σ_i for RSS based localization technique is four times larger than that of TOA based techniques which confirms that TOA based ranging is better for high resolution requirement when the multipath problem is not severe. The localization error for capsule in stomach has the lowest average value but distributed in a wider range compared to the errors in other two environments. These observations can be explained by the geometric relationship between the sensor array and the organs. As we can see from fig. 3.2(a), stomach is located in the upper part of the receiver sensor array system, and its volume is the smallest among the three organs. Therefore, the localization error varies more in the stomach environment. The points located in the upper part of stomach have larger localization error value as they are far from the center of the receiver array system, the points in the lower part of stomach have smaller localization error value. The small intestine is located in the center part of human abdomen cavity and the lumen is more centralized compared to large intestine. Therefore, the localization error inside small intestine is smaller than that in large intestine. Considering the physicians are expecting localization accuracy less than several centimeters. The TOA ranging based system provides a more promising results.

6.1.2 Effect of number of receiver sensors

In this subsection, we investigate the impact of number of receiver sensors on localization accuracy. In this experiment, 12000 Monte Carlo simulations (3 different organs,

4 different number of receiver sensors and 1000 simulations per organ) were carried out with the number of receiver sensors varied from 8 64. During each simulation, we assume one capsule is located randomly inside the human digestive system. The results show that the number of receivers has significant influence on the accuracy of localization when the number of receivers is smaller than 32 especially for RSS based localization technique.Finally, notice that for all the three organs, at least 32 receiver sensors are needed to guarantee the performance of 50mm average RMSE.

6.1.3 Effect of sensor configuration

In this experiment, three different placement for receiver sensors are considered, which represents the potential sensor arrangement in practice, as shown in fig.6.3 .

Half of the sensors are on the front plane of the jacket and, the other half are located in the rear plane of the jacket. These sensor configurations can be seen to have three distinct configurations namely, (1): Sensors concentrated at the borders of the jacket, (2): Sensors uniformly distributed in both the planes of the jacket, (3): Sensors concentrated at the center of the jacket. Figure 6.4 shows the RMSE of the three different sensor population for the three distinct configurations. Better performance is achieved when the sensors are concentrated near the center of the jacket for RSS based localization technique, while sensors distributed around the border of the jacket achieves higher accuracy for TOA based localization technique. Arranging all the sensors according to the technique employed is important to achieve the optimal performance for the localization system.

6.1.4 Effects of the shape of the path in the small intestine

Since the small intestine is a curled and folded long tube in the GI tract, it is the most complex part in the digestive system. We specifically analyzed the accuracy limit when the capsule moves along its path in the small intestine because the location of abnormalities found in this organ attracts the physicians mostly. Our analysis is based on the same RSS path loss and, TOA ranging models, but along the small intestine path shown in Fig.**??**. The length of this typical 3D intestine path model is 8 meters and we have used 32 body-mounted sensors for localization. The results of RSS- and TOA-based localization accuracy bounds along the small intestine path are shown in figure .6.5. The mean of localization error bounds for the RSS- and TOA based localizations are 48 and 13mm. In addition,

the accuracy limit of RSS based localization technique fluctuates much more higher than the TOA based localization technique. The accuracy limit of RSS based technique varies more than 10mm along the small intestine path, while the accuracy limit of TOA based technique only exhibits less than 0.5mm of variation along the small intestine path. However, both techniques show similarities in performance influenced by the geometric relationship between the capsule transmitter and the receiver array on the body surface. For example, the localization error bound for both techniques reaches the local maximums at 4 and 6 meter from the beginning of the small intestine.

6.1.5 Effect of number of Pills in cooperation

For this experiment, we fixed the number of receivers on body surface to 32 and increased the number of pills from 1 to 5. The pills are assumed to be randomly dis-

tributed inside the digestive system and they can measure the RSS or TOA from each other. We studied the effect of cooperation among pills using 15000 different situations for cooperative VCE localization.

The results are presented in Fig. 6.6 as the number of pills increase from 1 to 5. Localization error decreased by 5mm for RSS based technique while it remains almost the same for TOA based technique. Compared to the impact of number of receiver sensors, the number of pills in cooperation has less influence on the accuracy of localization. Therefore, our results indicate that increasing the number of receiver sensors on body surface is a more effective way to improve the overall localization performance than increasing the number of pills in cooperation for RSS or TOA based capsule localization.

6.1.6 Effect of random power on the bounds in different organs

In this section, we calculate the bounds for different organs when there's randomness in the transmitted power. We plot the lower bound on the $1-\sigma$ uncertainty ellipse for $\hat{r}_i$, the estimate of the ith capsule sensor coordinate. In this example, we use $\sigma_{dB} = 7.85$ and $\alpha = 4.26$ based on the path loss model discussed in Section . For the simulation, we consider $\rho = 0.704$. The bounds behaves similar at different values of ρ. We also found the bounds as a function of ρ. Finally, in these examples, the prior knowledge of transmit power is $\sigma_\pi = 10dB$. We also consider the case when $\sigma_\pi = 0dB$ for comparison purpose.

For perfectly known transmit power (i.e. $\sigma_\pi = 0dB$), the uncertainty ellipse is shown by solid lines whereas for $\sigma_\pi = 10dB$, it is shown by dotted lines. As we can see in the table below, the increase in the RMSE for all three organs when, randomness in

the transmit power exist.

Table 6.1: Percentage increase in the RMSE(mm) of the capsule in three different organs of the GI track

Human organ	$\sigma_{pi} = 0dB$	$\sigma_{\pi} = 10dB$	$\%$
Stomach	20.8284	21.8090	4.7
Small intestine	22.1399	22.4024	1.2
Large Intestine	26.2381	28.0591	7.1

Figure 4.1 shows corresponding bound in each organ individually. It is observed with given configuration of anchor nodes capsules in large intestine suffered the largest localization error when there was variance in transmit power. For small intestine, the value of RMSE for $\sigma_{\pi} = 0dB$ was $22.1399mm$ and for $\sigma_{\pi} = 10dB$ was $22.4024mm$, i.e. an increase in error of about 1.1.

Next, we calculate the bound over the entire range of correlation coefficient values. Here, we have used a grid of 64 sensors with configuration number 3. The rest of the parameters are kept the same as the previous simulations. In this experiment, the capsule is assumed to be in any one of the three organs and the average performance bounds as a function of ρ is calculated. As seen in figure , as$\rho \rightarrow 1$ the lower bounds are not affected with randomness in transmitted power as much as it is affected at lower value of ρ. Also, at lower values of ρ, the RMSE is lower than that at the higher values.

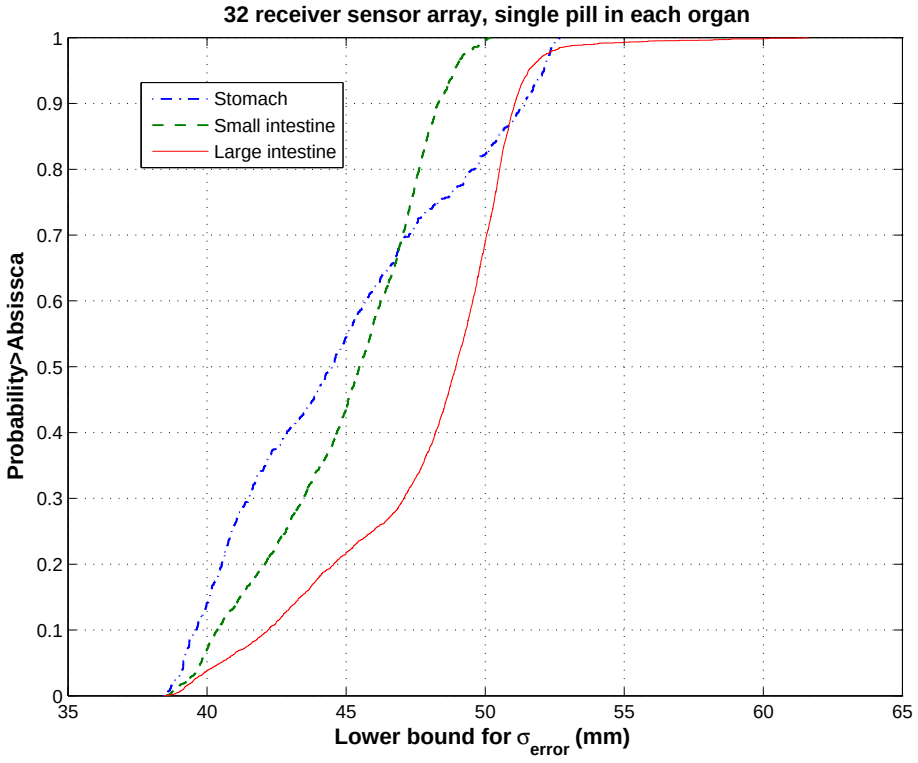

(a)

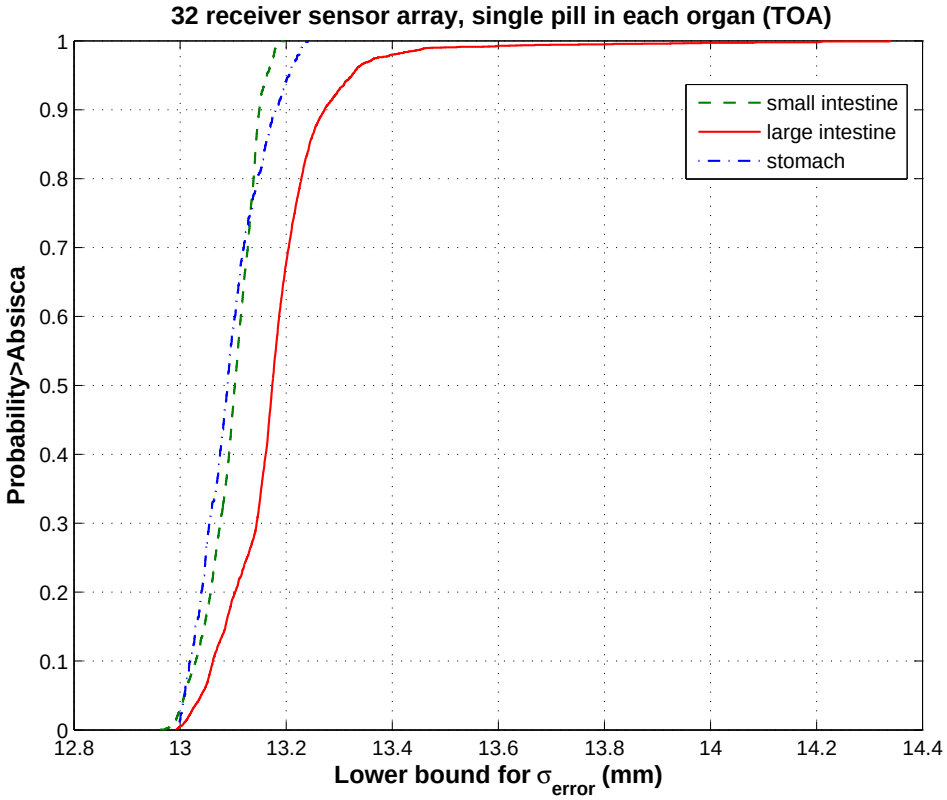

(b)

Figure 6.1: The CDF of location error bounds in stomach, small intestine and large

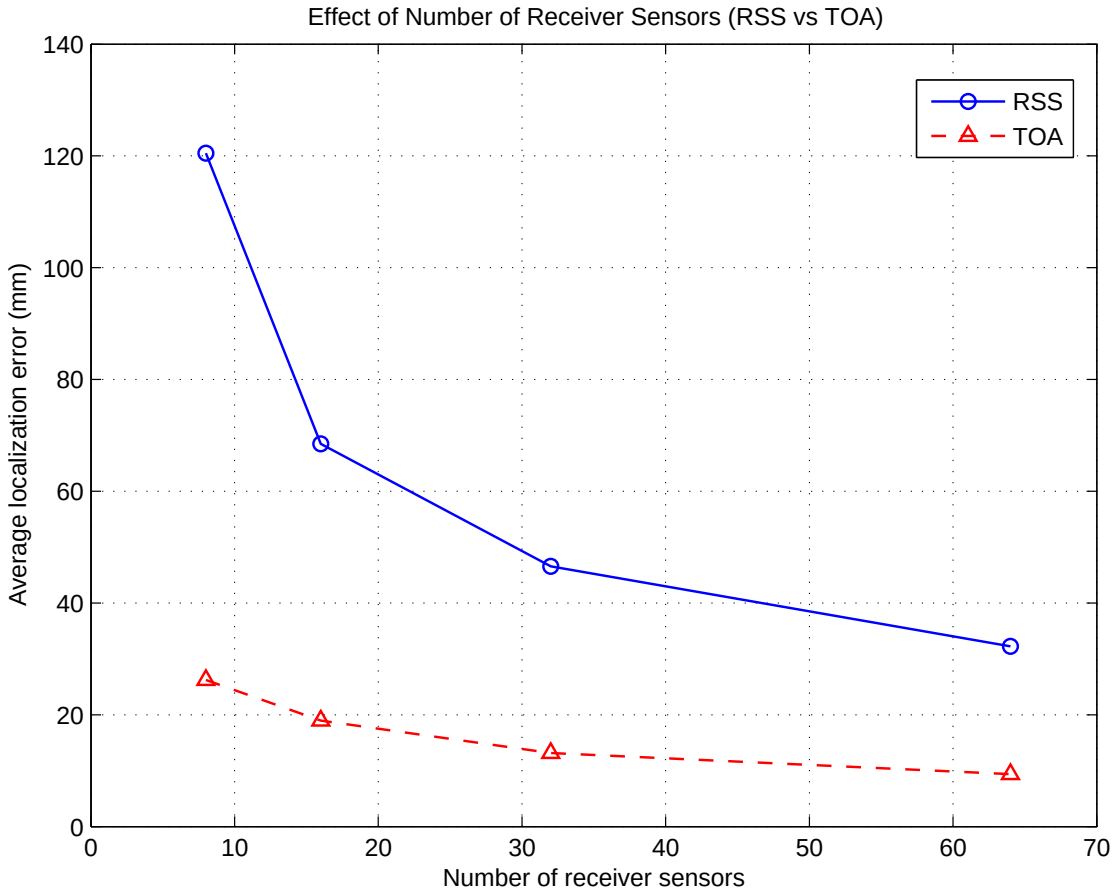

Figure 6.2: Performances of RSS- and TOA-based localization as a function of number of receiver sensors.

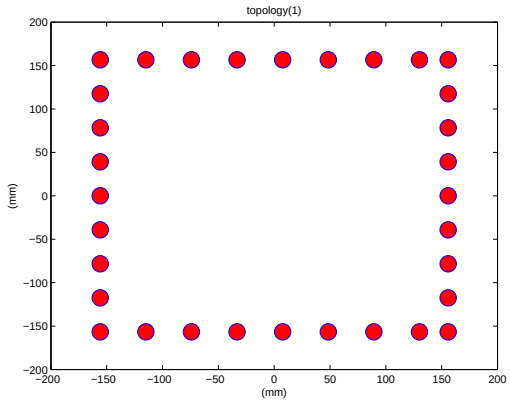

(a)

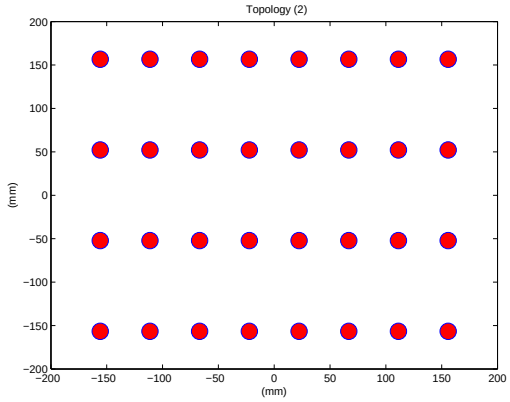

(b)

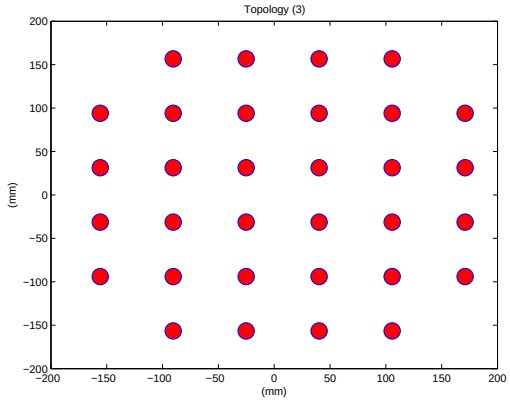

(c)

Figure 6.3: Three patterns for sensor configuration considered for analysis of the bounds (a)Topology1: square configuration (b)Topology2: parallel line configuration (c)Topology3: grid configuration

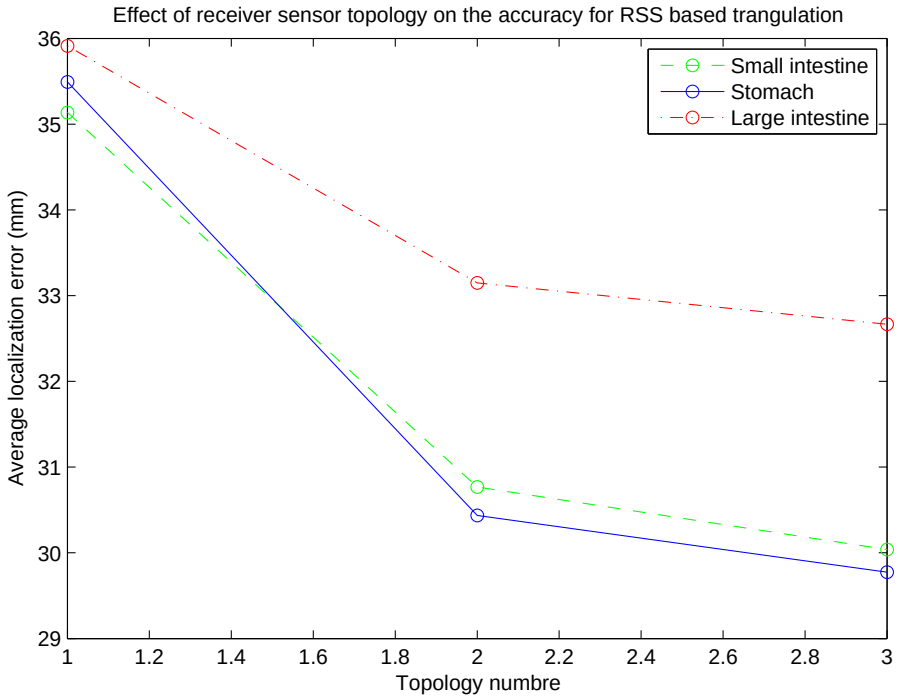

(a)

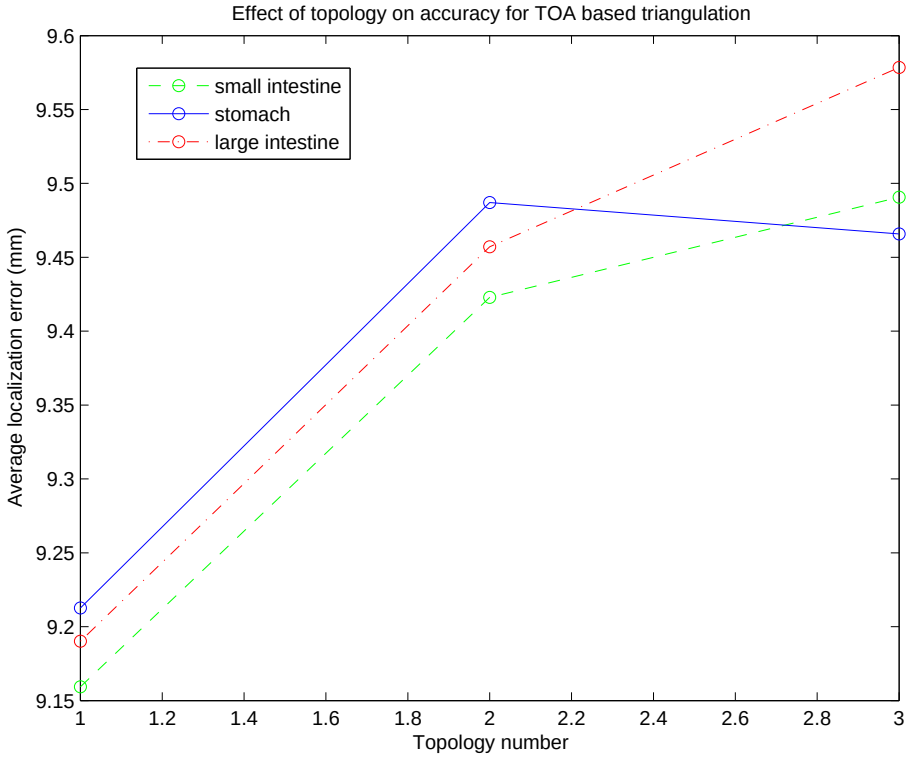

(b)

Figure 6.4: Three sensor configuration considered for analysis of the bounds for 64 sensors (a) TOA (b) RSS

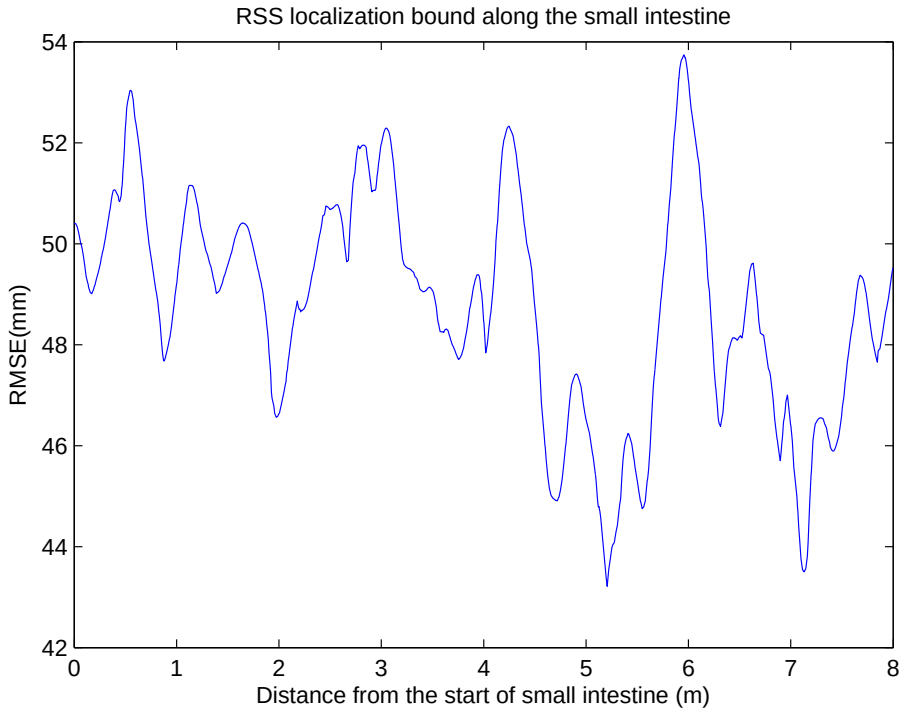

(a)

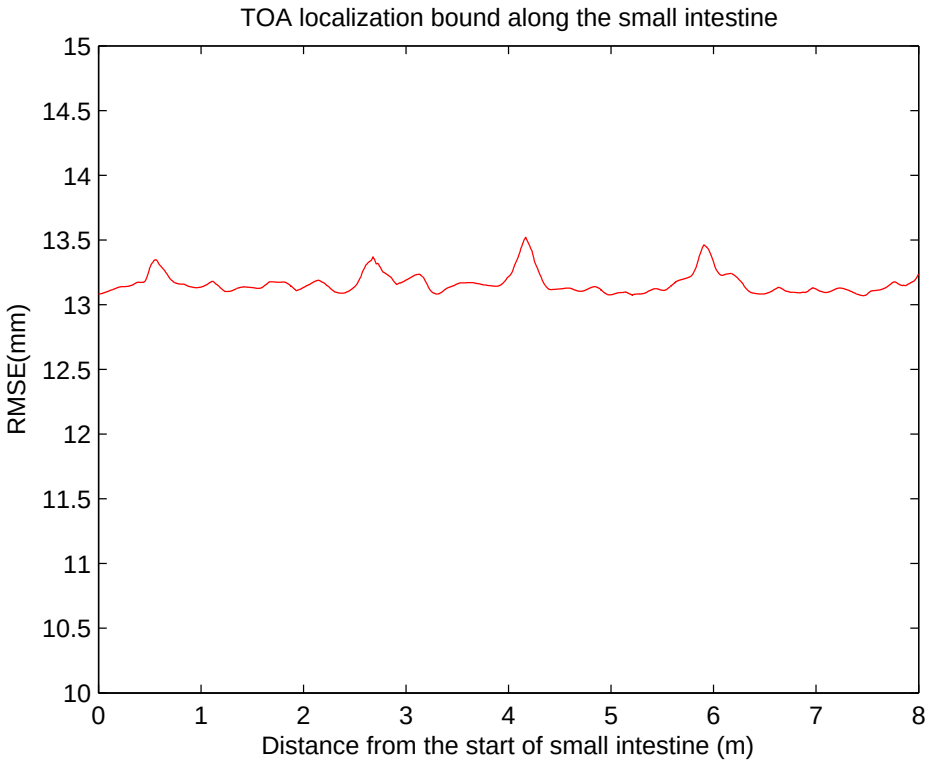

(b)

Figure 6.5: The accuracy limit of localization along the small intestine path (a)RSS-based localization. (b) TOA-based localization

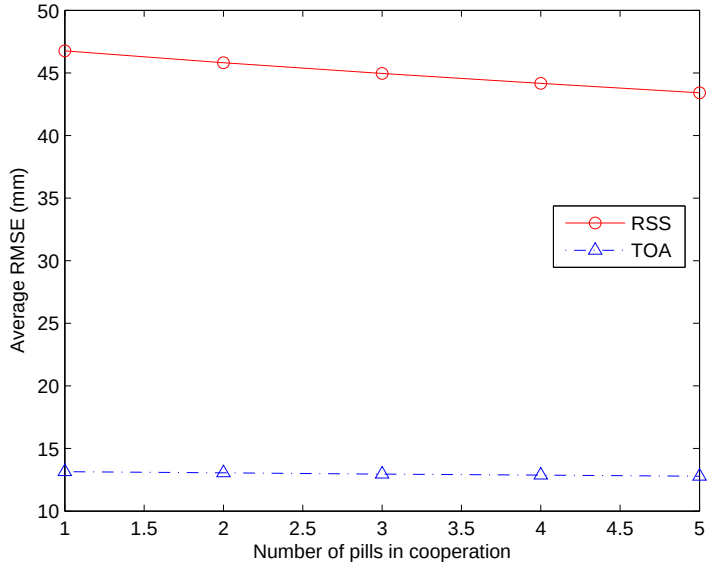

Figure 6.6: Performances as a function of number of pills in cooperation for RSS-and TOA-based localization.

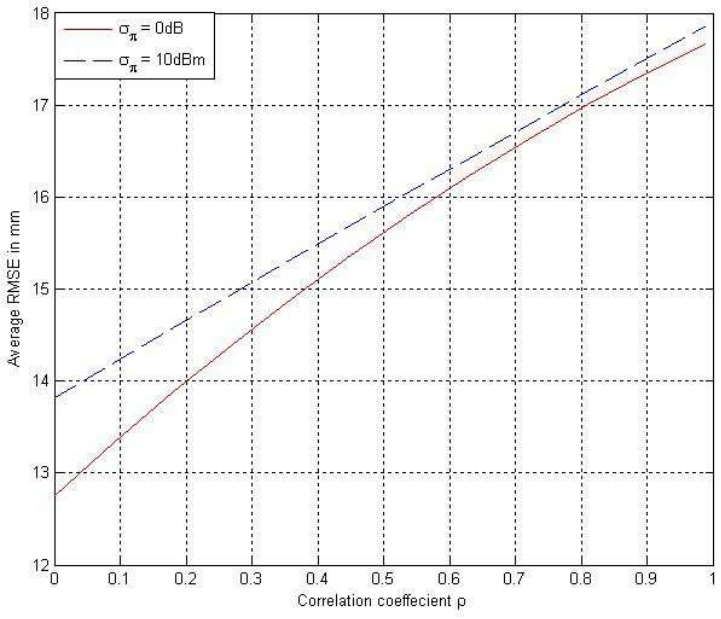

Figure 6.7: The CRLB versus correlation coefficient ρ, for two different σ_π with 64 sensors in parallel configuration. The path loss model parameters are $\sigma_{dB} = 7.85$ and $\alpha = 4.26$

Chapter 7

VCE Movement Model and the Application of Tracking Techniques to VCE Localization

In this chapter, the tracking of VCE is considered. The capsule endoscopes which are currently in use in clinical practices depend on normal peristaltic movement of the gut for their movement. Therefore the movement behavior is totally governed by stress and strain cycle of the intestines which itself is controlled by the nerve system. Clinical observations show that the stress and strain cycle in the guts can be considered constant as far as the patient is under normal condition [78]. In this chapter, we first present the methodology for VCE movement modeling and then propose the implementation of particle filter to fuse the information from the VCE movement model, RF localization signal and information from the inertial system.

7.1 VCE Movement Modeling

A model of the movements of the VCE inside the GI tract is needed for the simulation and the analysis of the temporal and spatial variation of the observed signals by body mounted sensors, design of algorithms for localization, and the emulation of the channel characteristics for performance evaluation and visualization of locations of VCEs in

a CPS platform. GI specialists localize these abnormalities in the GI tract that are reported by the capsule by clinical procedures such as endoscopy, colonoscopy, CT scan or surgery. We can use these abnormalities as landmarks in the GI tract and by counting the number of images observing these landmark estimate the velocity of the VCEs in a particular section of the GI tract.

Unlike the movement of vehicles on roads or human beings in indoor areas, the movement of VCE inside the human body is very inconsistent and varies with the type of organs. While we cannot develop completely generalized models, we should be able to develop empirical movement models for these movements. These models can primarily employ videos augmented by information obtained from CT scans, deep enteroscopy, and surgery where available [26].

The basic idea for developing the movement models is as follows. Some pre-dened landmarks are detected by image processing techniques or identied by a GI specialist through the video source taken by VCE [19], [56].

These landmarks include entrance and exit of each of the four organs traversed by the endoscopy capsule: esophagus, stomach, small intestine and large intestine as well as tumors and bleeding identied in the tract. Figure **??** shows pictures of landmarks inside the GI tract associated with pictures of duodenum, bleeding, tumor and cecum.

Since the videos are taken at a xed frame rate, the average speed of the video capsule can be obtained by dividing the typical distance between known landmarks and the average length of the organs by the elapsed time periods. This speed estimation can be further improved by analyzing the correction between the consecutive frames. Other movement features such as rotations and ips of the capsule can be also estimated based

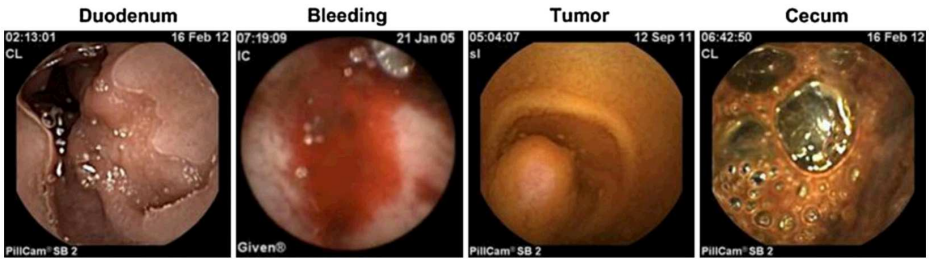

Figure 7.1: Simple pictures of landmarks for localization taken by the capsule

on the captured video source. Another key point is to nd the location of the tumors or bleedings that occurs in different locations of the GI tract. Those abnormalities can be used as new landmarks to reveal the knowledge on speed of the VCEs in different locations of the GI tract and distance of the abnormalities away from xed point. This way, we can emulate the movement of the capsule moving inside the GI tract and associate the video frames to the location inside the tract. A GI specialist can provide data to an engineering team from pre-existing clinical studies. In a typical hospital about 500 video capsule procedures are performed per year, of these, about 15 $\%$ of the patients have CT scans performed of the abdomen and pelvis to provide additional localization data on the position of a pathological lesion. Of these, about 40 $\%$ of patients have exploratory surgery for resecting of a source of bleeding or tumor from the small intestine. At operation the surgeon can accurately measure the position of the lesion with respect to the length of the small intestine. This database can be searched for those patients who have had all of the above procedures. Once the most useful patient population has been identi- ed, interpretation of the VCE studies can be provided by the medical team so that accurate and meaningful data can then be linked to the models and simulations developed by the engineering groups.

7.2 Particle Filter for Multisensor Integration

Since the RF localization techniques suffer from the noisy characteristics of wireless channel and multi-path distortion. It is natural to resort to other techniques such as inertial measurement unit (IMU) to improve the overall performance of the localization system. Traditional inertial measurement units are big and expensive, which limits their integration with the RF localization system. However, the emerging MEMS technology makes low-cost and small size inertial sensors a reality. The IMUs can provide accurate information rates, such as acceleration and angular turn rate, however, after integration to calculate the position and orientation, minor bias and noise in the IMU sensor data can cause unbounded growth of error with time. Fusing information from two technologies with different error behavior always produces better results. The Kalman filter has already been used in combining GPS/IMU or WiFi/IMU [29] to improve the overall performance. In the same manner, we can integrate the information from RF signal localization and the IMU sensors implemented on the VCE to mitigate the noise from each of them. Indeed, when the RF localization failed to provide reliable information due to the human tissue blockage, the IMU system can take over the task until the next reliable RF signal is available. The RF localization can also be used as an absolute sensing mechanism to reset the IMU periodically.

The objective of using the particle filter is to approximate the true posterior position$p(x_k|z_{1:k})$ with a set of discrete weighted particles:

$$p(x_k|z_{1:k}) \approx \omega_k^i \delta(x_k - x_k^i) \tag{7.1}$$

where$x_k = \begin{bmatrix} x(k) \\ y(k) \end{bmatrix}$ is the position state at time k,$x_k^i = \begin{bmatrix} x_k^i \\ y_k^i \end{bmatrix}$ is the state of the ith particle at time k, $z_{1:k}$ is the set of observation results from the RF localization,$\omega_k^i$is the weight of the ith particle.The prediction stage involves using the motion model to obtain a new position for each particle. The noise from the gyro and the odometer are modeled as i.i.d process noise sequences:

$$\begin{bmatrix} x_k^i \\ y_k^i \end{bmatrix} = \begin{bmatrix} x_{k-1}^i \\ y_{k-1}^i \end{bmatrix} + v_{k-1} \begin{bmatrix} cos(\phi(k-1) \\ sin\phi(k-1) \end{bmatrix} + \begin{bmatrix} n_{x_(k-1)} \\ n_{y_(k-1)} \end{bmatrix} \tag{7.2}$$

where v_{k-1} is the velocity from odometer and ϕ_{k-1} is the angular turn estimation obtained by integrating the gyro data around the $z$axis:

$$\phi_{k-1} = \sum_{i=0}^{k-1} \omega_z(i) \tag{7.3}$$

Then, the weight of each particle is updated by the equation [75]:

$$\omega_k^i = \omega_{k-1}^i p(z_k|x_k^i) \tag{7.4}$$

where $p(z_k|x_k^i)$ of observing the RF localization result z_k at the ith particle location. If we denote the position returned by the RF measurement at time k as X_{zk} and the location of ith particle at time k as $X_{x_k^i}$, then the probability is given by [25]

$$p(z_k|x_k^i) = \frac{1}{\sqrt{2\pi}\sigma} exp[-\frac{\|x_{zk} - X_{x_k^i}\|^2}{2\sigma^2}] \tag{7.5}$$

where σ is the measurement confidence. The smaller the σ, the more confident we are in the RF localization results. Here, the value of σ is chosen based on the variation of the RSS readings and the environment of the system. To obtain the posterior density function, we need to normalize the weights each time after they are updated. A common problem with particle filter is the degeneracy phenomenon, which means after a few iterations, most of the particles will have negligible weights [75]. A suitable measure

of degeneracy of the particles is the estimate of the effective sample size N_{eff}, defined as:

$$\hat{N_{eff}} = \frac{1}{\sum_{i=1}^{Ns}(\omega_k^i)^2} \tag{7.6}$$

Where Ns is the number of particles. The resampling is triggered when:

$$\hat{N_e ff} \leq threshold \tag{7.7}$$

The basic idea of resampling is to eliminate particles which have small weights and to concentrate on particles with large weights, the resulting weights are reset to $\omega_k^i = \frac{1}{N_s}$ for all the particles. One problem with resampling is that it reduces the diversity among particles as the resulting samples will contain many repeated points. For resamping algorithms , the most widely used algorithm is the simple sequential importance sampling (SIS) algorithm. The sampling step involves generating a new set $\{x^{i*)_k}\}_{i=1}^{N_s}$ by resampling N_s times from the approximate posterior distribution:

$$p(x_k|z_{1:k}) \approx \sum_{i=1}^{Ns} \omega_k^i \delta(x_k - x_k^i) \tag{7.8}$$

So that $p(x_k^{i*} = x_k^j) = \omega_k^j$.

We have used particle filters to combine RSS-based WiFi localization and movement models from inertial sensors for cooperative robotic applications in indoor areas. The results are promising since this method shows the potential to smooth the localization results while reducing the error by several orders of magnitude. In the localization literature, there is trend to use Kalman lter or particle lters to incorporate imaging landmark information to improve the performance. These classes of algorithms are known as simultaneous localization and mapping (SLAM) algorithms. In the capsule application,

since an endoscopic capsule continually takes pictures inside the GI tract, we can also use the image information to aid the RF localization system.

Chapter 8

Conclusions and Future Directions

This chapter provides an overall conclusion and discussion of some possible directions for the research that has been the focus of this dissertation.

8.1 Conclusions

In this dissertation, we have described thee measurement and modeling campaign that was aimed to characterize the spatial behavior of RSS and TOA based ranging error model for BAN applications. In addition, we provided an analysis of cooperative localization bounds for RSS and TOA based localization techniques for VCE localization. Finally, we proposed the utilization of particle filter to incorporate the information from IMU with the RF localization signal to improve the overall localization performance. We investigated the potential accuracy limits for RSS and TOA based RF localization for the wireless VCE as it travels inside the human GI tract using the CRLB. Results of our analysis showed the possibility of achieving average localization error 5cm in the digestive organs for RSS based localization technique and average localization error of 1.5cm for TOA based localization technique. To achieve these levels of accuracy, we showed that more than 32 sensors mounted on the body surface is needed. Our results demonstrate that increasing the number of sensors mounted on body surface has more

influence on the overall localization performance than increasing the number of pills inside the GI tract. We also analyzed the effect of randomness in transmit power on the localization accuracy in different organs and found that large intestine suffers more inaccuracies due to this effect and that can increase the error by 7.1accuracies of up to 10 cm for the VCE localization, results of this study suggests that designing RF localization techniques for the VCE is practical.

8.2 Future directions

Algorithms Using Movement Models and Landmarks. t should be possible to employ Kalman lter and particle lter to combine the information from the RF localization system using RSS or ToA and capsule movement model information to enhance the accuracy of the localization. Kalman lter [21]and particle lters have been widely used in outdoor and indoor RF localization and navigation applications to incorporate movement models into the TOAbased systems such as GPS and RSS-based localization systems such as WiFi-localization.we have used both lters to combine RSS-based Wi-Fi localization and movement models from inertial sensors for cooperative robotic applications in indoor areas. The results are promising since this method shows the potential to smooth the localization results while reducing the error by several orders of magnitude. In the localization literature, there is trend to use Kalman lter or particle lters to incorporate imaging landmark information to improve the performance. These classes of algorithms are known as simultaneous localization and mapping (SLAM) [85], [24] algorithms. In the capsule application, since an endoscopic capsule continually takes pictures inside the GI tract, we can also use the image information to aid the RF localization system.

Appendices

Appendix A

Derivation of the likelihood function for CRLB calculation

In this appendix, we derive the likelihood function for TOA and RSS in 3D space.

For the TOA case,

$$\begin{aligned} l_{1,i} &= \log f_{t_i|\theta_1,\theta_i}(T_{1,i}|\theta_1,\theta_i) \\ &= -\log\sqrt{2\pi\sigma_T^2} - \frac{T_{1,i}-(\sqrt{(x_1-x_i)^2+(y_1-y_i)^2+(z_1-z_i)^2}/\bar{v})^2}{2\sigma_T^2} \end{aligned} \tag{A.1}$$

$$\begin{aligned} E[\frac{\partial l_{1,i}}{\partial x_1}] &= -\frac{1}{\sigma_T^2}(x_i-x_1)(\frac{\bar{v}T_{1,i}}{\sqrt{(x_1-x_i)^2+(y_1-y_i)^2+(z_1-z_i)^2}}-1) \\ E[\frac{\partial^2 l_{1,i}}{\partial^2 x_1}] &= -\frac{1}{(\bar{v}\sigma_T)^2}\frac{(x_i-x_1)^2}{(x_1-x_i)^2+(y_1-y_i)^2+(z_1-z_i)^2} \end{aligned} \tag{A.2}$$

Similarly, we got

$$\begin{aligned} E[\frac{\partial^2 l_{1,i}}{\partial^2 y_1}] &= -\frac{1}{(\bar{v}\sigma_T)^2}\frac{(y_i-y_1)^2}{(x_1-x_i)^2+(y_1-y_i)^2+(z_1-z_i)^2} \\ E[\frac{\partial^2 l_{1,i}}{\partial^2 z_1}] &= -\frac{1}{(\bar{v}\sigma_T)^2}\frac{(z_i-z_1)^2}{(x_1-x_i)^2+(y_1-y_i)^2+(z_1-z_i)^2} \\ E[\frac{\partial^2 l_{1,i}}{\partial x_1\partial y_1}] &= -\frac{1}{(\bar{v}\sigma_T)^2}\frac{((x_i-x_1)(y_i-y_1)}{x_1-x_i)^2+(y_1-y_i)^2+(z_1-z_i)^2} \\ E[\frac{\partial^2 l_{1,i}}{\partial x_1\partial z_1}] &= -\frac{1}{(\bar{v}\sigma_T)^2}\frac{(x_i-z_1)(z_i-z_1)}{(x_1-x_i)^2+(y_1-y_i)^2+(z_1-z_i)^2} \\ E[\frac{\partial^2 l_{1,i}}{\partial y_1\partial z_1}] &= -\frac{1}{(\bar{v}\sigma_T)^2}\frac{(y_i-y_1)(z_i-z_1)}{(x_1-x_i)^2+(y_1-y_i)^2+(z_1-z_i)^2} \end{aligned} \tag{A.3}$$

and then, we have

$$\begin{aligned}
I_{xx} &= \frac{1}{(\bar{v}\sigma_T)^2}\sum_{i=2}^{m+1}\frac{(x_i-x_1)^2}{(x_1-x_i)^2+(y_1-y_i)^2+(z_1-z_i)^2}\\
I_{yy} &= \frac{1}{(\bar{v}\sigma_T)^2}\sum_{i=2}^{m+1}\frac{(y_i-x_1)^2}{(x_1-x_i)^2+(y_1-y_i)^2+(z_1-z_i)^2}\\
I_{zz} &= \frac{1}{(\bar{v}\sigma_T)^2}\sum_{i=2}^{m+1}\frac{(z_i-z_1)^2}{(x_1-x_i)^2+(y_1-y_i)^2+(z_1-z_i)^2}\\
I_{xy} &= \frac{1}{(\bar{v}\sigma_T)^2}\sum_{i=2}^{m+1}\frac{(x_i-x_1)(y_i-y_1)}{(x_1-x_i)^2+(y_1-y_i)^2+(z_1-z_i)^2}\\
I_{xz} &= \frac{1}{(\bar{v}\sigma_T)^2}\sum_{i=2}^{m+1}\frac{(x_i-x_1)(z_i-y_1)}{(x_1-x_i)^2+(y_1-y_i)^2+(z_1-z_i)^2}\\
I_{yz} &= \frac{1}{(\bar{v}\sigma_T)^2}\sum_{i=2}^{m+1}\frac{(y_i-y_1)(z_i-z_1)}{(x_1-x_i)^2+(y_1-y_i)^2+(z_1-z_i)^2}
\end{aligned} \tag{A.4}$$

For the RSS case, from [69], the density of $P_{1,i}$ is

$$\begin{aligned}
f(P_{1,i}|\theta_i,\theta_1) &= \frac{10/\log 10}{\sqrt{2\pi\sigma_{dB}^2}}\frac{1}{P_{1,i}}\exp[-\frac{\gamma}{8}(\log\frac{d_{1,i}^2}{\tilde{d}_{1,i}^2})^2]\\
\gamma &= (\frac{10\alpha}{\sigma_{dB}\log 10})^2\\
\tilde{d}_{1,i} &= d_0(\frac{P_0}{P_{1,i}})^{1/\alpha}
\end{aligned} \tag{A.5}$$

where $\tilde{d}_{1,i}$ is the maximum likelihood estimation of the range $d_{1,i}$ when the received power $P_{1,i}$ is given

$$l_{1,i} = \log(\frac{10\log 10}{\sqrt{2\pi\sigma_{dB}^2}}\frac{1}{P_r}) - \frac{\gamma}{8}(\log\frac{(x_i-x_1)^2+(y_i-y_1)^2+(z_i-z_1)^2}{\tilde{d}_{1,i}^2})^2 \tag{A.6}$$

then

$$\begin{aligned}
\frac{\partial^2 l_{1,i}}{\partial x_i\partial y_i} &= -\gamma\frac{(x_i-x_1)(y_i-y_1)}{d_{i,1}^4}[-\log(\frac{d_{i,1}^2}{\tilde{d}_{1,i}^2})+1]\\
\frac{\partial^2 l_{1,i}}{\partial x_i\partial y_1} &= -\gamma\frac{(x_i-x_1)(y_i-y_1)}{d_{i,1}^4}[\log(\frac{d_{i,1}^2}{\tilde{d}_{1,i}^2})+1]
\end{aligned} \tag{A.7}$$

Then the FIM simplifies to equation 5.13.

Appendix B

Derivation of CRLB with randomness in transmitted power

Fisher information matrix of a vector of multivariate Gaussian measurements with mean $\mu(\theta)$ and covariance C

$$F_\theta = [\bigtriangledown_\theta \mu(\theta)]^T C^{-1} [\bigtriangledown_\theta \mu(\theta)] = \begin{bmatrix} F_{Rxx} & F_{Rxy} & F_{Rxz} & F_{Rx\pi} \\ F_{Ryx} & F_{Ryy} & F_{Ryx} & F_{Ry\pi} \\ F_{Rzx} & F_{Rzy} & F_{Rzz} & F_{Rz\pi} \\ F_{R\pi x} & F_{R\pi y} & F_{R\pi z} & F_{R\pi\pi} \end{bmatrix} \tag{B.1}$$

From equation 5.23, we have,

$$\bar{F_\theta} = [\bigtriangledown_\theta \bar{\mu}]^T C^{-1} [\bigtriangledown_\theta \bar{\mu}] = \begin{bmatrix} \bar{F_{Rxx}} & \bar{F_{Rxy}} & \bar{F_{Rxz}} & \bar{F_{Rx\pi}} \\ \bar{F_{Ryx}} & \bar{F_{Ryy}} & \bar{F_{Ryx}} & \bar{F_{Ry\pi}} \\ \bar{F_{Rzx}} & \bar{F_{Rzy}} & \bar{F_{Rzz}} & \bar{F_{Rz\pi}} \\ \bar{F_{R\pi x}} & \bar{F_{R\pi y}} & \bar{F_{R\pi z}} & \bar{F_{R\pi\pi}} \end{bmatrix} \tag{B.2}$$

$$\bar{F_\theta^\triangle} = [\bigtriangledown_\theta \mu^\triangle]^T C^{-1} [\bigtriangledown_\theta \mu^\triangle] = \begin{bmatrix} \bar{F_{Rxx}^\triangle} & \bar{F_{Rxy}^\triangle} & \bar{F_{Rxz}^\triangle} & \bar{F_{Rx\pi}^\triangle} \\ \bar{F_{Ryx}^\triangle} & \bar{F_{Ryy}^\triangle} & \bar{F_{Ryx}^\triangle} & \bar{F_{Ry\pi}^\triangle} \\ \bar{F_{Rzx}^\triangle} & \bar{F_{Rzy}^\triangle} & \bar{F_{Rzz}^\triangle} & \bar{F_{Rz\pi}^\triangle} \\ \bar{F_{R\pi x}^\triangle} & \bar{F_{R\pi y}^\triangle} & \bar{F_{R\pi z}^\triangle} & \bar{F_{R\pi\pi}^\triangle} \end{bmatrix} \tag{B.3}$$

BIBLIOGRAPHY

[1]

[2] *Ansoft Full-wave electromagnetic Field Simulation*, `http://www.ansoft.com/products/hf/hfss/`, [Online; accessed 27-September-2010].

[3] Douglas G Adler and Christopher J Gostout, *Wireless capsule endoscopy*, Hospital Physician **39** (2003), no. 5, 14–22.

[4] B. Alavi and K. Pahlavan, *Modeling of the toa-based distance measurement error using uwb indoor radio measurements*, Communications Letters, IEEE **10** (2006), no. 4, 275–277.

[5] Bardia Alavi and Kaveh Pahlavan, *Modeling of the toa-based distance measurement error using uwb indoor radio measurements*, Communications Letters, IEEE **10** (2006), no. 4, 275–277.

[6] A. Alomainy and Yang Hao, *Modeling and characterization of biotelemetric radio channel from ingested implants considering organ contents*, Antennas and Propagation, IEEE Transactions on **57** (2009), no. 4, 999–1005.

[7] N. Alsindi, B. Alavi, and K. Pahlavan, *Empirical pathloss model for indoor geolocation using uwb measurements*, Electronics Letters **43** (2007), no. 7, 370 –372.

[8] N. Alsindi, X. Li, and K. Pahlavan, *Analysis of time of arrival estimation using wideband measurements of indoor radio propagations*, Instrumentation and Measurement, IEEE Transactions on **56** (2007), no. 5, 1537–1545.

[9] N.A. Alsindi, B. Alavi, and K. Pahlavan, *Measurement and modeling of ultrawideband toa-based ranging in indoor multipath environments*, Vehicular Technology, IEEE Transactions on **58** (2009), no. 3, 1046–1058.

[10] Nayef Alsindi and Kaveh Pahlavan, *Cooperative localization bounds for indoor ultra-wideband wireless sensor networks*, EURASIP J. Adv. Signal Process **2008** (2008), 125:1–125:13.

[11] ———, *Cooperative localization bounds for indoor ultra-wideband wireless sensor networks*, EURASIP J. Adv. Signal Process **2008** (2008), 125:1–125:13.

[12] T. Alves, B. Poussot, and J-M Laheurte, *Analytical propagation modeling of ban channels based on the creeping-wave theory*, Antennas and Propagation, IEEE Transactions on **59** (2011), no. 4, 1269–1274.

[13] K. Arshak and F. Adepoju, *Adaptive linearized methods for tracking a moving telemetry capsule*, IEEE international symposium on industrial electronics (ISIE), June 2007, pp. 4–7.

[14] V.N. Bahl, P. Padmanabhan, *Radar: an in-building rf-based user location and tracking system*, INFOCOM 2000. Nineteenth Annual Joint Conference of the IEEE Computer and Communications Societies. Proceedings. IEEE, vol. 2, 2000, pp. 775–784.

[15] Rashmi Bajaj, Samantha Lalinda Ranaweera, and Dharma P Agrawal, *Gps: location-tracking technology*, Computer **35** (2002), no. 4, 92–94.

[16] Nader Bargshady, Kaveh Pahlavan, Yunxing Ye, Ferit Akgul, and Nayef Alsindi, *Bounds on Performance of Hybrid WiFi-UWB Cooperative Localization for Robotic Applications*, Proceedings of IEEE International Symposium on Personal, Indoor and Mobile Radio Communications (PIMRC10), 2010.

[17] Mathieu Bouet and Aldri L dos Santos, *Rfid tags: Positioning principles and localization techniques*, Wireless Days, 2008. WD'08. 1st IFIP, IEEE, 2008, pp. 1–5.

[18] David R Cave, *Wireless video capsule endoscopy*, Presented as 1st Body Aread Network Technology and Applications Workshop at WPI, Worcester, MA, 2011.

[19] David R Cave, David E Fleischer, Christopher J Gostout, Douglas O Faigel, Jonathan A Leighton, Russell I Heigh, Virender K Sharma, Klaus Mergener, Knishka Bhattacharya, Elizabeth Rajan, et al., *A multi-center randomized comparison of the endocapsule: Olympus inc and the pillcam sb: Given imaging in patients with obscure gi bleeding*, Gastrointestinal Endoscopy **65** (2007), no. 5, AB125–AB125.

[20] Min Chen, Sergio Gonzalez, Athanasios Vasilakos, Huasong Cao, and Victor CM Leung, *Body area networks: A survey*, Mobile Networks and Applications **16** (2011), no. 2, 171–193.

[21] S.Y. Chen, *Kalman filter for robot vision: A survey*, Industrial Electronics, IEEE Transactions on **59** (2012), no. 11, 4409–4420.

[22] D. Dardari, A. Conti, U. Ferner, A. Giorgetti, and M.Z. Win, *Ranging with ultra-wide bandwidth signals in multipath environments*, Proceedings of the IEEE **97** (2009), no. 2, 404–426.

[23] B Denis, J Keignart, and N Daniele, *Impact of nlos propagation upon ranging precision in uwb systems*, Ultra Wideband Systems and Technologies, 2003 IEEE Conference on, IEEE, 2003, pp. 379–383.

[24] MWM Gamini Dissanayake, Paul Newman, Steven Clark, Hugh F Durrant-Whyte, and Michael Csorba, *A solution to the simultaneous localization and map building (slam) problem*, Robotics and Automation, IEEE Transactions on **17** (2001), no. 3, 229–241.

[25] Frédéric Evennou and François Marx, *Advanced integration of wifi and inertial navigation systems for indoor mobile positioning*, EURASIP J. Appl. Signal Process. **2006** (2006), 164–164.

[26] D. O. Faigel and D. R. Cave, *Capsule endoscopy*, Saunders Elsevier, Amsterdam, The Netherlands, 2008.

[27] M. Fischer, R. Schreiber, D. Levi, and R. Eliakim, *Capsule Endoscopy: the Localization System*, Gastrointestinal endoscopy clinics of north america **14** (2004), 25–31.

[28] A. Fort, J. Ryckaert, C. Desset, P. De Doncker, P. Wambacq, and L. Van Biesen, *Ultra-wideband channel model for communication around the human body*, Selected Areas in Communications, IEEE Journal on **24** (2006), no. 4, 927–933.

[29] Korbinian Frank, Bernhard Krach, Noel Catterall, and Patrick Robertson, *Development and evaluation of a combined wlan & inertial indoor pedestrian positioning system*, ION GNSS, 2009.

[30] Mordechai Frisch, Arkady Glukhovsky, and Daphna Levy, *Array System and Method for Locating an in Vivo Signal Source*, May 2002.

[31] Ruijun Fu, Yunxing Ye, Ning Yang, and K. Pahlavan, *Doppler spread analysis of human motions for body area network applications*, Personal Indoor and Mobile Radio Communications (PIMRC), 2011 IEEE 22nd International Symposium on, 2011, pp. 2209–2213.

[32] Arianna Menciassia Gastone Ciutia, Pietro Valdastria and Paolo Darioa, *Robotic magnetic steering and locomotion of microsystems for diagnostic and surgical endoluminal procedures*, Robotica, 2009.

[33] S. Gezici, Zhi Tian, G.B. Giannakis, Hisashi Kobayashi, A.F. Molisch, H.V. Poor, and Z. Sahinoglu, *Localization via ultra-wideband radios: a look at positioning aspects for future sensor networks*, Signal Processing Magazine, IEEE **22** (2005), no. 4, 70–84.

[34] Sinan Gezici, *A survey on wireless position estimation*, Wireless Personal Communications **44** (2008), no. 3, 263–282.

[35] Saeed S Ghassemzadeh, Rittwik Jana, Christopher W Rice, William Turin, and Vahid Tarokh, *A statistical path loss model for in-home uwb channels*, Ultra Wideband Systems and Technologies, 2002. Digest of Papers. 2002 IEEE Conference on, IEEE, 2002, pp. 59–64.

[36] Jay L Goldstein, Glenn M Eisen, Blair Lewis, Ian M Gralnek, Steve Zlotnick, John G Fort, et al., *Video capsule endoscopy to prospectively assess small bowel*

injury with celecoxib, naproxen plus omeprazole, and placebo., Clinical gastroenterology and hepatology: the official clinical practice journal of the American Gastroenterological Association **3** (2005), no. 2, 133–141.

[37] Jacob. H, D. Levy, R. Shreiber, A. Glukhovsky, and D. Fisher, *Localization of the Given M2A Ingestible Capsule in the Given Diagnostic Imaging System*, Gastrointestinal Endoscopy, vol. 55, 2002, p. AB135.

[38] M.A. Hanson, H.C. Powell, A.T. Barth, K. Ringgenberg, B.H. Calhoun, J.H. Aylor, and J. Lach, *Body area sensor networks: Challenges and opportunities*, Computer **42** (2009), no. 1, 58–65.

[39] Yang Hao, A. Alomainy, Yan Zhao, C.G. Parini, Y. Nechayev, P. Hall, and C.C. Constantinou, *Statistical and deterministic modelling of radio propagation channels in wban at 2.45ghz*, Antennas and Propagation Society International Symposium 2006, IEEE, 2006, pp. 2169–2172.

[40] J. He, K. Pahlavan, S. Li, and Q. Wang, *A testbed for evaluation of the effects of multipath on performance of toa-based indoor geolocation*, IEEE Trans on instrumentation and Measurements (2013).

[41] M. Heidari, N.A. Alsindi, and K. Pahlavan, *Udp identification and error mitigation in toa-based indoor localization systems using neural network architecture*, Wireless Communications, IEEE Transactions on **8** (2009), no. 7, 3597 –3607.

[42] CHAO HU, MAX Q.-H. MENG, and MRINAL MANDAL, *Efficient magnetic localization and orientation technique for capsule endoscopy*, International Journal of Information Acquisition **02** (2005), no. 01, 23–36.

[43] Chao Hu, MQ-H Meng, Mrinal Mandal, and Xiaona Wang, *3-axis magnetic sensor array system for tracking magnet's position and orientation*, Intelligent Control and Automation, 2006. WCICA 2006. The Sixth World Congress on, vol. 2, IEEE, 2006, pp. 5304–5308.

[44] Anders J Johansson, *Wireless communication with medical implants: antennas and propagation*, Ph.D. thesis, Citeseer, 2004.

[45] Emil Jovanov, Aleksandar Milenkovic, Chris Otto, and Piet C De Groen, *A wireless body area network of intelligent motion sensors for computer assisted physical rehabilitation*, Journal of NeuroEngineering and rehabilitation **2** (2005), no. 1, 6.

[46] Aravind Kailas and Mary Ann Ingram, *Wireless aspects of telehealth*, Wireless personal communications **51** (2009), no. 4, 673–686.

[47] M Kanaan and K Pahlavan, *Algorithm for toa-based indoor geolocation*, Electronics Letters **40** (2004), no. 22, 1421–1422.

[48] M. Kanaan and K. Pahlavan, *Cn-toag: a new algorithm for indoor geolocation*, Personal, Indoor and Mobile Radio Communications, 2004. PIMRC 2004. 15th IEEE International Symposium on, vol. 3, 2004, pp. 1906–1910 Vol.3.

[49] Makoto Kawasaki and Ryuji Kohno, *A TOA Based Positioning Technique of Medical Implanted Devices*, Third international Symposium on Medical information & communication technology, ISMCIT09 (Montreal), 2009.

[50] Michel Kieffer and Eric Walter, *Centralized and distributed source localization by a network of sensors using guaranteed set estimation*, Acoustics, Speech and Signal Processing, 2006. ICASSP 2006 Proceedings. 2006 IEEE International Conference on, vol. 4, IEEE, 2006, pp. IV–IV.

[51] C. Knapp and G. Clifford Carter, *The generalized correlation method for estimation of time delay*, Acoustics, Speech and Signal Processing, IEEE Transactions on **24** (1976), no. 4, 320–327.

[52] A. Kuchar, M. Tangemann, and E. Bonek, *A real-time doa-based smart antenna processor*, Vehicular Technology, IEEE Transactions on **51** (2002), no. 6, 1279–1293.

[53] Joon-Yong Lee and Robert A Scholtz, *Ranging in a dense multipath environment using an uwb radio link*, Selected Areas in Communications, IEEE Journal on **20** (2002), no. 9, 1677–1683.

[54] B Lewis and N Goldfarb, *The advent of capsule endoscopya not-so-futuristic approach to obscure gastrointestinal bleeding*, Alimentary pharmacology & therapeutics **17** (2003), no. 9, 1085–1096.

[55] Blair S Lewis and Paul Swain, *Capsule endoscopy in the evaluation of patients with suspected small intestinal bleeding: results of a pilot study*, Gastrointestinal endoscopy **56** (2002), no. 3, 349–353.

[56] _____, *Capsule endoscopy in the evaluation of patients with suspected small intestinal bleeding: results of a pilot study*, Gastrointestinal endoscopy **56** (2002), no. 3, 349–353.

[57] Gil Y Melmed and Simon K Lo, *Capsule endoscopy: practical applications*, Clinical Gastroenterology and Hepatology **3** (2005), no. 5, 411–422.

[58] M.GHAVAMI, L.B.MICHAEL, and R.KOHNO, *ultra wideband signals and systems in communication engineering.*, John Wiley and Sons, Ltd, NJ, 2004.

[59] Toshihiro Mogi and Tomoaki Ohtsuki, *Toa localization using rss weight with path loss exponents estimation in nlos environments*, Communications, 2008. APCC 2008. 14th Asia-Pacific Conference on, IEEE, 2008, pp. 1–5.

[60] I.K. Mohammed, B.S. Sharif, J.A. Neasham, and D. Giaouris, *Novel mimo 4-dof position control for capsule endoscope*, Circuits and Systems (ISCAS), 2011 IEEE International Symposium on, 2011, pp. 909–912.

[61] E. Monton, J.F. Hernandez, J.M. Blasco, T. Herve, J. Micallef, I. Grech, A. Brincat, and V. Traver, *Body area network for wireless patient monitoring*, Communications, IET **2** (2008), no. 2, 215–222.

[62] Takashi Nakamura, Masahiko Shimizu, Hiroshi Kimura, and Risaburo Sato, *Effective permittivity of amorphous mixed materials*, Electronics and Communications in Japan (Part I: Communications) **88** (2005), no. 10, 1–9.

[63] K. Pahlavan, *Wireless communications for office information networks*, Communications Magazine, IEEE **23** (1985), no. 6, 19–27.

[64] K. Pahlavan, G. Bao, Y. Ye, S. Makarov, U. Khan, P. Swar, D. Cave, A. Karellas, P. Krishnamurthy, and K. Sayrafian, *Rf localization for wireless video capsule endoscopy*, International Journal of Wireless Information Networks **19** (2012), 326–340 (English).

[65] K. Pahlavan and A.H. Levesque, *Wireless information networks*, Wiley and Sons Inc, Second edition, 2005, 738 pages.

[66] K. Pahlavan, X.Li, and J.-P.Makela, *Indoor geolocation science and technology*, IEEE Commun.Mag **Vol. 40** (2002), no. No. 2, 112–118.

[67] Kaveh Pahlavan, *Principles of wireless networks: A unified approach*, John Wiley & Sons, Inc., 2011.

[68] Kaveh Pahlavan and Allen H. Levesque, *Wireless information networks. second edition.*, Artech Houses, Boston, 1996.

[69] N. Patwari and A.O. Hero, *Signal strength localization bounds in ad hoc and sensor networks when transmit powers are random*, Sensor Array and Multichannel Processing, 2006. Fourth IEEE Workshop on, july 2006, pp. 299 –303.

[70] N. Patwari, III Hero, A.O., M. Perkins, N.S. Correal, and R.J. O'Dea, *Relative location estimation in wireless sensor networks*, Signal Processing, IEEE Transactions on **51** (2003), no. 8, 2137 – 2148.

[71] Yihong Qi, H. Suda, and Hisashi Kobayashi, *On time-of-arrival positioning in a multipath environment*, Vehicular Technology Conference, 2004. VTC2004-Fall. 2004 IEEE 60th, vol. 5, 2004, pp. 3540–3544 Vol. 5.

[72] Johannes Reinschke Rainer Kuth and Rudolf Rockelein, *Method for determing the position and orientation of an endoscopy capsule guided through an examination object by using a navigating magnetic field generated by means of a navigation device*, February 2007.

[73] J. Ryckaert, P. De Doncker, R. Meys, A. de Le Hoye, and S. Donnay, *Channel model for wireless communication around human body*, Electronics Letters **40** (2004), no. 9, 543–544.

[74] A.A.M. Saleh and R.A. Valenzuela, *A statistical model for indoor multipath propagation*, Selected Areas in Communications, IEEE Journal on **5** (1987), no. 2, 128–137.

[75] M. Sanjeev Arulampalam, S. Maskell, N. Gordon, and T. Clapp, *A tutorial on particle filters for online nonlinear/non-gaussian bayesian tracking*, Signal Processing, IEEE Transactions on **50** (2002), no. 2, 174–188.

[76] K. Sayrafian-Pour, W.B. Yang, J. Hagedorn, J. Terrill, K. Yekeh Yazdandoost, and K. Hamaguchi, *Channel models for medical implant communication*, International Journal of Wireless Information Networks **17** (2010), no. 3, 105–112.

[77] Andreas G Schreyer, Hans Herfarth, Ron Kikinis, Johannes Seitz, Jürgen Schölmerich, Angela Geissler, and Stefan Feuerbach, *3d modeling and virtual endoscopy of the small bowel based on magnetic resonance imaging in patients with inflammatory bowel disease*, Investigative radiology **37** (2002), no. 9, 528–533.

[78] Dawn M Sears, Andrejs Avots-Avotins, Kim Culp, and Michael W Gavin, *Frequency and clinical outcome of capsule retention during capsule endoscopy for gi bleeding of obscure origin*, Gastrointestinal endoscopy **60** (2004), no. 5, 822–827.

[79] Yi Shang, Wheeler Ruml, and Markus P.J. Fromherz, *Positioning using local maps*, Ad Hoc Networks **4** (2006), no. 2, 240 – 253.

[80] Yuan Shen and M.Z. Win, *Fundamental limits of wideband localization part i: A general framework*, Information Theory, IEEE Transactions on **56** (2010), no. 10, 4956 –4980.

[81] James J Spiker, *The global positioning system: Theory and application*, vol. 1, Aiaa, 1996.

[82] P. Stoica and K.C. Sharman, *Novel eigenanalysis method for direction estimation*, Radar and Signal Processing, IEE Proceedings F **137** (1990), no. 1, 19–26.

[83] R. Stoleru and J.A. Stankovic, *Probability grid: a location estimation scheme for wireless sensor networks*, Sensor and Ad Hoc Communications and Networks, 2004. IEEE SECON 2004. 2004 First Annual IEEE Communications Society Conference on, 2004, pp. 430–438.

[84] P. Swar, Yunxing Ye, K. Ghaboosi, and K. Pahlavan, *On effect of transmit power variance on localization accuracy in wireless capsule endoscopy*, Wireless Communications and Networking Conference (WCNC), 2012 IEEE, april 2012, pp. 2119 –2123.

[85] Ratnasingham Tharmarasa, Thiagalingam Kirubarajan, Marcel L Hernandez, and A Sinha, *Pcrlb-based multisensor array management for multitarget tracking*, Aerospace and Electronic Systems, IEEE Transactions on **43** (2007), no. 2, 539–555.

[86] S. Thomas, *Smartpill Redefines 'Noninvasive'*, Buffalo physician, vol. 40, 2006, pp. 13–14.

[87] H. L. Van Trees, *Detection, estimation, and modulation theory: Part i*, Wiley, New York, 1968.

[88] G.R. Tsouri, A. Sapio, and J. Wilczewski, *An investigation into relaying of creeping waves for reliable low-power body sensor networking*, Biomedical Circuits and Systems, IEEE Transactions on **5** (2011), no. 4, 307–319.

[89] Giovanni Vannucci, *Direct sequence spread spectrum (dsss) communications system with frequency modulation utilized to achieve spectral spreading*, September 22 1992, US Patent 5,150,377.

[90] L. Wang, C. Hu, L. Tian, M. Li, and Max. Q. H, *A Novel Radio Propagation Radiation Model for Localization of the Capsule in GI Tract*, IEEE international conference on robotics and biomimetics, December 19-23, 2009.

[91] Yi Wang, Ruijun Fu, Yunxing Ye, Khan Umair, and Kaveh Pahlavan, *Performance Bounds for RF Positioning of Endoscopy Camera Capsules*, IEEE Radio and Wireless week (Phoenix, Arizona), 2011.

[92] Thad B Welch, Randall L Musselman, Bomono A Emessiene, Phillip D Gift, Daniel K Choudhury, Derek N Cassadine, and Scott M Yano, *The effects of the human body on uwb signal propagation in an indoor environment*, Selected Areas in Communications, IEEE Journal on **20** (2002), no. 9, 1778–1782.

[93] Marilynn P Wylie and Jack Holtzman, *The non-line of sight problem in mobile location estimation*, Universal Personal Communications, 1996. Record., 1996 5th IEEE International Conference on, vol. 2, IEEE, 1996, pp. 827–831.

[94] H. Wymeersch, J. Lien, and M.Z. Win, *Cooperative localization in wireless networks*, Proceedings of the IEEE **97** (2009), no. 2, 427–450.

[95] _____, *Cooperative localization in wireless networks*, Proceedings of the IEEE **97** (2009), no. 2, 427–450.

[96] X.Li, *Super-Resolution TOA estimation with Diversity Techniques for Indoor Geolocation Appllications*, Ph.D. thesis, Worcester Polytechnic Institute, 2003.

[97] Y. Ye, P. Swar, K. Pahlavan, and K. Ghaboosi, *Accuracy of rss-based rf localization in multi-capsule endoscopy*, International Journal of Wireless Information Networks (2012), 1–10.

[98] Kiran Yedavalli, Bhaskar Krishnamachari, Sharmila Ravula, and Bhaskar Srinivasan, *Ecolocation: a sequence based technique for rf localization in wireless sensor networks*, Proceedings of the 4th international symposium on Information processing in sensor networks, IEEE Press, 2005, p. 38.

[99] Marcia Yu, *M2a (tm) capsule endoscopy: A breakthrough diagnostic tool for small intestine imaging*, Gastroenterology Nursing **25** (2002), no. 1, 24–27.

[100] David CK Yuen and Bruce A MacDonald, *Vision-based localization algorithm based on landmark matching, triangulation, reconstruction, and comparison*, Robotics, IEEE Transactions on **21** (2005), no. 2, 217–226.